The Dissertation Committee for Soon Joon Yoon Certifies that this is the approved version of the following dissertation:

Photoacoustic Imaging using Nanoclusters

Committee:

Stanislav Y. Emelianov, Supervisor

Konstantin Sokolov

Keith Johnston

John A. Pearce

Edward Yu

Photoacoustic Imaging using Nanoclusters

by

Soon Joon Yoon, B.S.; M.S.

Dissertation

Presented to the Faculty of the Graduate School of

The University of Texas at Austin

in Partial Fulfillment

of the Requirements

for the Degree of

Doctor of Philosophy

The University of Texas at Austin

August 2014

Dedication

To my family.

Acknowledgements

First and foremost, I would like to express my great appreciation to my supervisor Dr. Stanislav Emelianov for his diligent guidance and enthusiastic support. He always encouraged me and helped me to broaden my perspective on the research. He has shown me how to approach my work as a scientist. Stas has been a strong and supportive adviser to me throughout my Ph.D. studies. I respect him for many reasons, not just his achievement, but also as a personality. He is a passionate and active person who tries many new things. Without his knowledge and guide, it would not have been successful.

I am extremely grateful for Dr. Konstantin Sokolov and Dr. Keith Johnston for tremendous help during my research. I am gratefully indebted to them for brilliant comments and suggestions. Their varied perspectives have helped me to strengthen my work. My appreciation also goes to my committee members, Dr. John Pearce, Dr. Edward Yu for the assistance they provided at all levels of my research.

In addition, I believe that I am lucky enough to meet all the precious colleagues who are helpful and offer invaluable assistance. I would like to acknowledge all my current colleagues Dr. Salavat Aglyamov, Dr. Andrei Karpiouk, Dr. Carolyn L. Bayer, Dr. Seung-Yun Nam, Dr. Jason Cook, Dr. Pratixa Joshi, Dr. Geoff Luke, Dr. Brandon Slaughter, Doug Yeager, Alex Hannah, Laura Ricles, Nich Dana, Robin Hartman, Daniela Santiesteban, Don VanderLaan, Diego Dumani, In-Cheol Sun and Juili Kelvekar. Also, thank to former colleagues, Dr. Srivalleesha Mallidi, Dr. Mohammad Mehrmohammadi, Dr. Seungsoo Kim, Dr. Yun-Sheng Chen, Dr. Suhyun Park, Dr. Jimmy Su, Dr. Bo Wang, Dr. Kimberly Homan, Dr. Iulia Graf, Dr. Sangpil Yoon, Dr. Min Qu, and Dr. Katheryne Wilson. Also, special thanks to Dr. Justina Tam from Dr. Sokolov's lab and Dr. Avinash Murthy and

Bobby Stover from Dr. Johnston's lab. I am also grateful to faculty and staff in the department of Electrical and Computer Engineering and the department of Biomedical engineering.

Lastly, I owe more than thanks to my family for their unconditional love and understanding. My parents always encourage me and support me through the duration of my study. Special thanks to my wife, Youn Hi, for her patience supporting and trusting me all the time. Above all, thank you god for every blessing you have given me.

Photoacoustic Imaging using Nanoclusters

Soon Joon Yoon, Ph.D.

The University of Texas at Austin, 2014

Supervisor: Stanislav Y. Emelianov

Advances in novel imaging techniques and molecular probes are now extending the opportunity of visualizing molecular targets of diseases. Molecular imaging provides anatomic as well as functional and pathological information to sense the expression of molecular biological events. In general, molecular imaging aims to target a specific cell type or tissue and visualize biological events *in vivo* at the molecular or cellular levels through specific probes. Molecular imaging is usually performed in conjunction with probes for specific targets. The objective of this dissertation is to explore molecular imaging by providing highly efficient photoacoustic nanocluster contrast agents to further validate *in vivo* molecular imaging, improve the therapeutic procedure, and study fundamental photoacoustic signal processes from cluster of nanoparticles. Initially, a photothermal stimuli-responsive photoacoustic nanocluster was designed and synthesized to provide highly sensitive dynamic contrast within tissue samples. The photoacoustic signal enhancement from clustering of nanoparticles was demonstrated by characterizing the photoacoustic signal from photothermal stimuli-responsive nanoclusters. After characterization, photothermal stimuli-responsive nanoclusters were injected into a mouse tissue and the dynamic photoacoustic response from the nanoclusters activated by an external laser source was observed. This activation can be repeatedly turned on by modulating input laser signals, suggesting a new route for dynamic photoacoustic contrast

imaging that will further improve the imaging contrast and more accurately guide the drug release process. Despite tremendous advantages of using these nanoparticles, their safety in a biological environment could be a major hurdle for their *in vivo* utilization. In order to avoid accumulation and long-term toxicity of nanoparticles, biodegradable nanoclusters consisting of sub-5 nm primary gold particles stabilized by a weakly adsorbed biodegradable polymer were introduced. The photoacoustic signal from biodegradable nanoclusters was quantitatively characterized. In addition, a photothermal stability of different sizes of biodegradable nanoclusters was investigated. These nanoclusters were then intravenously injected into mice and biodistribution of nanoparticles was observed. Finally, *in vivo* spectroscopic photoacoustic imaging was performed on tumor-bearing mice with antibody conjugated biodegradable nanoclusters. This research may provide a new opportunity for molecular imaging to help diagnose tumors at an early stage and promote clinical translation of these techniques.

Table of Contents

List of Tables

List of Figures

Chapter 1: Introduction

Cancer is one of the most challenging diseases in the world. It is the leading cause of death in developed countries and the second leading cause of death in the United States in 2011 [1][1]. For many years, researchers have developed various diagnostic tools for the detection, differentiation, and staging of cancer at its curable stages, thus increasing the survival rates and reducing healthcare costs [2-4]. Moreover, medical imaging has been explored for developing non- or less-invasive, and highly targeted therapeutic tools with less adverse side effects through accurately monitoring and assessing the outcome of treatments. During recent decades, there has been a tremendous interest in exploiting the development of new medical imaging techniques capable of characterizing anatomical, structural, functional and metabolic characteristics of cancerous tissues [2, 3]. Recent advances in molecular and cellular biology indicated that understanding the cellular and molecular pathways of cancer can lead to diagnosis of the pathology at its early stages of development and affect the cancer treatment significantly [5]. In particular, the development of imaging contrast agents with specific targeting moieties expands the scope of several existing medical imaging modalities from their conventional anatomical and structural imaging to molecular and cellular imaging [5-8]. An optimal imaging modality to identify cancer at its early stages of development must have notable features such as being non-invasive (or minimally invasive), capable of high temporal and spatial resolution and able to provide information about cellular and molecular events with high sensitivity

[1] Some parts of this introduction were published in the journal: M. Mehrmohammadi, S.J. Yoon, D. Yeager, and S.Y. Emelianov, "Photoacoustic imaging for cancer detection and staging," Current Molecular Imaging, 2(1):89 - 105 (2013).

and specificity. Moreover, the ideal imaging modality must have minimal complexity and the potential of being widely available in clinical practice.

Molecular photoacoustic (PA) imaging has shown great potential in combination with molecularly targeted nanoparticles with their highly absorptive properties at desired visible and near-infrared optical wavelength [9-17]. PA imaging is an emerging imaging modality, which is stable, cost effective and non-ionizing, providing functional and pathological information at high resolution in real time [18-21]. There are numerous studies currently exploring photoacoustic imaging using nanoparticles, since molecular PA imaging with nanoparticles is a relatively new imaging modality.

The overall goal of this research is to demonstrate a novel imaging method using nanoclusters as PA contrast agents to validate *in vivo* molecular PA imaging to diagnose cancerous tissue. This dissertation includes the design and characterization of nanoclusters as photoacoustic contrast agents. In order to accomplish the goal of the project, photothermal stimuli-responsive nanoclusters are first developed and characterized to validate a PA signal enhancement. In addition, biodegradable nanoclusters are shown as a PA contrast agent which can be translated to the clinic.

1.1 Significance of Molecular Imaging

Over the past decades, physicians only could detect tumors or monitor their growth by surgery and biopsy. Despite the advent of modern medical imaging, they are still limited to detect tumors at their early stages. However, these recent advances in noninvasive medical imaging modalities allow us to open new opportunities for molecular diagnostic and therapeutic procedures. Molecular imaging provides anatomic as well as functional and pathological information in conjunction with probes to sense the expression of molecular biological events. In general, molecular imaging aims to target a specific cell

type or tissue and visualize biological events *in vivo* at the molecular or cellular levels through specific probes.

Molecular imaging can be used to detect, characterize, and monitor early stage of tumor because the imaging of specific molecular targets which are associated with tumors can allow physicians to diagnose and manage oncology patients earlier. In addition, molecular imaging can investigate the efficacy of drugs. Currently, major imaging modalities capable of providing cellular and molecular information of cancer are optical imaging [22], magnetic resonance imaging (MRI) [23], and radionuclide imaging such as positron emission tomography (PET) [24] and single photon emission computed tomography (SPECT) [25]. These modalities have shown great capabilities and have been extensively studied in cancer diagnosis. However, they suffer from certain limitations such as system complexity and temporal resolution in MRI, limited imaging depth in optical imaging and limited spatial and temporal resolution in PET and SPECT. Therefore, there is still demand for the development of new robust imaging modalities, capable of addressing these limitations and reducing system complexity and implementation cost.

PA imaging has shown tremendous potential in cellular and molecular-specific imaging of cancer. The key advantages which make PA a suitable diagnostic modality for clinical applications are its ability to provide molecular information at clinically relevant depths with a high resolution and in real-time [9-17]. Moreover, it can be easily combined with US imaging as both imaging modalities have shared hardware components and common signal detection regimen. Therefore, through the combination of US and PA imaging, it is possible to obtain information on anatomical, functional, and molecular content of diseased tissues [18-21].

1.2 PHOTOACOUSTIC IMAGING

1.2.1 Principle of Photoacoustic Imaging

PA imaging is based on the principles of photoacoustic effect that were first explored by Alexander Graham Bell in 1880 [26]. Photoacoustic techniques were initially studied in non-biological fields such as physics and chemistry [27, 28]. Since Theodore Bowen introduced PA imaging technique as a biomedical imaging modality in 1981 [29], this technology has been developing quite rapidly by several early adopters of photoacoustic imaging [30-32].

Fundamentally, the photoacoustic technique measures the conversion of electromagnetic energy into acoustic pressure waves [29]. In biomedical PA imaging, the tissue is irradiated with a nanosecond pulsed laser, resulting in the generation of an ultrasound wave due to optical absorption and rapid thermal (or thermoelastic) expansion of tissue (Figure 1.1) [33]. The initial pressure, p_0, generated by an optical absorber, is described as

$$p_0 = \Gamma \mu_a F$$

where F is the laser fluence at the absorber, μ_a is the optical absorption coefficient, and Γ is the Grüneisen parameter of the tissue [34]. By detecting the pressure waves using an ultrasound transducer, an image can be formed with the primary contrast related to the optical absorption of tissue. This unique mechanism through which a PA image is generated provides distinct advantages compared to other *in vivo* imaging modalities. First, the contrast mechanism in PA imaging is based on the differences in optical absorption properties of the tissue components. PA imaging is suited for imaging structures with high optical coefficient such as blood vessels [35-37]. Second, PA imaging can be achieved using longer wavelengths in near-infrared (NIR) region, where tissue absorption is at a minimum. Light can penetrate up to several centimeters into biological tissues at

wavelengths in the near-infrared range while remaining under the safe laser exposure limits for human skin [38, 39].

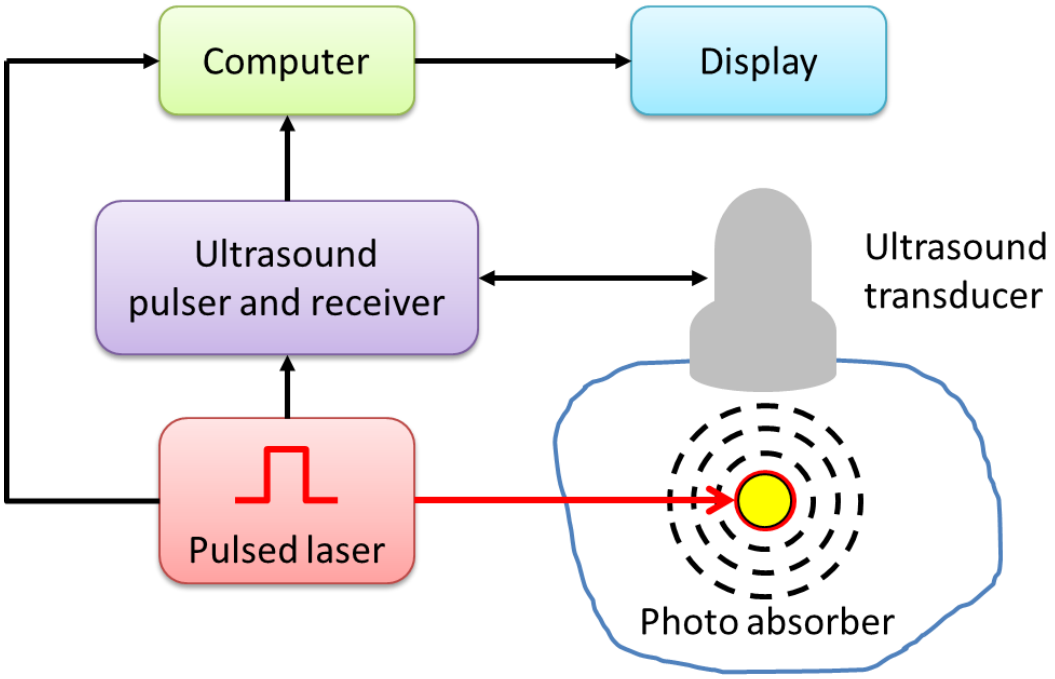

Figure 1.1: A diagram shows the main components of a PA imaging system and the mechanism of PA signal generation

The photoacoustic technique enables imaging deeper into tissues than optical imaging methods that utilize ballistic or quasiballistic photons (e.g., optical coherence tomography or OCT) because photoacoustics does not rely on detection of photons – instead, weakly scattering acoustic waves are detected in response to laser irradiation. Third, a PA imaging system can be easily combined with an US system because both systems can share the same detector and electronics. The primary contrast in US imaging is derived from the mechanical properties of the tissue, which mostly describes anatomical information. Therefore, combined PA and US system can provide both anatomical and functional information [40].

In PA, imaging depth is limited by light penetration and acoustic attenuation. In practice, the incident laser light and acoustic wave generated by the light beam will be attenuated in the tissue. However, the penetration depth is primarily limited by the optical scattering – a dominant component of the optical attenuation in the tissue. Specifically, the optical penetration depth is determined by the effective extinction coefficient $\mu_{eff} = (3\mu_a(\mu_a + \mu'_s))^{1/2}$ obtained from diffusion theory, where μ_a and μ'_s are the absorption coefficient and reduced scattering coefficient of the tissue, respectively [41, 42]. At depths greater than 1 mm, the light diffuses and decays exponentially with the exponential constant equal to μ_{eff}. The penetration depth is defined as the distance at which the intensity of the light inside the tissues falls to 1/e (~ 37%) of its intensity at the surface. The penetration depth, $1/\mu_{eff}$, is strongly wavelength-dependent and it may reach up to several centimeters in NIR region [38, 39].

Spatial resolution of PA imaging at depth beyond quasiballistic penetration of photons is determined by characteristics of an ultrasound transducer. The lateral resolution is dependent on numerical aperture (NA) and the center frequency of the transducer. The axial resolution is inversely proportional to the frequency bandwidth of the transducer [21, 43]. Therefore, a transducer with large NA, higher center frequency and higher bandwidth provides the best spatial resolution. In practice, sub-millimeter spatial resolution is achievable at depth up to several centimeters, and sub-100 μm is possible for penetration depth of several millimeters. Higher lateral resolution (~ 5 μm) in PA imaging can be achieved by using fine optical focusing within less than 1 mm imaging depth where the focused light is in the ballistic regime. In this case, the lateral resolution is determined by optical diffraction limit, however, the axial resolution is still limited by frequency bandwidth and acoustic attenuation [44]. Overall, spatial resolution of photoacoustic imaging decreases as imaging depth increases.

1.2.2 Photoacoustic Contrast Agents

Endogenous Contrast Agents in Photoacoustic Imaging

Biological tissues contain several kinds of endogenous chromophores that can generate PA signal. The main sources of endogenous contrast in PA imaging are hemoglobin, melanin, and lipids. Depending on the wavelength, these endogenous contrast agents may have strong absorption coefficients in comparison with other tissue constituents. Photoacoustic imaging has been used in various applications where endogenous chromophores are present, such as in the visualization of blood vasculature structure and melanoma [36, 37, 45-48]. The absorption coefficients of these chromophores are strongly wavelength dependent. Therefore, if PA imaging is performed at several wavelengths, referred to as spectroscopic PA imaging, it is possible to measure distributions of the chromophores [46, 48, 49]. The use of endogenous chromophores in biomedical imaging has two key advantages. First, the endogenous contrast agents are inherently biologically safe. Although exogenous contrast agents may provide strong contrast and ability to be targeted to specific molecules, one of the major obstacles, inhibiting the clinical use of exogenous contrast agents is safety, such as toxicity and retention in the body. Second, physiological and metabolic changes that differentiate pathological tissue from normal tissue can be monitored because endogenous contrast agents provide the physiological changes, such as oxygen saturation and vascular blood volume in the body [32, 50].

Exogenous contrast agents have been introduced to expand the application of PA imaging in several ways [11, 12, 51, 52]. First, since the PA signal depends on the optical absorption of the photoabsorber, utilizing exogenous contrast agents with large optical absorption at a desired wavelength can increase the PA signal [13, 53, 54]. This effect can subsequently allow imaging at greater depths or using lower optical fluence. Moreover, by

tuning the optical absorption of these exogenous contrast agents to fall in the "tissue optical window" where tissue components have minimal absorption, it is possible to increase the imaging contrast and depth [55-58]. Second, by utilizing small enough contrast agents (such as nanoparticles) that can extravasate from the vasculature, get close to and ultimately tag specific cells or molecules, PA imaging can be utilized to visualize events at the cellular and molecular levels [59-67].

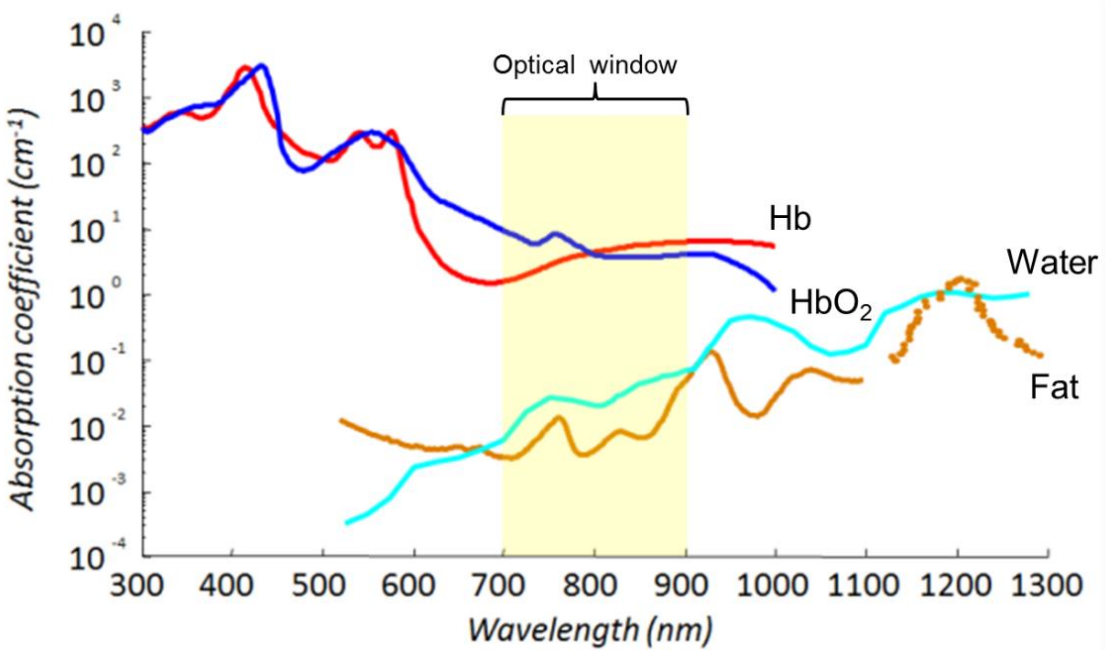

Figure 1.2: Optical absorption of endogenous photo absorbers in tissue. The optical window is shown with a yellow box.

Moreover, having prior knowledge of the optical absorption of such contrast, opens a path to spectroscopic PA imaging, where the PA signals at several different wavelengths are utilized to suppress the signal from background tissue and thus reveal the presence of the contrast agents with a higher contrast [50, 60, 68-72]. Depending on the required

imaging depth, desired light source to be used, and delivery mechanism of nanostructures, the choice of exogenous contrast agents may change.

Exogenous Contrast Agents for Photoacoustic Imaging

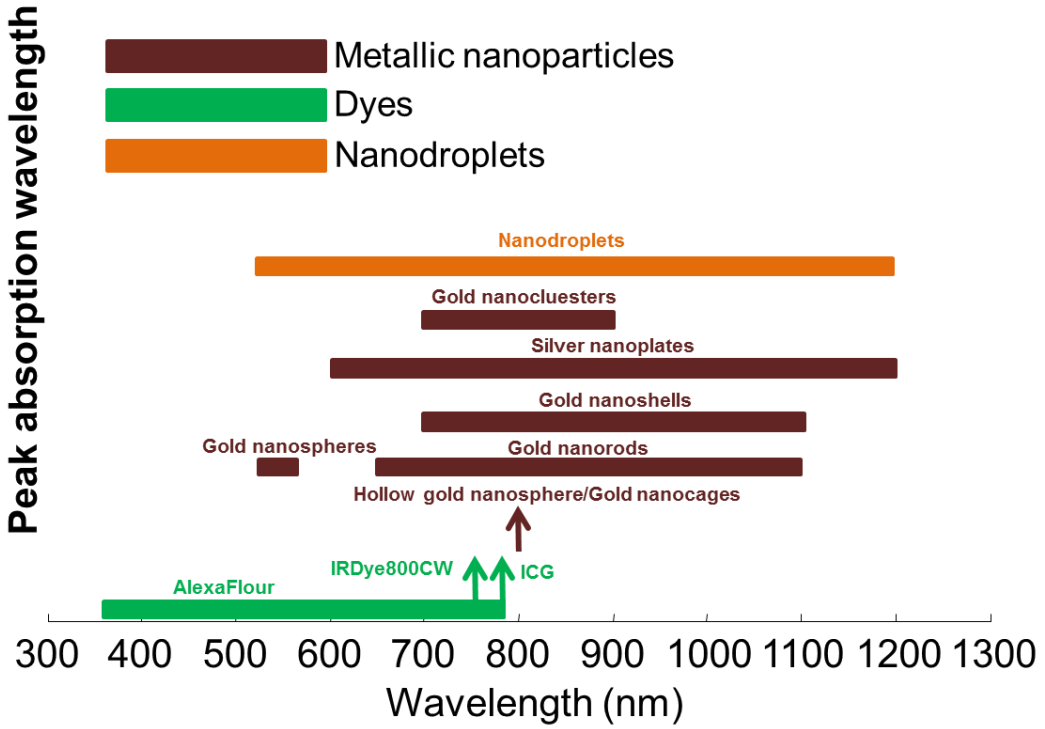

Figure 1.3: The range where peak absorption of major PA imaging exogenous contrast agents falls in. The peak absorptions depend on several parameters such as size, geometry, optical cross-section, etc. SWNTs are shown to have a high optical absorption over a wide range of spectrum including optical window spectrum [98].

Currently, the major contrast agents for PA imaging are metallic nanostructures [17, 52, 53, 57, 60, 73-85], dyes (or fluorophores) [86-90], and single-walled carbon nanotubes (SWNTs) [15, 64, 80, 91-94]. Recently, new PA contrast agents such as perfluorocarbon droplets loaded with metallic nanostructures [95-97] were introduced to

further enhance PA imaging abilities. Figure 1.2 summarizes the optical absorption of tissue components and the peak of optical absorption for several types of exogenous contrast agents used in PA imaging (Figure 1.3).

Contrast-enhanced PA molecular imaging (i.e., PA imaging using molecular targeted exogenous contrast agents) can provide anatomical, functional and molecular information of diseased tissues at clinically relevant depths, with high spatial resolution and obvious contrast. Several research groups has shown the abilities of PA imaging augmented with molecular-targeted contrast agents to detect cancer at the cellular level [57, 60, 63, 65, 99]. Contrast enhanced PA imaging has shown great promise in its ability to detect primary tumors [64, 85], tumor vasculature [100], circulating tumor cells (CTCs) [16, 63, 101, 102], and micro-metastasis in sentinel lymph nodes (SNL) [88, 103]. Table 1 summarizes some reported research studies related to exogenous contrast agent-assisted PA in detection of tumors, CTCs, mapping lymph nodes, and identifying lymphatic metastasis.

Goal of the study	Molecular probe	Imaging Wavelength (nm)	Target
Tumor detection			
PA imaging of orthotopic glioblastoma mice brain tumor	Hybrid multimodal nanostructure	532 nm	None
Spectroscopic PA molecular and Hypoxia imaging of brain tumors	IRDye800	764, 784, 804, 824	$\alpha_v\beta_3$ integrin
PA imaging of breast tumor xenograft in nude mice	IRDye800CW	710 to 890 nm	neutropilin-1 receptor (NPR-1)
PA imaging of targeted SWNTs to detect human glioblastoma tumors in mice	SWNT	750 nm	$\alpha_v\beta_3$ integrin
Spectroscopic PA imaging to monitor the accumulation of silica coated gold nanorods in human endolethial tumor	Gold nanorods	740, 760, 780, 800, 820, 840 nm	None
Spectroscopic PA imaging to detect pancreatic tumor in a nude mouse	Silver Nanoplates	740 to 940 nm	EGFR
PA imaging of targeted SWNTs to detect glioblastoma-astrocytoma tumor xenograft	SWNTs	690 nm	$\alpha_v\beta_3$ integrin
PA Imaging of B16 melanoma in mice	Gold Nanocages	778 nm	α-melanocyte-stimulating hormone
PA imaging of LNCaP prostate cancer cells labeled with gold nanorods and implanted in a nude mice	Gold nanorods	725 nm	Human epidermal growth factor (HER2)/neu antigen
PA imaging of gold nanoshell accumulated in a colon carcinoma tumor	Gold nanoshells	800 nm	None
PA detection of human breast cancer (BT474) tumor xenograft in mice	Gold nanospheres	532 nm	None
CTC detection			
Imaging CTCs labeled both magnetically and optically and are captured using a static magnetic in a mouse with breast cancer xenograft tumor	Magnetic nanoparticles (MNPs) and Gold-coated SWNTs	905 nm	plasminogen activator receptors for MNPS None for Gold-coated SWNTs
Monitoring metastatic cells in blood stream in an ear vein in mice using two-wavelength photoacoustic imaging	Melanin nanoparticles	639 and 865 nm	None
Lymph node metastasis detection			
Mapping SLN using spectroscopic PA imaging of gold nanorods	Gold nanorods	757, 807, 820 nm	None
PA imaging augmented with functionalized gold-coated SWNTs to trace and map lymphatic endothelial cells (LECs) in mouse model.	Gold-coated SWNTs	850 nm	lymphatic endothelial hyaluronan receptor-1 (LYVE-1)
PA Imaging SLN in a rat using ICG	ICG	668 nm	None
PA imaging of cancer cells metastasis from primary tumor in mouse ear to SLN using golden SWNTs	Magnetic nanopartricles (MNPs) and Gold-coated SWNTs	639 and 850 nm	folate
SLN mapping in a rat model using gold nanocages	Gold Nanocages	755 nm	None

Table 1: Summary of nano-sized contrast agents assisted PA in detecting tumors, CTCs, mapping lymph nodes and identifying lymphatic metastasis [98].

1.2.3 Photoacoustic Signal Enhancement from Nanoclusters

Recently, photoacoustic signal enhancement effect has been reported for different forms of aggregates or clusters. The enhancement of photoacoustic signal was observed from different forms of nanoparticle clusters including nanoparticle aggregation by cell endocytosis. Figure 1.4 represents an increase in photoacoustic signal from aggregated silica-coated gold nanoparticles in comparison to disperse nanorods. In these experiments, the photoacoustic signal of the aggregated nanoparticles produced 7 times higher photoacoustic signal compared to that of disperse nanoparticles. In general, the nanoparticles irradiated by pulsed laser generate heat which will be rapidly in the equilibrium state. The generated heat is transferred from the nanoparticles to the surrounding environment, and then, the environment undergoes thermal expansion which produces the pressure wave. The optical absorption properties of nanoparticles are the important factor which leads to the thermal expansion. However, the source of the photoacoustic signal enhancement from aggregated particles is not clear so far. It is likely that the signal enhancement occurs because of thermal interactions in a cluster of nanoparticles. When nanoparticles are aggregated, their thermal fields can overlap because of their small interparticle distance. The thermal coupling of nanoparticles may amplify the photoacoustic signal.

The photoacoustic signal enhancement from clustering of nanoparticles can be further investigated using thermo-sensitive nanoclusters consisting of primary nanoparticles because the interparticle distance of the nanoclusters can be controllable by changing temperature. In addition, the photoacoustic signal enhancement effect can be utilized by any forms of cluster particles.

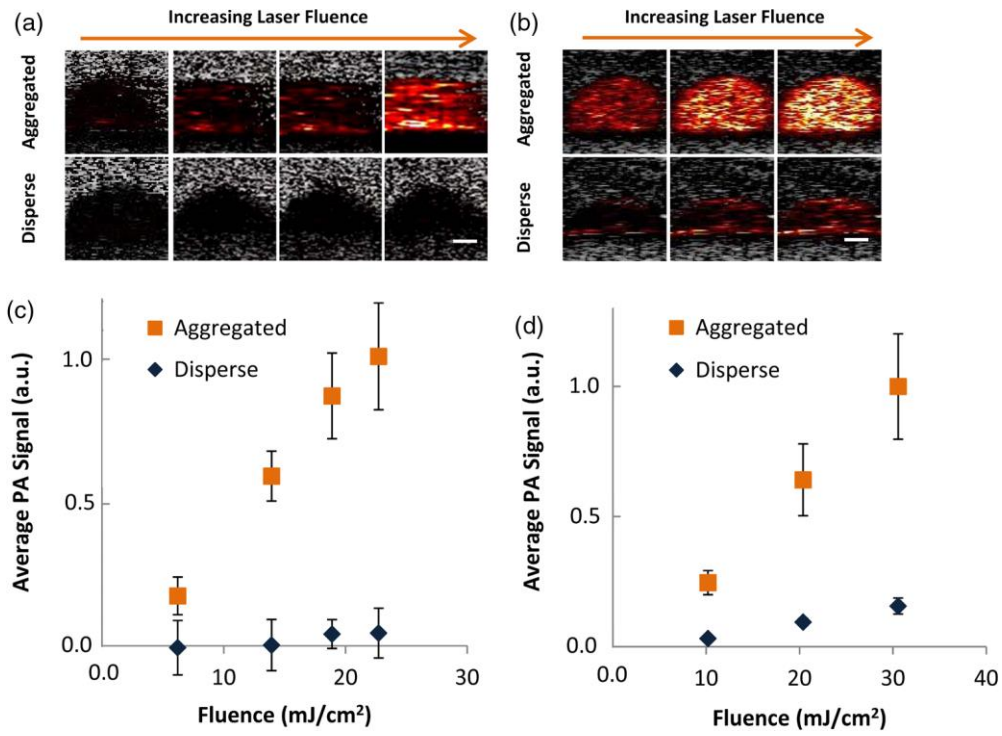

Figure 1.4: Photoacoustic signal of the aggregated and disperse nanoparticles as a function of fluence. (a) silica-coated gold nanorods at 3.7×10^{11} nanoparticles/mL and (b) silica-coated gold nanosphere at 3.5×10^{12} nanoparticles/mL [104].

1.3 Overall Research Goals

The overall goal of this work is to demonstrate a novel imaging method using nanoclusters as PA contrast agents to validate *in vivo* molecular PA images to diagnose cancerous tissue. In Chapter 2, the design and characterization of photothermal stimuli-responsive nanoclusters is described. The photoacoustic signal enhancement from clustering of nanoparticles is demonstrated.

In Chapter 3, photoacoustic signal from of photothermal stimuli-responsive nanoclusters is explored on an *ex vivo* animal model. To investigate their dynamic behavior

and repeatability, a continuous-wave (CW) laser is periodically turned on and off to heat the nanoclusters up.

In Chapter 4, biodegradable nanoclusters which consist of sub-5nm primary gold nanoparticle stabilized by biodegradable polymer are introduced and characterized. Photoacoustic signal is analyzed quantitatively from a tissue mimicking phantom. In addition, the photothermal stability of different sizes of nanoclusters is investigated. *In vitro* and *in vivo* experiments are performed to detect tumors using antibodies conjugated to biodegradable nanoclusters on cancer cells. A tissue mimicking phantom with the inclusion of cells labeled with anti-EGFR (epidermal growth factor receptor) nanoclusters is prepared for photoacoustic signal measurement. In addition, mice are subcutaneously inoculated with EGFR expressing human A431 cells and EGFR-negative human MDA-MB-435 cells are prepared and imaged before and after the injection of the antibody conjugated nanoclusters.

Finally, Chapter 5 lists the overall conclusion and future directions.

1.4 REFERENCES

1. R. Siegel, E. Ward, O. Brawley, and A. Jemal, "Cancer statistics, 2011," CA: A Cancer Journal for Clinicians (2011).

2. K. Doi, "Current status and future potential of computer-aided diagnosis in medical imaging," British Journal of Radiology **78**, s3-s19 (2005).

3. H. N. Wagner Jr and P. S. Conti, "Advances in medical imaging for cancer diagnosis and treatment," Cancer **67**, 1121-1128 (1991).

4. C. M. C. Tempany and B. J. McNeil, "Advances in biomedical imaging," JAMA: The Journal of the American Medical Association **285**, 562-567 (2001).

5. R. Weissleder and M. J. Pittet, "Imaging in the era of molecular oncology," Nature **452**, 580-589 (2008).

6. R. Weissleder, "Molecular imaging in cancer," Science's STKE **312**, 1168 (2006).

7. R. Weissleder, "Molecular Imaging: Exploring the Next Frontier1," Radiology **212**, 609-614 (1999).

8. R. Weissleder, "Scaling down imaging: molecular mapping of cancer in mice," Nature Reviews Cancer **2**, 11-18 (2002).

9. L. V. Wang and S. Hu, "Photoacoustic tomography: *in vivo* imaging from organelles to organs," Science **335**, 1458-1462 (2012).

10. S. Y. Emelianov, P. C. Li, and M. O'Donnell, "Photoacoustics for molecular imaging and therapy," Physics today **62**, 34 (2009).

11. G. P. Luke, D. Yeager, and S. Y. Emelianov, "Biomedical Applications of Photoacoustic Imaging with Exogenous Contrast Agents," Annals of biomedical engineering, 1-16 (2012).

12. S. Mallidi, G. P. Luke, and S. Emelianov, "Photoacoustic imaging in cancer detection, diagnosis, and treatment guidance," Trends in biotechnology (2011).

13. L. V. Wang, "Prospects of photoacoustic tomography," Medical Physics **35**, 5758 (2008).

14. P. Beard, "Biomedical photoacoustic imaging," Interface Focus **1**, 602-631 (2011).

15. A. Zerda, J. W. Kim, E. I. Galanzha, S. S. Gambhir, and V. P. Zharov, "Advanced contrast nanoagents for photoacoustic molecular imaging, cytometry, blood test and photothermal theranostics," Contrast Media & Molecular Imaging **6**, 346-369 (2011).

16. E. I. Galanzha and V. P. Zharov, "Photoacoustic flow cytometry," Methods **57**, 280-296 (2012).

17. V. V. Tuchin, A. Tárnok, and V. P. Zharov, "*In vivo* flow cytometry: a horizon of opportunities," Cytometry Part A **79**, 737-745 (2011).

18. T. Harrison, J. C. Ranasinghesagara, H. Lu, K. Mathewson, A. Walsh, and R. J. Zemp, "Combined photoacoustic and ultrasound biomicroscopy," Optics Express **17**, 22041-22046 (2009).

19. J. J. Niederhauser, M. Jaeger, R. Lemor, P. Weber, and M. Frenz, "Combined ultrasound and optoacoustic system for real-time high-contrast vascular imaging *in vivo*," Medical Imaging, IEEE Transactions on **24**, 436-440 (2005).

20. S. Park, S. Mallidi, A. B. Karpiouk, S. Aglyamov, and S. Y. Emelianov, "Photoacoustic imaging using array transducer," in *SPIE Photonics West*, 2007), 643714.

21. S. Emelianov, S. Aglyamov, A. Karpiouk, S. Mallidi, S. Park, S. Sethuraman, J. Shah, R. Smalling, J. Rubin, and W. Scott, "Synergy and Applications of Combined Ultrasound, Elasticity, and Photoacoustic Imaging," in *IEEE International Ultrasonics Symposium*, (IEEE, 2006), 405-415.

22. C. Bremer, V. Ntziachristos, and R. Weissleder, "Optical-based molecular imaging: contrast agents and potential medical applications," European radiology **13**, 231-243 (2003).

23. J. M. Perez, L. Josephson, and R. Weissleder, "Use of magnetic nanoparticles as nanosensors to probe for molecular interactions," ChemBioChem **5**, 261-264 (2004).

24. S. S. Gambhir, "Molecular imaging of cancer with positron emission tomography," Nature Reviews Cancer **2**, 683-693 (2002).

25. S. R. Meikle, P. Kench, M. Kassiou, and R. B. Banati, "Small animal SPECT and its place in the matrix of molecular imaging technologies," Physics in medicine and biology **50**, R45 (2005).

26. A. G. Bell, "Production of sound by radiant energy," Journal of the Franklin Institute **111**, 401-428 (1881).

27. A. Rosencwaig and A. Gersho, "Theory of the photoacoustic effect with solids," Journal of applied physics **47**, 64-69 (1976).

28. R. C. Gray and A. J. Bard, "Photoacoustic spectroscopy applied to systems involving photoinduced gas evolution or consumption," Analytical Chemistry **50**, 1262-1265 (1978).

29. T. Bowen, "Radiation-Induced Thermoacoustic Soft Tissue Imaging," in *1981 Ultrasonics Symposium*, 1981), 817-822.

30. A. A. Oraevsky, S. L. Jacques, R. O. Esenaliev, and F. K. Tittel, *Time-Resolved Optoacoustic Imaging in Layered Biological Tissues*, Advances in Optical Imaging and Photon Migration (Academic Press, New York, 1994), Vol. 21, pp. 161-165.

31. R. A. Kruger and P. Y. Liu, "Photoacoustic ultrasound: Pulse production and detection in 0.5% Liposyn," Medical physics **21**, 1179-1184 (1994).

32. X. Wang, Y. Pang, G. Ku, X. Xie, G. Stoica, and L. V. Wang, "Noninvasive laser-induced photoacoustic tomography for structural and functional *in vivo* imaging of the brain," Nat Biotech **21**, 803-806 (2003).

33. A. C. Tam, "Applications of photoacoustic sensing techniques," Reviews of Modern Physics **58**, 381-431 (1986).

34. L. Wang, *Photoacoustic Imaging and Spectroscopy*, Optical Science and Engineering (CRC Press, 2009).

35. R. Siphanto, K. Thumma, R. Kolkman, T. G. Leeuwen, F. F. M. Mul, J. W. Neck, L. N. A. Adrichem, and W. Steenbergen, "Serial nonivasive photoacoustic imaging of neovascularization in tumor angiogenesis," Optics express **13**, 89-95 (2005).

36. Y. Lao, D. Xing, S. Yang, and L. Xiang, "Noninvasive photoacoustic imaging of the developing vasculature during early tumor growth," Phys Med Biol **53**, 4203-4212 (2008).

37. G. Ku, X. Wang, X. Xie, G. Stoica, and L. V. Wang, "Imaging of tumor angiogenesis in rat brains *in vivo* by photoacoustic tomography," Applied optics **44**, 770-775 (2005).

38. R. O. Esenaliev, A. A. Karabutov, and A. A. Oraevsky, "Sensitivity of laser opto-acoustic imaging in detection of small deeply embedded tumors," Selected Topics in Quantum Electronics, IEEE Journal of **5**, 981-988 (1999).

39. G. Ku and L. V. Wang, "Deeply penetrating photoacoustic tomography in biological tissues enhancedwith an optical contrast agent," Opt. Lett. **30**, 507-509 (2005).

40. S. Y. Emelianov, S. R. Aglyamov, A. B. Karpiouk, S. Mallidi, S. Park, S. Sethuraman, J. Shah, R. W. Smalling, J. M. Rubin, and W. G. Scott, "1E-5 Synergy and Applications of Combined Ultrasound, Elasticity, and Photoacoustic Imaging (Invited)," in *Ultrasonics Symposium, 2006. IEEE*, 2006), 405-415.

41. L. V. Wang, "Multiscale photoacoustic microscopy and computed tomography," Nature photonics **3**, 503-509 (2009).

42. A. A. Oraevsky and A. A. Karabutov, *Optoacoustic tomography. In Biomedical Photonics Handbook* (CRC Press, Boca Raton, Florida, 2003), pp. 34/31–34/34.

43. M. Xu and L. V. Wang, "Analytic explanation of spatial resolution related to bandwidth and detector aperture size in thermoacoustic or photoacoustic reconstruction," Physical Review E **67**, 056605 (2003).

44. K. Maslov, H. F. Zhang, S. Hu, and L. V. Wang, "Optical-resolution photoacoustic microscopy for *in vivo* imaging of single capillaries," Opt. Lett. **33**, 929-931 (2008).

45. J. Laufer, P. Johnson, E. Zhang, B. Treeby, B. Cox, B. Pedley, and P. Beard, "*In vivo* preclinical photoacoustic imaging of tumor vasculature development and therapy," Journal of Biomedical Optics **17**, 056016-056011 (2012).

46. H. F. Zhang, K. Maslov, G. Stoica, and L. V. Wang, "Functional photoacoustic microscopy for high-resolution and noninvasive *in vivo* imaging," Nature biotechnology **24**, 848-851 (2006).

47. K. Maslov, H. F. Zhang, S. Hu, and L. V. Wang, "Optical-resolution photoacoustic microscopy for *in vivo* imaging of single capillaries," Opt Lett **33**, 929-931 (2008).

48. M.-L. Li, J.-T. Oh, X. Xie, G. Ku, W. Wang, C. Li, G. Lungu, G. Stoica, and L. V. Wang, "Simultaneous molecular and hypoxia imaging of brain tumors *in vivo* using spectroscopic photoacoustic tomography," Proceedings of the Ieee **96**, 481-489 (2008).

49. J.-T. Oh, M.-L. Li, H. F. Zhang, K. Maslov, G. Stoica, and L. V. Wang, "Three-dimensional imaging of skin melanoma *in vivo* by dual-wavelength photoacoustic microscopy," Journal of biomedical optics **11**, 034032-034032 (2006).

50. M. L. Li, J. T. Oh, X. Xie, G. Ku, W. Wang, C. Li, G. Lungu, G. Stoica, and L. V. Wang, "Simultaneous molecular and hypoxia imaging of brain tumors *in vivo* using spectroscopic photoacoustic tomography," Proceedings of the IEEE **96**, 481-489 (2008).

51. X. Yang, E. W. Stein, S. Ashkenazi, and L. V. Wang, "Nanoparticles for photoacoustic imaging," Wiley Interdisciplinary Reviews: Nanomedicine and Nanobiotechnology **1**, 360-368 (2009).

52. L. S. Bouchard, M. S. Anwar, G. L. Liu, B. Hann, Z. H. Xie, J. W. Gray, X. Wang, A. Pines, and F. F. Chen, "Picomolar sensitivity MRI and photoacoustic imaging of cobalt nanoparticles," Proceedings of the National Academy of Sciences **106**, 4085 (2009).

53. Y. Wang, X. Xie, X. Wang, G. Ku, K. L. Gill, D. P. O'Neal, G. Stoica, and L. V. Wang, "Photoacoustic tomography of a nanoshell contrast agent in the *in vivo* rat brain," Nano letters **4**, 1689-1692 (2004).

54. M. Xu and L. V. Wang, "Photoacoustic imaging in biomedicine," Review of scientific instruments **77**, 041101 (2006).

55. K. Homan, S. Kim, Y. S. Chen, B. Wang, S. Mallidi, and S. Emelianov, "Prospects of molecular photoacoustic imaging at 1064 nm wavelength," Optics letters **35**, 2663-2665 (2010).

56. X. Yang, S. E. Skrabalak, Z. Y. Li, Y. Xia, and L. V. Wang, "Photoacoustic tomography of a rat cerebral cortex *in vivo* with Au nanocages as an optical contrast agent," Nano letters **7**, 3798-3802 (2007).

57. A. Agarwal, S. Huang, M. ODonnell, K. Day, M. Day, N. Kotov, and S. Ashkenazi, "Targeted gold nanorod contrast agent for prostate cancer detection by photoacoustic imaging," Journal of applied physics **102**, 064701-064701-064704 (2007).

58. Y. S. Chen, W. Frey, S. Kim, P. Kruizinga, K. Homan, and S. Emelianov, "Silica-coated gold nanorods as photoacoustic signal nanoamplifiers," Nano letters (2011).

59. S. Mallidi, T. Larson, J. Aaron, K. Sokolov, and S. Emelianov, "Molecular specific optoacoustic imaging with plasmonic nanoparticles," Opt. Express **15**, 6583-6588 (2007).

60. S. Mallidi, T. Larson, J. Tam, P. P. Joshi, A. Karpiouk, K. Sokolov, and S. Emelianov, "Multiwavelength photoacoustic imaging and plasmon resonance coupling of gold nanoparticles for selective detection of cancer," Nano letters **9**, 2825-2831 (2009).

61. C. Kim, E. C. Cho, J. Chen, K. H. Song, L. Au, C. Favazza, Q. Zhang, C. M. Cobley, F. Gao, and Y. Xia, "*In vivo* molecular photoacoustic tomography of melanomas targeted by bioconjugated gold nanocages," ACS nano (2010).

62. D. Pan, M. Pramanik, A. Senpan, X. Yang, K. H. Song, M. J. Scott, H. Zhang, P. J. Gaffney, S. A. Wickline, and L. V. Wang, "Molecular photoacoustic tomography with colloidal nanobeacons," Angewandte Chemie **121**, 4234-4237 (2009).

63. E. I. Galanzha, J. W. Kim, and V. P. Zharov, "Nanotechnology-based molecular photoacoustic and photothermal flow cytometry platform for *in-vivo* detection and killing of circulating cancer stem cells," Journal of biophotonics **2**, 725-735 (2009).

64. A. De La Zerda, C. Zavaleta, S. Keren, S. Vaithilingam, S. Bodapati, Z. Liu, J. Levi, B. R. Smith, T. J. Ma, and O. Oralkan, "Carbon nanotubes as photoacoustic molecular imaging agents in living mice," Nature nanotechnology **3**, 557-562 (2008).

65. I. H. El-Sayed, X. Huang, and M. A. El-Sayed, "Surface plasmon resonance scattering and absorption of anti-EGFR antibody conjugated gold nanoparticles in cancer diagnostics: applications in oral cancer," Nano letters **5**, 829-834 (2005).

66. J. A. Copland, M. Eghtedari, V. L. Popov, N. Kotov, N. Mamedova, M. Motamedi, and A. A. Oraevsky, "Bioconjugated gold nanoparticles as a molecular based contrast agent: implications for imaging of deep tumors using optoacoustic tomography," Molecular Imaging & Biology **6**, 341-349 (2004).

67. E. I. Galanzha, E. V. Shashkov, T. Kelly, J. W. Kim, L. Yang, and V. P. Zharov, "*In vivo* magnetic enrichment and multiplex photoacoustic detection of circulating tumour cells," Nature nanotechnology **4**, 855-860 (2009).

68. D. Razansky, C. Vinegoni, and V. Ntziachristos, "Multispectral photoacoustic imaging of fluorochromes in small animals," Optics letters **32**, 2891-2893 (2007).

69. R. Ma, A. Taruttis, V. Ntziachristos, and D. Razansky, "Multispectral optoacoustic tomography (MSOT) scanner for whole-body small animal imaging," Optics Express **17**, 21414-21426 (2009).

70. K. H. Song, C. Kim, K. Maslov, and L. V. Wang, "Noninvasive *in vivo* spectroscopic nanorod-contrast photoacoustic mapping of sentinel lymph nodes," European journal of radiology **70**, 227-231 (2009).

71. C. L. Bayer, Y. S. Chen, S. Kim, S. Mallidi, K. Sokolov, and S. Emelianov, "Multiplex photoacoustic molecular imaging using targeted silica-coated gold nanorods," Biomedical optics express **2**, 1828-1835 (2011).

72. S. Kim, Y. S. Chen, G. P. Luke, and S. Y. Emelianov, "*In vivo* three-dimensional spectroscopic photoacoustic imaging for monitoring nanoparticle delivery," Biomedical optics express **2**, 2540-2550 (2011).

73. W. Lu, Q. Huang, G. Ku, X. Wen, M. Zhou, D. Guzatov, P. Brecht, R. Su, A. Oraevsky, and L. V. Wang, "Photoacoustic imaging of living mouse brain vasculature using hollow gold nanospheres," Biomaterials **31**, 2617-2626 (2010).

74. K. Kim, S. W. Huang, S. Ashkenazi, M. O'Donnell, A. Agarwal, N. A. Kotov, M. F. Denny, and M. J. Kaplan, "Photoacoustic imaging of early inflammatory response using gold nanorods," Applied physics letters **90**, 223901 (2007).

75. P. C. Li, C. W. Wei, C. K. Liao, C. D. Chen, K. C. Pao, C. R. C. Wang, Y. N. Wu, and D. B. Shieh, "Photoacoustic imaging of multiple targets using gold nanorods," Ultrasonics, Ferroelectrics and Frequency Control, IEEE Transactions on **54**, 1642-1647 (2007).

76. K. Homan, S. Kim, Y.-S. Chen, B. Wang, S. Mallidi, and S. Emelianov, "Prospects of molecular photoacoustic imaging at 1064 nm wavelength," Opt. Lett. **35**, 2663-2665 (2010).

77. C. Kim, H. M. Song, X. Cai, J. Yao, A. Wei, and L. V. Wang, "*In vivo* photoacoustic mapping of lymphatic systems with plasmon-resonant nanostars," Journal of materials chemistry **21**, 2841-2844 (2011).

78. L. L. Ma, M. D. Feldman, J. M. Tam, A. S. Paranjape, K. K. Cheruku, T. A. Larson, J. O. Tam, D. R. Ingram, V. Paramita, and J. W. Villard, "Small multifunctional nanoclusters (nanoroses) for targeted cellular imaging and therapy," ACS nano **3**, 2686-2696 (2009).

79. K. H. Song, C. Kim, C. M. Cobley, Y. Xia, and L. V. Wang, "Near-infrared gold nanocages as a new class of tracers for photoacoustic sentinel lymph node mapping on a rat model," Nano letters **9**, 183-188 (2008).

80. J. W. Kim, E. I. Galanzha, E. V. Shashkov, H. M. Moon, and V. P. Zharov, "Golden carbon nanotubes as multimodal photoacoustic and photothermal high-contrast molecular agents," Nature nanotechnology **4**, 688-694 (2009).

81. Y. Jin, C. Jia, S. W. Huang, M. O'Donnell, and X. Gao, "Multifunctional nanoparticles as coupled contrast agents," Nature Communications **1**, 41 (2010).

82. C. Wang, J. Chen, T. Talavage, and J. Irudayaraj, "Gold Nanorod/Fe3O4 Nanoparticle "Nano-Pearl-Necklaces" for Simultaneous Targeting, Dual-Mode Imaging, and Photothermal Ablation of Cancer Cells," Angewandte Chemie **121**, 2797-2801 (2009).

83. K. Homan, S. Mallidi, E. Cooley, and S. Emelianov, "Combined photoacoustic and ultrasound imaging of metal nanoparticles *in vivo*," in *Nanoimaging* (Pan Stanford Publishing, Singapore, 2010).

84. V. P. Zharov, E. I. Galanzha, E. V. Shashkov, N. G. Khlebtsov, and V. V. Tuchin, "*In vivo* photoacoustic flow cytometry for monitoring of circulating single cancer cells and contrast agents," Optics letters **31**, 3623-3625 (2006).

85. K. A. Homan, M. Souza, R. Truby, G. P. Luke, C. Green, E. Vreeland, and S. Emelianov, "Silver Nanoplate Contrast Agents for *In Vivo* Molecular Photoacoustic Imaging," ACS nano, 641-650 (2012).

86. S. Bhattacharyya, S. Wang, D. Reinecke, W. Kiser Jr, R. A. Kruger, and T. R. DeGrado, "Synthesis and Evaluation of Near-Infrared (NIR) Dye− Herceptin Conjugates as Photoacoustic Computed Tomography (PCT) Probes for HER2 Expression in Breast Cancer," Bioconjugate chemistry **19**, 1186-1193 (2008).

87. G. Kim, S. W. Huang, K. C. Day, M. O'Donnell, R. R. Agayan, M. A. Day, R. Kopelman, and S. Ashkenazi, "Indocyanine-green-embedded PEBBLEs as a contrast agent for photoacoustic imaging," Journal of biomedical optics **12**, 044020 (2007).

88. K. H. Song, E. W. Stein, J. A. Margenthaler, and L. V. Wang, "Noninvasive photoacoustic identification of sentinel lymph nodes containing methylene blue *in vivo* in a rat model," Journal of biomedical optics **13**, 054033 (2008).

89. K. M. Stantz, M. Cao, B. Liu, K. D. Miller, and L. Guo, "Molecular imaging of neutropilin-1 receptor using photoacoustic spectroscopy in breast tumors," in *SPIE Photonics West*, 2010), 75641O.

90. E. V. Shashkov, M. Everts, E. I. Galanzha, and V. P. Zharov, "Quantum dots as multimodal photoacoustic and photothermal contrast agents," Nano letters **8**, 3953-3958 (2008).

91. M. Pramanik, M. Swierczewska, D. Green, B. Sitharaman, and L. V. Wang, "Single-walled carbon nanotubes as a multimodal-thermoacoustic and photoacoustic-contrast agent," Journal of biomedical optics **14**, 034018 (2009).

92. K. Kostarelos, A. Bianco, and M. Prato, "Promises, facts and challenges for carbon nanotubes in imaging and therapeutics," Nature nanotechnology **4**, 627-633 (2009).

93. L. Xiang, Y. Yuan, D. Xing, Z. Ou, S. Yang, and F. Zhou, "Photoacoustic molecular imaging with antibody-functionalized single-walled carbon nanotubes for early diagnosis of tumor," Journal of biomedical optics **14**, 021008 (2009).

94. B. T. Khuri-Yakub, X. Chen, H. Dai, and S. S. Gambhir, "Family of Enhanced Photoacoustic Imaging Agents for High-Sensitivity and Multiplexing Studies in Living Mice," ACS Nano **6**, 4694-4701 (2012).

95. K. Wilson, K. Homan, and S. Emelianov, "Biomedical photoacoustics beyond thermal expansion using triggered nanodroplet vaporization for contrast-enhanced imaging," Nature Communications **3**, 618 (2012).

96. E. Strohm, M. Rui, I. Gorelikov, N. Matsuura, and M. Kolios, "Vaporization of perfluorocarbon droplets using optical irradiation," Biomedical optics express **2**, 1432-1442 (2011).

97. K. Wilson, K. Homan, and S. Emelianov, "Synthesis of a dual contrast agent for ultrasound and photoacoustic imaging," in *SPIE Photonics West*, 2010), 75760M.

98. M. Mehrmohammadi, S. J. Yoon, D. Yeager, and S. Y. Emelianov, "Photoacoustic Imaging for Cancer Detection and Staging," Current molecular imaging **2**, 89-105 (2013).

99. B. Kang, D. Yu, Y. Dai, S. Chang, D. Chen, and Y. Ding, "Cancer-Cell Targeting and Photoacoustic Therapy Using Carbon Nanotubes as “Bomb” Agents," Small **5**, 1292-1301 (2009).

100. M. L. Li, J. C. Wang, J. A. Schwartz, K. L. Gill-Sharp, G. Stoica, and L. V. Wang, "*In-vivo* photoacoustic microscopy of nanoshell extravasation from solid tumor vasculature," Journal of biomedical optics **14**, 010507 (2009).

101. T. Thomas, P. Dale, R. Weight, U. Atasoy, J. Magee, and J. Viator, "Photoacoustic detection of breast cancer cells in human blood," significance **1**, 2 (2008).

102. J. A. Viator, S. Gupta, B. S. Goldschmidt, K. Bhattacharyya, R. Kannan, R. Shukla, P. S. Dale, E. Boote, and K. Katti, "Gold nanoparticle mediated detection of prostate cancer cells using photoacoustic flowmetry with optical reflectance," Journal of Biomedical Nanotechnology **6**, 187-191 (2010).

103. W. J. Akers, C. Kim, M. Berezin, K. Guo, R. Fuhrhop, G. M. Lanza, G. M. Fischer, E. Daltrozzo, A. Zumbusch, and X. Cai, "Noninvasive photoacoustic and fluorescence sentinel lymph node identification using dye-loaded perfluorocarbon nanoparticles," ACS nano **5**, 173 (2011).

104. C. L. Bayer, S. Y. Nam, Y.-S. Chen, and S. Y. Emelianov, "Photoacoustic signal amplification through plasmonic nanoparticle aggregation," J Biomed Opt, submitted (2012).

Chapter 2: Design, Synthesis and Characterization of Photothermal Stimuli-responsive Nanoclusters

Photoacoustic imaging is based on a process that converts photons to acoustic waves through thermal-elastic expansion of imaging targets by pulsed laser heating [1-4]. This process is dominated by optical absorption properties of materials, therefore, to develop a stimuli-responsive photoacoustic nanoparticle, one approach is to create a particle whose optical absorption varies with the stimulus signals. Stimuli-responsive fluorophores have been widely used in fluorescent imaging and partially adapted for photoacoustic imaging [5-8]. However, these fluorescent probes are not designed for releasing drugs.

Another approach, instead, is to induce photoacoustic signal change from stimuli-responsive particle aggregation. Nanoparticle photoacoustic contrast agents, unlike homogeneous medium, are optically and thermally heterogeneous after heated by external source. Thermal energy generated by optical absorption from the nanoparticles will diffuse out to their surrounding liquid. Since the particles are small, their thermal relaxation and diffusion time are much shorter than the duration of the illuminated laser pulse [9]. Once the nanoparticles move and their interparticle distances vary so that their heat profiles change from overlapping to non-overlapping or vice versa, their photoacoustic intensity will change upon this dynamics [10]. Therefore, a stimuli-responsive photoacoustic probe can be created by a nanocluster, whose particle packing density can vary dynamically in a controllable manner. It is known that many stimuli-responsive nanogels can recognize stimuli such as specific chemicals, pH value, temperature or light, and respond by changing volumes of particles [11, 12]. If one can incorporate photoacoustic contrast agents, such as

gold nanoparticles, into such volume changing stimuli-responsive nanogels, a dynamic contrast agent that helps to trace the stimulus responses can be created.

In this chapter, photothermal stimuli-responsive nanoclusters are designed and characterized as photoacoustic contrast agents. The synthesis of the nanoclusters is first described. The photoacoustic signal enhancement from clustering of nanoparticles is demonstrated by altering the volume of nanoclusters. The photoacoustic signals from these nanoclusters are also compared to that of their primary particles.

2.1 MATERIALS AND METHODS

N-Isopropylacrylamide (NIPAm), cross-linking agent N-N'-methylene-bis-acrylamide (BIS), and an initiator potassium persulfate (KPS), copper(II) chloride ($CuCl_2$), sodium sulfide ($Na_2S•9H_2O$), sodium citrate, and methoxy-PEG-thiol (PEG-SH, MW 5000) were purchased from Sigma-Aldrich (St. Louis, MO, USA).

2.1.1 Nanoparticle Synthesis

Poly(n-isopropylacrylamide) (PNIPAM) Nanogel Synthesis

PNIPAM nanogel were prepared via free radical precipitation polymerization[13]. An aqueous solution (90 mL) containing monomer, N-isopropylacrylamide (12.5 mole), and cross-linker, N-N'-methylene-bis-acrylamide was placed in a 250 mL three necks flask with a reflux condenser. The solution was de-gassed under argon purge with mechanically stirring at 300 rpm for 15 minutes and then heated to 70 °C in water bath. At this point, 10 mL of potassium persulfate solution (5 wt %) was injected in the flask through needle. Following synthesis, the PNIPAM nanogels were purified several times by centrifugation (20000g, 30 min at 20°C) and redispersed in ultrafiltrated (18 MΩcm, Thermo Scientific Barnstead Diamond water purification systems) deionized water.

Five nm Gold Nanoparticles

To synthesize citrate-stabilized 5 nm gold nanospheres, 500 mL of nanopure water was heated to 97°C in an Erlenmeyer flask while covered. While stirring, add 1 mL of 1% of $HAuCl_4$ solution. One minute later, 1 mL of 1% of sodium citrate solution was added to the solution. After one minute, 1 mL of 0.075% $NaBH_4$ in a 1% sodium citrate solution was added to the solution. After 5 minutes of stirring, the solution is transferred to an ice bath to cool to room temperature.

Copper Sulfide (CuS) Nanoparticle Synthesis

CuS nanospheres (NSs) were synthesized by reacting copper(II) chloride ($CuCl_2$) with sodium sulfide (Na_2S)[14]. In particular, 1 mL of Na_2S solution (1 M) was added to 1L of an aqueous solution of $CuCl_2$ (1 mM) and sodium citrate (0.68 mM), under stirring at room temperature for 5 minutes. The resultant brown color reaction mixture was, then, heated to 90 °C on a hotplate and stirred for another 15 min until a dark green solution was obtained. To introduce a polyethylene glycol (PEG) coating, about 1 mg of NH_2-PEG-SH (5 kDa) was added into the citrate CuS NS solution. The reaction was stirred at room temperature overnight.

PNIPAM-AuNS Nanocluster Synthesis

Gold nanospheres in 5 nm diameter were prepared as described previously. The gold nanospheres were concentrated to OD of 5 using Amicon centrifugal filter tubes with a molecular weight cutoff of 100 kDa (EMD Millipore, Billerica, MA, USA) at 1500 × g for 5 minutes. A mixture of 100 μL of concentrated AuNSs and 1 mL of the PNIPAM nanogels (2.0 wt% solid) were poured in a tube. The mixture was put into a shaker for overnight at room temperature and then washed several times by centrifugation at 3000 g for 10

minutes. The loading concentration is controlled by varying the concentration ratio of AuNSs to PNIPAM.

PNIPAM-CuS Nanocluster Synthesis

A mixture of CuS NSs and 1 mL of the PNIPAM nanogels (2.0 wt% solid) synthesized by the previously described protocol were poured in a tube. The mixture was put into a shaker for overnight at room temperature and then washed several times by centrifugation at 3000 g for 10 minutes. The loading concentration is controlled by varying the concentration ratio of CuS NSs to PNIPAM.

Photoacoustic Signal Characterization

To investigate the PA performance of PNIPAM-AuNS nanoclusters, their PA signals were characterized using a photoacoustic imaging system; the results were compared with the PA signals generated from their individual AuNSs. The extinction of PNIPAM-AuNS and AuNS solutions were matched using UV-Vis spectroscopy. An ultrasound and photoacoustic imaging system (Vevo LAZR, VisualSonics, Inc.) with a 20 MHz array ultrasound transducer (MS250, VisualSonics, Inc.) was used to capture the photoacoustic signals at the wavelength of 700 nm. An optical fiber bundle for light delivery is integrated with the ultrasound transducer. The phantoms were made by first mixing each solution in 1:1 volume ratio with phenol-free Matrigel (Corning), a gelatinous protein that mimics the complex extracellular environment found in many tissues. Then, both mixtures were injected separately into thin wall polyethylene tubes (1 mm outer diameter and 0.6 mm inner diameter) and mounted on a plastic scaffold. The scaffold along with the tubes was placed in a water tank during imaging. The water inlet and outlet of the tank were connected to a temperature-controlled water circulator to maintain a constant and uniform temperature during imaging. The transducer with the fiber bundle was

mounted on top of the phantom with a fixed distance of 1 cm from the transducer to the tube inclusions, which was aligned perpendicularly with respect to the imaging plane of the transducer. Seven-nanosecond laser pulses produced by a wavelength-tunable optical parametric oscillator (Premiscan, GWU, Inc.) were used to excite photoacoustic signals. The laser fluence at the output of the fiber bundle was adjusted to 13 mJ/cm^2. During the imaging, the water temperature was initially set at 21°C and gradually increased to 40°C by every 2°C, then it was cooled down to 21°C gradually. The water temperature stayed at each temperature for at least 5 minute before the PA images were recorded to allow sufficient thermal diffusion in samples. At each temperature, 300 PA signals of the phantom were collected for averaging. To plot the photoacoustic signal intensities as a function of temperature of each sample, the maximum PA intensities were selected at each temperature. These 300 signals were averaged and the standard deviation was calculated. The PA performance of PNIPAM-CuS comparing to pure CuS nanoparticle was measured with a similar manner at the wavelength of 970 nm.

2.2 CHARACTERIZATION OF PNIPAM NANOCLUSTER

To demonstrate the design, a nanosize photothermal stimuli-responsive polymer, poly(n-isopropylacrylamide) hydrogel (PNIPAM), was selected as the model vehicle to carry and control the nanoparticle aggregation [15, 16]. The most appealing property of PNIPAM particle is that their volume rapidly reduces (de-swelling state or shrink state) when temperature rises above their lower critical solution temperature (LCST), a phenomenon that is caused by phase transition of hydrophobic moieties of polymer chain [16]. Moreover, this process is reversible: when temperature decreases, their volume will be recovered (swelling state). The LCST temperature of PNIPAM is 32°C, but it can be increased to match the biological temperature by co-polymerizing hydrophilic monomers

into the polymer matrix [17, 18]. Besides copolymers, some PNIPAM derivatives, such as poly (n-isopropylmethacrylamide) (PNIPMAM) also possess LCST at 38°C to 44°C [19]. PNIPAM based hydrogels have been widely used for controlling release of therapeutic agents such as genes and drugs [20, 21], tissue engineering, tunable catalysis, and sensing [22], therefore ideal for this purpose.

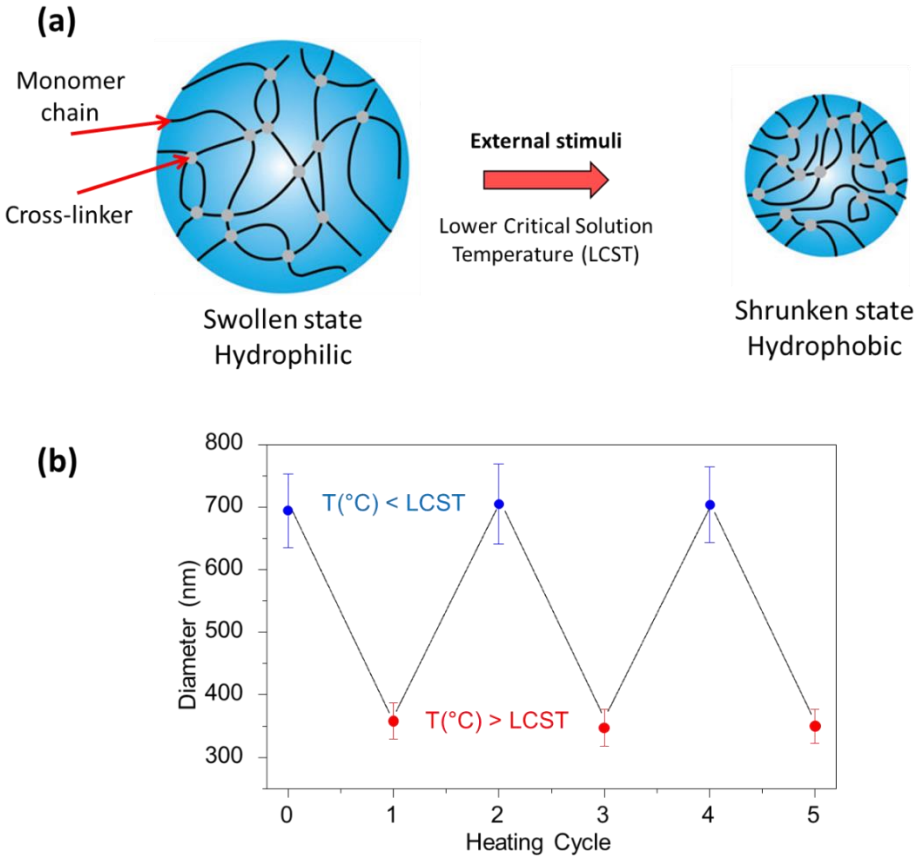

Figure 2.1: (a) Structure of PNIPAM nanogels (b) Averaged diameter of PNIPAM below and above LCST.

Cross-linked PNIPAM nanogels were synthesized as described previously. The size of nanogels is average 700 nm in diameter at room temperature. After heating above LCST, these nanogels shrink to 350 nm in diameter (Figure 2.1b), corresponding to 12.5% of their original volume. Two commonly used photoacoustic contrast agents, gold nanosphere (AuNSs) and copper sulfide nanospheres (CuS NSs), are separately loaded into this nanogel to form two types of stimuli-responsive photoacoustic contrast agents [14, 23-26]. AuNSs are one of the most popular photoacoustic contrast agents because of their large optical cross section and inert chemical reactivity. Although the optical cross section of CuS NSs is lower than that of AuNSs, their inherent absorption peak close to the tissue second optical window (~1064 nm) make them also attractive photoacoustic contrast agents [27].

2.3 Result and Discussions

To investigate morphology changes of these PNIPAM-contrast agents nanoclusters caused by thermal stimulation, TEM samples were prepared at the temperatures below and above LCST, respectively. TEM images (Figure 2.2a-b and Figure 2.3a-b) at different temperature illustrate the swelling and deswelling state of these nanoclusters.

Above LCST, the volume reduction of these nanoclusters results in changes of their optical properties. Optical absorption of nanoclusters is determined by plasmon resonance of AuNSs and plasmonic coupling between individual AuNSs. AuNSs have a plasmon peak around 520 nm due to the nature of gold and geometry. However, plasmonic coupling is strongly affected by the separation distance of AuNSs. The reduced separation between the individual AuNSs results in stronger plasmonic coupling and broadening of plasmonic peak. Indeed, the UV-Vis results (Figure 2.2c) show broadening of the spectrum.

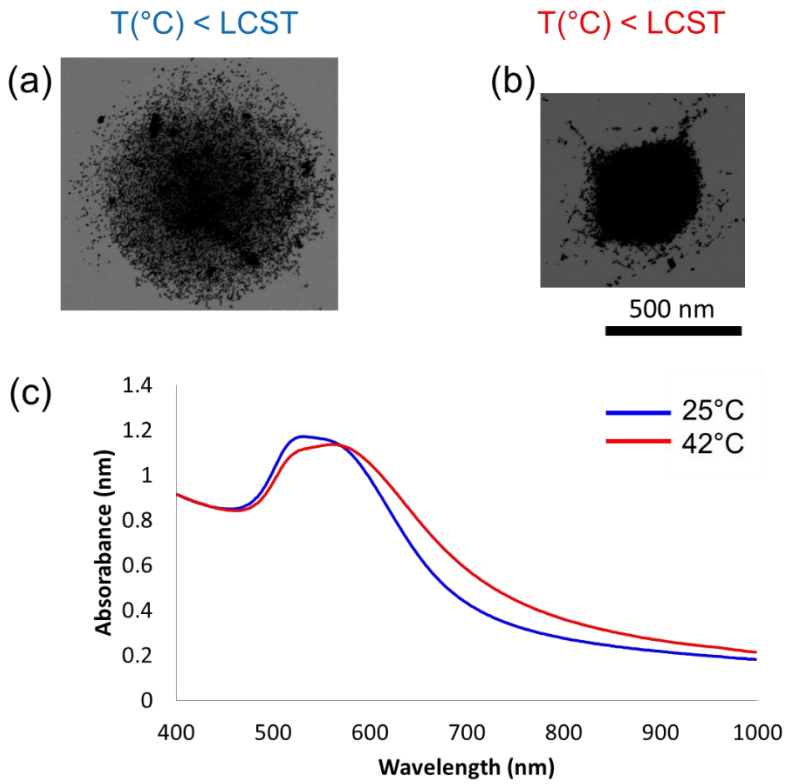

Figure 2.2: (a) TEM images of PNIPAM-AuNS nanoclusters prepared at temperature below LCST. (b) TEM images of PNIPAM-AuNS nanoclusters prepared at temperature above LCST. (c) UV-Vis spectra of PNIPAM-AuNS at 25˚C (blue curves) and 42˚C (red curves). Scale bars are 500 nm (a, b).

Unlike AuNSs, CuS NSs are semiconductor nanoparticles; their optical absorption is caused by electron transition overcoming their bandgap [14]. When CuS nanoparticles are brought closer to each other, the increase in their extinction is mainly due to the increased Rayleigh scattering of the nanoclusters (Figure 2.3a-b).

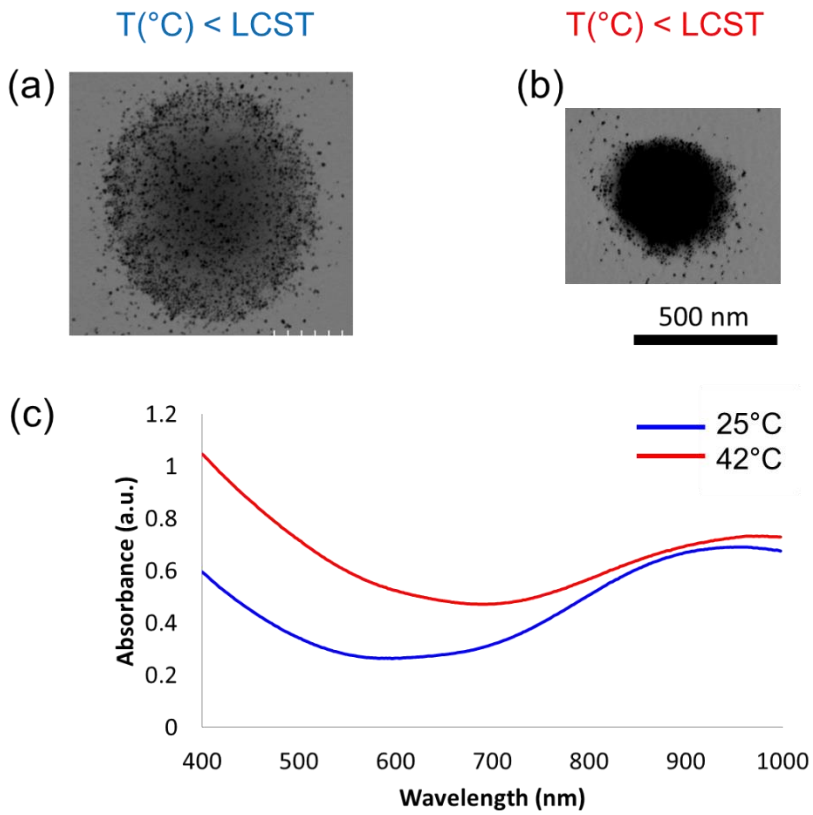

Figure 2.3: (a) TEM images of PNIPAM-CuS nanoclusters prepared at temperature below LCST. (b) TEM images of PNIPAM-CuS nanoclusters prepared at temperature above LCST. (c) UV-Vis spectra of PNIPAM-CuS at 25˚C (blue curves) and 42˚C (red curves). Scale bars are 500 nm (a, b).

The morphology change of the nanoclusters can induce different photoacoustic responses. To demonstrate this, photoacoustic signal of these PNIPAM-nanoparticle nanoclusters using a customized photoacoustic imaging system was obtained. Photoacoustic intensities from pure AuNS and PNIPAM-AuNS solutions are compared. AuNS concentrations are first matched through UV-Vis spectroscopy. Photoacoustic signal as a function of the solution temperature between 22°C and 44°C (Figure 2.4a) was recorded. The results show the PNIPAM-AuNS solution produced higher photoacoustic

intensity than pure AuNS solution even below LCST. This photoacoustic signal enhancement is attributed to the randomly occurred thermal profile overlapping that creates a higher temperature gradient. Also at this temperature range, in both solutions, the photoacoustic intensity increases linearly with temperature. This increment comes from the thermal expansion coefficient of water that increases linearly in the range of this experiment from 21°C to 40°C [9]. When temperature is crossing LCST, in pure AuNS solution, the photoacoustic intensity keeps its linear trend, whereas in PNIPAM-AuNS solution, an abrupt intensity increase is observed. This abrupt increment happens from 28 °C to 32 °C, close to the LCST of PNIPAM, corresponding the phase transition of PNIPAM, the sudden density increment of the loaded AuNS (or reduced particle spacing) causes the photoacoustic signal enhancement. Above the LCST temperature range (from 32°C to 40°C), the photoacoustic intensity from PNIPAM-AuNS increases linearly with temperature again. As a result, its photoacoustic enhancement factor increases to more than 45 times compared to pure AuNS solution at 36 °C at 700 nm. This result suggests that this unique photoacoustic signature caused by morphology changes of the nanoclusters can be used to monitor the dynamic morphology changes of the nanoclusters, a critical capability for image-guided controlled releasing. Besides, since this shrinking process of the nanoclusters is reversible, when the temperature is cooled down, the photoacoustic intensity reversely follows the curve back to its original intensity (Figure 2.4a).

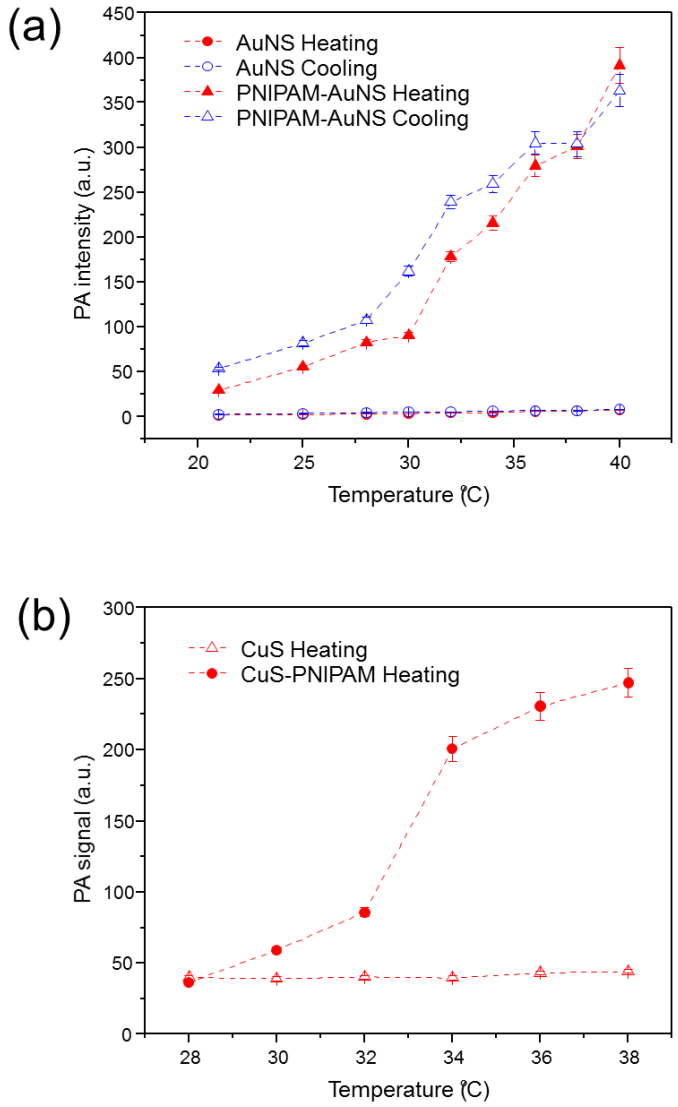

Figure 2.4: Photoacoustic signal of PNIPAM-nanoparticle nanoclusters as a function of temperatures (a) Comparison of photoacoustic intensities for PNIPAM-AuNS and pure AuNS with a heating and cooling cycle, indicating the curve retrieves back to its original PA intensity as temperature cools below LCST at the wavelength of 700 nm. Abrupt PA intensity changes are observed in both PNIMPAM-AuNS nanoclusters and (b), PNIPAM-CuS nanoclusters, whereas their pure nanoparticles (AuNS and CuS) show linear behavior with respect to temperatures at the wavelength of 970 nm.

Similarly, photoacoustic signal characterization was performed using PNIPAM-CuS nanoclusters and pure CuS nanoparticle solutions. The reason of investigating PNIPAM-CuS is their improved photothermal stability from the spherical nature of CuS, this will eventually contribute to their repeatability as reusable stimuli-responsive agents. Although the trend for photoacoustic intensity increment is similar to PNIPAM-AuNS, their signal enhancement factor is slightly different. In this case, 2 times and 5.5 times enhancements were observed below and above LCST, respectively (Figure 2.4b). This difference could be due to the inherently lower absorption cross-section of the CuS nanoparticles, which require particles to pack even more densely to achieve higher signal enhancement.

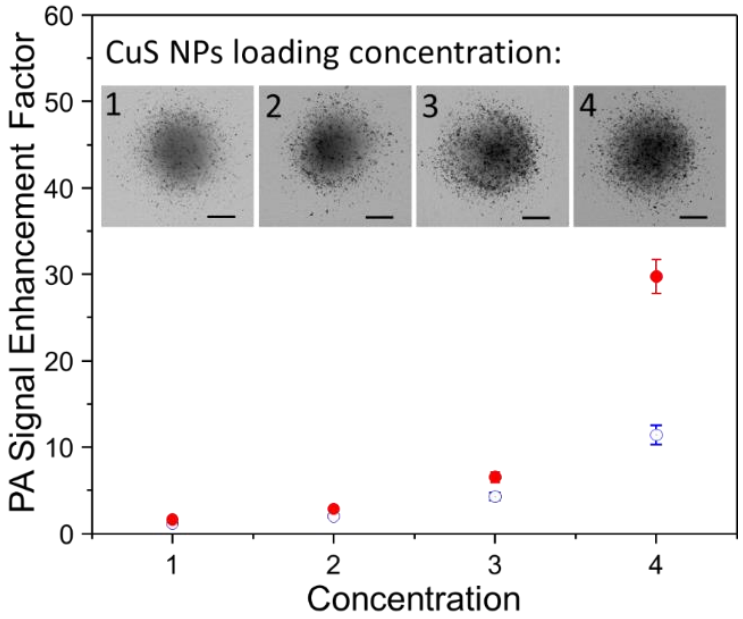

Figure 2.5: Photoacoustic signal enhancement factors as a function of loading concentrations of nanoparticles inside the nanoclusters. Photoacoustic signal enhancement factor as a function for CuS loading concentration below (blue points) and above LCST (red points). Insets show TEM images of the nanoclusters with increased loading density of CuSs. Scale bars are 250 nm.

To investigate whether photoacoustic signal enhancement can be further improved, PNIPAM-CuS with increasing loading concentrations of nanoparticles. As shown in the TEM images in insets of Figure 2.5, the CuS concentration is varied. With increased loading concentrations, PNIPAM-CuS starts to show advantages because of their small size. This small dimension allows much higher loading concentration of CuS into a single PNIPAM nanogel. As a result, much higher photoacoustic intensity increment is expected from the densely loaded PNIPAM-CuS nanoclusters. Four different loading concentrations of both PNIPAM-CuS and pure CuS nanospheres were prepared and tested their photoacoustic signal enhancement factors at 27 °C and 37°C respectively. A signal enhancement factor of 11.5 and 30 times below and above LCST were observed in the case of the highest loading concentration.

2.4 CONCLUSION

In this Chapter a new approach to visualize the dynamic stimulus responses of nanoparticles was introduced using photoacoustic imaging. A photothermal stimuli-responsive nanoparticle whose photoacoustic intensity responds to light and thermal stimuli, ideal for a therapeutic agent vehicle, was designed and synthesized. Moreover, these smart nanoclusters can generate stronger photoacoustic signals comparing to the same concentration of their inorganic individual nanoparticle. The results suggest that a photoacoustic signal is amplified when nanoparticles are clustered. Therefore, the result demonstrated that nanocluster can be an effective photoacoustic contrast agents.

2.5 REFERENCES

1. L. V. Wang and S. Hu, "Photoacoustic tomography: *in vivo* imaging from organelles to organs," Science **335**, 1458-1462 (2012).

2. A. C. Tam, "Applications of photoacoustic sensing techniques," Reviews of Modern Physics **58**, 381-431 (1986).

3. G. J. Diebold, M. I. Khan, and S. M. Park, "Photoacoustic "signatures" of particulate matter: optical poduction of acoustic monopole radiation," Science **250**, 101-104 (1990).

4. A. A. Oraevsky, S. L. Jacques, R. O. Esenaliev, and F. K. Tittel, *Laser-based optoacoustic imaging in biological tissues*, Laser-Tissue Interaction V, Proceedings Of (1994), Vol. 2134, pp. 122-128.

5. V. Ntziachristos, C.-H. Tung, C. Bremer, and R. Weissleder, "Fluorescence molecular tomography resolves protease activity *in vivo*," Nature Medicine **8**, 757-760 (2002).

6. J. Levi, S. R. Kothapalli, T.-J. Ma, K. Hartman, B. T. Khuri-Yakub, and S. S. Gambhir, "Design, synthesis, and imaging of an activatable photoacoustic probe," Journal of the American Chemical Society **132**, 11264-11269 (2010).

7. H. Kobayashi and P. L. Choyke, "Target-cancer-cell-specific activatable fluorescence imaging probes: rational design and *in vivo* applications," Accounts of Chemical Research **44**, 83-90 (2011).

8. D. R. Elias, D. L. J. Thorek, A. K. Chen, J. Czupryna, and A. Tsourkas, "*In vivo* imaging of cancer biomarkers using activatable molecular probes," Cancer Biomarkers **4**, 287-305 (2008).

9. Y.-S. Chen, W. Frey, S. Aglyamov, and S. Emelianov, "Environment-dependent generation of photoacoustic waves from plasmonic nanoparticles," Small **8**, 47-52 (2012).

10. C. L. Bayer, S. Y. Nam, Y.-S. Chen, and S. Y. Emelianov, "Photoacoustic signal amplification through plasmonic nanoparticle aggregation," BIOMEDO **18**, 016001-016001 (2013).

11. M. A. C. Stuart, W. T. S. Huck, J. Genzer, M. Mueller, C. Ober, M. Stamm, G. B. Sukhorukov, I. Szleifer, V. V. Tsukruk, M. Urban, F. Winnik, S. Zauscher, I. Luzinov, and S. Minko, "Emerging applications of stimuli-responsive polymer materials," Nature Materials **9**, 101-113 (2010).

12. S. Mura, J. Nicolas, and P. Couvreur, "Stimuli-responsive nanocarriers for drug delivery," Nature Materials **12**, 991- 1003 (2013).

13. H. G. Schild, "Poly(N-isopropylacrylamide): experiment, theory and application," Progress in Polymer Science **17**, 163-249 (1992).

14. G. Ku, M. Zhou, S. Song, Q. Huang, J. Hazle, and C. Li, "Copper sulfide nanoparticles as a new class of photoacoustic contrast agent for deep tissue imaging at 1064 nm," ACS Nano **6**, 7489-7496 (2012).

15. M. A. C. Stuart, W. T. S. Huck, J. Genzer, M. Muller, C. Ober, M. Stamm, G. B. Sukhorukov, I. Szleifer, V. V. Tsukruk, M. Urban, F. Winnik, S. Zauscher, I. Luzinov, and S. Minko, "Emerging applications of stimuli-responsive polymer materials," **9**(2010).

16. H. G. Schild, "Poly (n-isopropylacrylamide) - experiment, theory and application," Progress in Polymer Science **17**, 163-249 (1992).

17. S. Hirotsu, Y. Hirokawa, and T. Tanaka, "Volume-phase transitions of ionized N-isopropylacrylamide gels," The Journal of Chemical Physics **87**, 1392-1395 (1987).

18. G. Huang, J. Gao, Z. Hu, J. V. St. John, B. C. Ponder, and D. Moro, "Controlled drug release from hydrogel nanoparticle networks," Journal of Controlled Release **94**, 303-311 (2004).

19. D. Duracher, A. Elaissari, and C. Pichot, "Characterization of cross-linked poly(N-isopropylmethacrylamide) microgel latexes," Colloid Polym. Sci. **277**, 905-913 (1999).

20. L. Zha, B. Banik, and F. Alexis, "Stimulus responsive nanogels for drug delivery," Soft Matter **7**, 5908-5916 (2011).

21. T. Vermonden, R. Censi, and W. E. Hennink, "Hydrogels for protein delivery," Chemical Reviews **112**, 2853-2888 (2012).

22. E. Cabane, X. Zhang, K. Langowska, C. Palivan, and W. Meier, "Stimuli-responsive polymers and their applications in nanomedicine," Biointerphases **7**, 1-27 (2012).

23. P.-C. Li, C.-R. C. Wang, D.-B. Shieh, C.-W. Wei, C.-K. Liao, C. Poe, S. Jhan, A.-A. Ding, and Y.-N. Wu, "*In vivo* photoacoustic molecular imaging withsimultaneous multiple selective targeting usingantibody-conjugated gold nanorods," Opt. Express **16**, 18605-18615 (2008).

24. S. Manohar, C. Ungureanu, and T. G. Van Leeuwen, "Gold nanorods as molecular contrast agents in photoacoustic imaging: the promises and the caveats," Contrast Media & Molecular Imaging **6**, 389-400 (2011).

25. J. V. Jokerst, A. J. Cole, D. Van de Sompel, and S. S. Gambhir, "Gold nanorods for ovarian cancer detection with photoacoustic imaging and resection guidance via raman imaging in living mice," ACS Nano **6**, 10366-10377 (2012).

26. P. K. Jain, I. H. El-Sayed, and M. A. El-Sayed, "Au nanoparticles target cancer," Nano Today **2**, 18-29 (2007).

27. A. M. Smith, M. C. Mancini, and S. Nie, "Second window for *in vivo* imaging," Nature Nanotechnology **4**, 710-711 (2009).

Chapter 3: *Ex vivo* Photoacoustic Imaging of Tissue using PNIPAM-CuS Nanoclusters

Targeted delivery and controlled release of therapeutic agents is crucial to optimize treatment for many diseases. Many therapeutic agents suffer from poor pharmacokinetics, therefore, require a vehicle that can carry these agents and well control their release to disease sites. Stimuli-responsive nanogels have recently shown great promises as such vehicles, because they can dynamically respond to micro-environmental changes. To maximize the outcome of the therapy and minimize the side effects, a proper imaging technique that can guide the delivery, validate the release and later noninvasively assess the efficacy of the therapeutic agents, is highly desired. Photoacoustic imaging has been used to guide thermal-, photodynamic-, and chemo- therapies, and to assess the therapeutic outcomes, especially in cancer treatments. Many of these capabilities are achieved with the facilitation of nanoparticles as imaging contrast agents. However, few nanoparticles can serve the dual purposes as the stimuli-responsive drug release vehicle, and at the same time, as a dynamic contrast agent that can reveal their dynamic releasing processes under stimuli.

The experiments in the previous chapter were performed in an *in vitro* condition with external thermal heating. In this chapter, *ex vivo* photoacoustic imaging of a mouse tissue using PNIPAM-CuS nanoclusters is performed. The absorption peak of CuS particles is around 1000 nm, therefore, they can be imaged at the wavelength of 1064 nm. Despite lower absorption cross-section of CuS particles, there are several advantages using CuS nanoparticles over other plasmonic particles such as AuNSs or Au nanorods. First, background noise can be reduced because tissue is not absorbing as strong as in the other range [1]. Second, imaging depth can be increased because it has a low absorption and low scattering coefficients in biological tissues and a maximum allowable laser fluence is

higher [2]. In addition, one of the most reliable and cost effective Q-switched Nd:YAG laser can be used for photoacoustic imaging. However, tumor cells do not have specific optical absorption which can be differentiated from the background tissue at 1064 nm. To enhance the contrast of photoacoustic imaging, the strong contrast agents absorbing at 1064 nm are required. CuS nanoparticles are one of the promising photoacoustic contrast agents that absorb light at 1064 nm. In addition, PNIPAM-CuS nanoclusters can provide additional contrast when the temperature is above the LCST. It is known that under continuous wave (CW) laser illumination, optical absorbing nanoparticles will also increase temperature rapidly [3]. This photothermal effect has been used for localized heating to annihilate cancer cells [4] and to trigger the drug release [5-7]. It suggests the photoacoustic contrast-enhanced nanoclusters can be noninvasively turned on with external lasers.

3.1 MATERIALS AND METHODS

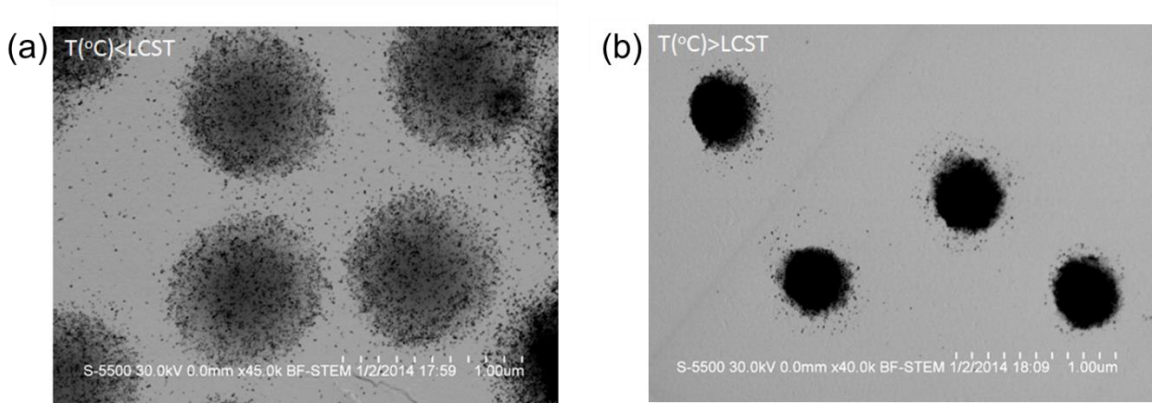

Figure 3.1: TEM images of the PNIPAM-CuS nanoclusters for *ex vivo* imaging. (a) TEM sample was prepared at temperature below LCST which illustrates the swelling state of the nanoclusters, (b) sample was prepared at temperature above LCST illustrating the de-swelling state of the nanoclusters.

The procedure to make PNIPAM-CuS nanoclusters was discussed previously in Chapter 2.1.

3.1.1 Animal Preparation

For *ex-vivo* mouse imaging, a 12 week old Nu/Nu mouse was euthanized by carbon dioxide asphyxiation followed by cerebral dislocation. The CuS and PNIPAM-CuS samples (OD = 1.8) were mixed with Matrigel (Corning Inc., New York, NY, USA) at 1:1 volume ratio and implanted subcutaneously into the flank of the mouse.

3.1.2 Ultrasound and Photoacoustic Imaging with Countinous-wave Laser Heating

The ultrasound and photoacoustic images were collected by VEVO 2100 LAZR system (Visualsonics Inc., Toronto, ON, Canada) with 20 MHz array ultrasound transducer (MS250, VisualSonics, Inc.). The photoacoustic images were collected at the wavelength of 1064 nm and the laser fluence was 23 mJ/cm^2. The mouse was immersed in a water bath and 1.6 W continuous-wave at 1064 nm Nd:YAG laser was used for heating the area where the samples were injected. The CW laser is controlled by a function generator to turn on and off by a square waveform with a 30 second period.

3.2 Results and Discussion

The photoacoustic responses of PNIPAM-CuS on an *ex-vivo* animal model (Figure 3.2a) were obtained in comparison to regular photoacoustic contrast agents (CuS NSs) (Figure 3.2b-c). To test their dynamic behavior and repeatability, The CW lasers were periodically turned on. When the CW laser is on, CuS NSs instantaneously heat up the PNIPAM matrix and causes it to shrink. As evidenced in Figure 3.3, the periodic heating causes repeatedly enhancement of photoacoustic signals from the nanocluster region so that imaging depth can be increased into the tissue.

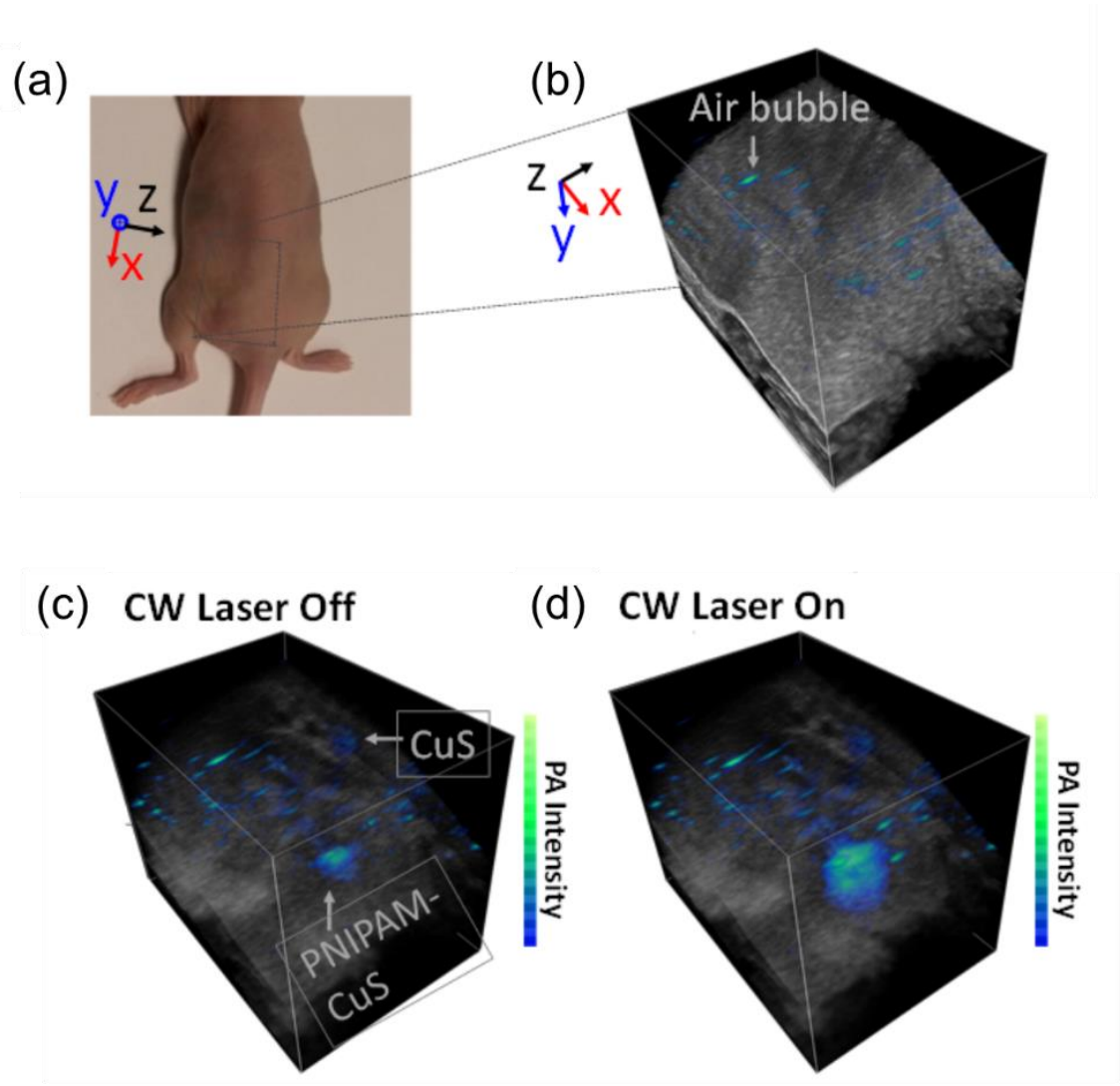

Figure 3.2: *Ex-vivo* Photoacoustic imaging of mouse. (a) A photograph a mouse model with both CuS NSs and PNIPAM-CuS injected in the region marked by the square. (b) Overlay of ultrasound and photoacoustic imaging show scattered air bubbles on the skin as a strong background noise before nanoparticle injection. (b) After nanoparticle injection, when the CW laser is off, the region with PNIPAM-CuS is clearly visualized, but the region with CuS NSs is relatively weak, and difficult to be distinguished from the bubble region. (d) When the CW laser is on, the PA intensity at the PNIPAM-CuS region is dramatically enhanced.

Besides the signal intensity enhancement that improves the imaging contrast and depth, the special signature of such dynamically changing signals can also be used to differentiate the PNIPAM-CuS nanoclusters from the background noises. Since the background noises (tissues and even bubbles) change very little when the CW laser is on and off, by subtracting PA intensities at the two states, the region with PNIMPAM-CuS nanoclusters are clearly revealed (Figure 3.4). The results show that PNIPAM-CuS nanoclusters produce dynamic contrast by CW laser irradiation. These PNIPAM-CuS nanoclusters provide several advantages over other contrast agents such as nanospheres, nanorods, and nanoshells [8-11].

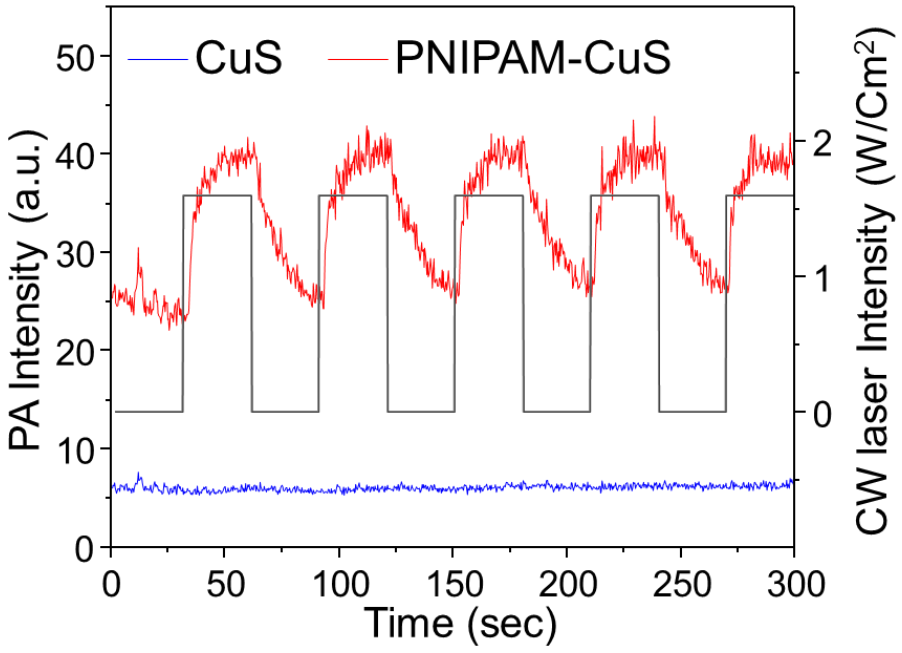

Figure 3.3: Quantitative photoacoustic signal analysis from the mouse. Multi-cycles of CW laser on and off shows the PA signals follow the CW laser on/off cycle dynamically.

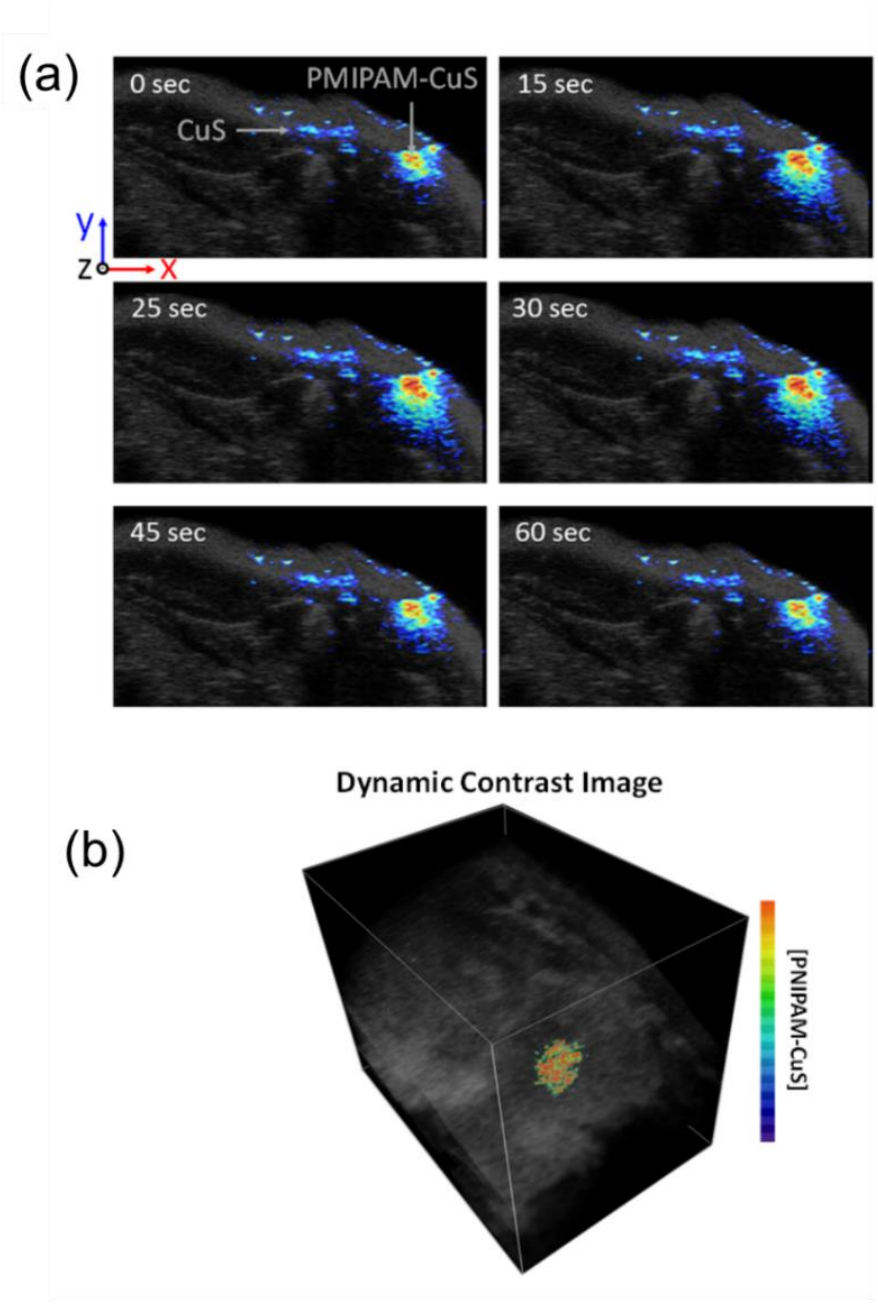

Figure 3.4: *Ex vivo* photoacoustic imaging of mouse (a) PA intensity recorded during a full cycle of CW laser on and off, (b) dynamic contrast PA image obtained by subtracting the PA intensity under CW laser-off from CW laser-on, removing the strong background noises from the tissues, CuS NPs and bubbles, and unambiguously reveals the region with only the PNIPAM-CuS.

Since the PNIPAM-CuS nanoclusters provide dynamic contrast, they can be differentiated from background in real time. By simply using CW laser, the nanoclusters can be visualized. In addition, the nanoclusters do not require spectroscopic photoacoustic analysis for detecting the presence of nanoparticles due to their dynamic contrast. This allows us to save imaging time because photoacoustic imaging is needed at only one wavelength. Furthermore, computational power for post-processing can be significantly reduced [12-14].

3.3 CONCLUSIONS

Photoacoustic generation from the developed nanoclusters highlights several interesting characteristics: First, a polymeric nanogel-nanoparticle system that generates photoacoustic signals in response to thermal stimuli was created. More importantly, hybridizing strongly optical absorbing nanoparticles also give the polymer capability to respond to light, thus dynamic volumetric changes of the polymer can be triggered by light and captured by the abrupt photoacoustic variations. The stimuli-responsive nanoclusters are built with hydrogels that have been widely used for controllable drug release. By incorporating photoacoustic imaging technique, the nonlinear photo-induced photoacoustic signal variation provides the stimuli-responsive nanoclusters capabilities for validating the drug release process. In addition, the photothermal activation of the nanocluster results in the photoacoustic contrast enhancement, serving as a photoacoustic signal nanoamplifier that potentially reduces their required dosage and toxicity. Finally, this activation can be repeatedly turned on by modulating input laser signals, suggesting a new route for photoacoustic dynamic contrast imaging that will further improve the imaging contrast to guide the drug release process more accurately.

3.4 REFERENCES

1. K. Homan, S. Kim, Y.-S. Chen, B. Wang, S. Mallidi, and S. Emelianov, "Prospects of molecular photoacoustic imaging at 1064 nm wavelength," Opt. Lett. **35**, 2663-2665 (2010).

2. L. I. o. America, *American National Standard for the Safe Use of Lasers ANSI Z136.1-2000* (American National Standards Institute, Inc., New York, 2000).

3. G. Baffou and R. Quidant, "Thermo-plasmonics: using metallic nanostructures as nano-sources of heat," Laser & Photonics Reviews **7**, 171-187 (2013).

4. X. Huang, P. K. Jain, I. H. El-Sayed, and M. A. El-Sayed, "Plasmonic photothermal therapy (PPTT) using gold nanoparticles," Lasers in Medical Science **23**, 217-228 (2008).

5. M. Bikram, A. M. Gobin, R. E. Whitmire, and J. L. West, "Temperature-sensitive hydrogels with SiO2-Au nanoshells for controlled drug delivery," Journal of Controlled Release **123**, 219-227 (2007).

6. T. L. Doane and C. Burda, "The unique role of nanoparticles in nanomedicine: imaging, drug delivery and therapy," Chemical Society Reviews **41**, 2885-2911 (2012).

7. B. P. Timko, T. Dvir, and D. S. Kohane, "Remotely triggerable drug delivery systems," Advanced Materials **22**, 4925-4943 (2010).

8. A. Agarwal, S. W. Huang, M. O'Donnell, K. C. Day, M. Day, N. Kotov, and S. Ashkenazi, "Targeted gold nanorod contrast agent for prostate cancer detection by photoacoustic imaging," Journal of Applied Physics **102**, 064701-064701-064704 (2007).

9. Y. W. Wang, X. Y. Xie, X. D. Wang, G. Ku, K. L. Gill, D. P. O'Neal, G. Stoica, and L. V. Wang, "Photoacoustic tomography of a nanoshell contrast agent in the *in vivo* rat brain," Nano Letters **4**, 1689-1692 (2004).

10. B. Wang, E. Yantsen, T. Larson, A. B. Karpiouk, S. Sethuraman, J. L. Su, K. Sokolov, and S. Y. Emelianov, "Plasmonic intravascular photoacoustic imaging for detection of macrophages in atherosclerotic plaques," Nano Letters **9**, 2212-2217 (2009).

11. V. P. Zharov, "Ultrasharp nonlinear photothermal and photoacoustic resonances and holes beyond the spectral limit," Nature Photonics **5**, 110-226 (2011).

12. S. Sethuraman, J. H. Amirian, S. H. Litovsky, R. W. Smalling, and S. Y. Emelianov, "Spectroscopic intravascular photoacoustic imaging to differentiate atherosclerotic plaques," Optics Express **16**, 3362-3367 (2008).

13. K. H. Song, C. Kim, K. Maslov, and L. V. Wang, "Noninvasive *in vivo* spectroscopic nanorod-contrast photoacoustic mapping of sentinel lymph nodes," European Journal of Radiology **70**, 227-231 (2009).

14. S. Kim, Y.-S. Chen, G. P. Luke, and S. Y. Emelianov, "*In vivo* three-dimensional spectroscopic photoacoustic imaging for monitoring nanoparticle delivery," Biomed. Opt. Express **2**, 2540-2550 (2011).

Chapter 4: Photoacoustic Imaging using Biodegradable Plasmonic Nanoclusters

In recent years, there has been growing interest in metallic plasmonic nanoparticles for various biomedical applications including imaging, sensing, and therapeutics because the nanoparticles have strong scattering and absorption in the visible and near-infrared (NIR) regions [1]. Specifically, strongly absorbing gold nanoparticles have been shown as contrast agents in photoacoustic imaging [2-5]. These nanoparticles extend penetration depth and enhance sensitivity of photoacoustic imaging *in-vivo*. Furthermore, molecular and cellular photoacoustic imaging can be achieved by using targeted gold nanoparticles [3-6] [2].

In addition to this, the photoacoustic signal enhancement from nanoclusters was demonstrated in chapter 2 and 3. It suggests that any form of nanoclusters can be a promising photoacoustic contrast agents. However, because of accumulation of nanoparticles and potential long-term toxicity, the safety of the nanoparticles in a biological environment could be a major hurdle for utilizing plasmonic nanoparticles *in-vivo* [7]. The size of commonly used nanoparticles in biomedical imaging application ranges between 20 to 150 nm – these nanoparticles may not be easily removed from the body. Previous study indicates that particles smaller than ~6 nm in diameter are rapidly cleared from the body [8]. However, the nanoparticles within this size range do not have sufficient blood residence time for imaging and therapy because they are removed too rapidly from the

[2] The results of Chapter 4.1 were published in the journal: S.J. Yoon, S. Mallidi, J.M. Tam, J.O. Tam, A. Murthy, K.P. Johnston, K.V. Sokolov, and S.Y. Emelianov, "Utility of biodegradable plasmonic nanoclusters in photoacoustic imaging," Optics Letters, 35:3751-3753 (2010). The results for Chapter 4.2 were published in the journal: S.J. Yoon, A.M. Murthy, K.P. Johnston, K.V. Sokolov, and S.Y. Emelianov, "Thermal stability of biodegradable plasmonic nanoclusters in photoacoustic imaging," Optics Express, 20(28):29479-87 (2012).

body. In addition, smaller nanoparticles produce smaller signal in comparison with larger nanoparticles [9].

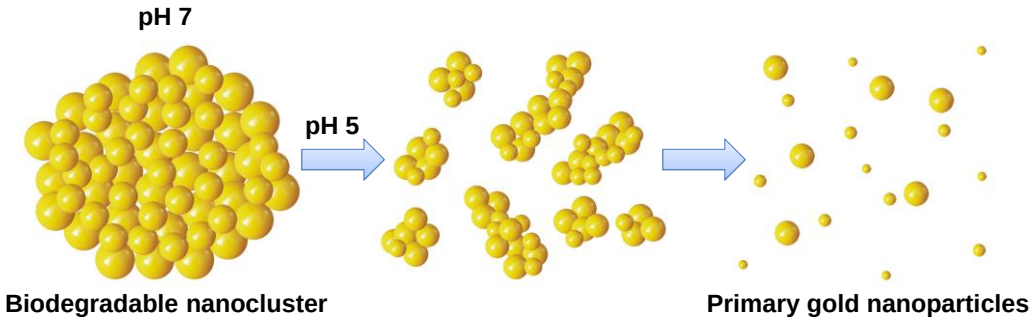

Figure 4.1: Diagram of degradation of gold nanoclusters at different pH levels.

Recently, non-toxic biodegradable plasmonic nanoclusters consisting of sub-5 nm primary gold particles stabilized by a weakly adsorbed biodegradable polymer have been reported [10, 11]. The small spacing between primary gold nanoparticles within the clusters results in strong near infra-red absorbance [12]. The nanoclusters, stable at pH 7, degrade into primary gold nanoparticles at around pH 5 (the environment inside of the endosomes) within about 7 days [10]. Once biodegraded, the 5 nm primary gold nanoparticles can be excreted from the body [13].

In this chapter, the feasibility of biodegradable nanoclusters as a photoacoustic contrast agent is demonstrated. Photoacoustic and ultrasound imaging of a tissue mimicking phantom with inclusions containing nanoclusters at various concentrations are performed. In addition, photothermal stability of different sizes of the biodegradable nanoclusters is investigated.

4.1 Quantitative Photoacoustic Imaging of Biodegradable Nanoclusters

The results of this study were published in the journal: S.J. Yoon, S. Mallidi, J.M. Tam, J.O. Tam, A. Murthy, K.P. Johnston, K.V. Sokolov, and S.Y. Emelianov, “Utility of

biodegradable plasmonic nanoclusters in photoacoustic imaging," Optics Letters, 35:3751-3753 (2010).

4.1.1 Material and Methods

The sub-100 nm clusters composed of primary 4-nm diameter gold nanoparticles were synthesized using previously published protocol [10, 11]. Briefly, 1 ml of a citrate-capped gold nanoparticle dispersion was prepared at a concentration of 3 mg/ml Au. 42 µl of a 1% (w/v) lysine solution was then added to the dispersion and stirred for 15 min, in order to create a dispersion consisting of gold nanoparticles capped with a mixture of lysine and citrate ligands. This dispersion was then diluted with deionized water to 1 mg/ml Au, and 21 mg of the biodegradable polymer PLA(1k)-PEG(10k)-PLA(1k) was added to the 1 mg/ml dispersion, resulting in a polymer/Au ratio of 7/1. The polymer-gold nanoparticle dispersion was bath sonicated for 5 min, and the resulting mixture was placed under an air stream and evaporated to a film. 2 ml of deionized water was then added to the dried film, and the mixture was bath sonicated for ~15 min, resulting in a dispersion of nanoclusters.

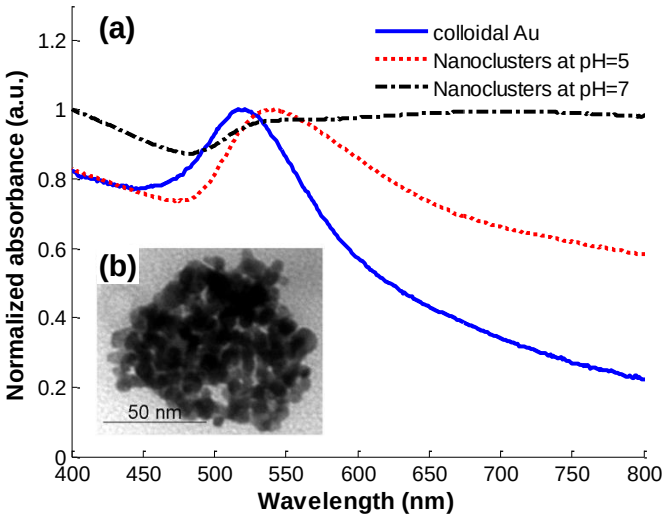

Figure 4.2: (a) Normalized absorbance spectra and (b) TEM image of biodegradable nanoclusters.

The primary colloidal gold nanospheres have an absorbance peak at 520 nm (Figure 4.2a, solid line). However, the solution of 100 nm nanoclusters (see TEM image in Figure 4.2b) at pH 7 had a broad absorbance in NIR region where soft tissue and blood have low absorption (Figure 4.2a, dashed line). In contrast, after incubation at pH 5 for 1 week, the absorbance spectrum of the nanoclusters shifted toward the original spectrum of the colloidal gold nanospheres. The difference between two spectra is due to small number (about 7%) of clusters remaining in the dispersion [10]. The result indicates that over time the biodegradable nanoclusters degrade to the primary gold nanospheres.

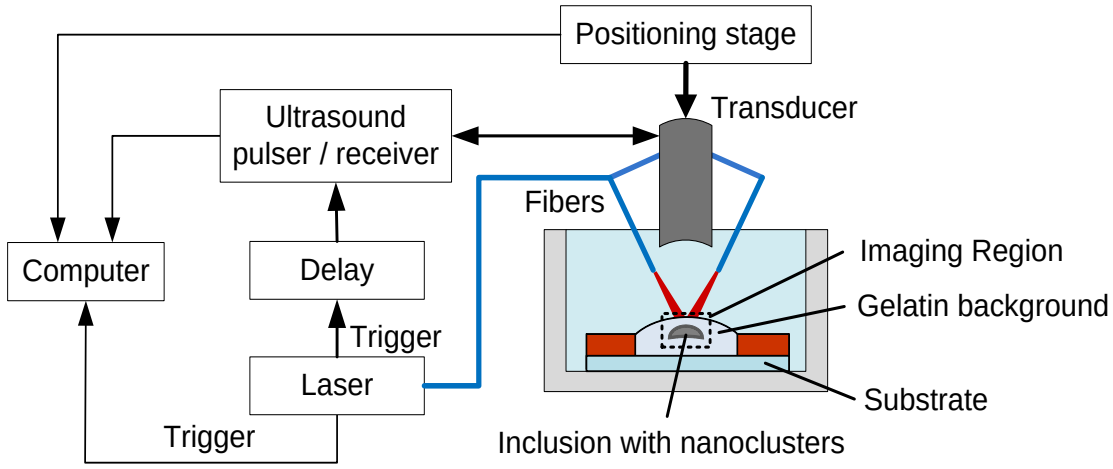

Figure 4.3: Block diagram of combined ultrasound and photoacoustic (US/PA) imaging system and the gelatin-based tissue mimicking phantom with biodegradable nanoclusters inclusion.

Photoacoustic imaging experiments were performed using tissue mimicking phantoms. To simulate the ultrasound and optical scattering properties of tissue, 8% gelatin solution with 0.1% (by weight) of 15 μm silica microparticles was poured into a mold. Once the gelatin solution was cooled, it formed a base layer of the phantom. To make an

inclusion, a single drop of aliquot of the nanocluster suspension at a given concentration mixed with gelatin and silica particles was placed at the center of the base layer. The inclusion was then cooled and covered with the 8% gelatin solution mixed with 0.1% of 15 μm silica particles (same as base layer). Four phantoms with inclusions were prepared, the concentrations of the nanoclusters in each inclusion were 550, 220, 110 and 55 μg/mL, respectively.

The combined ultrasound and photoacoustic imaging system (Figure 4.3) consisted of a pulsed OPO laser system (750 nm wavelength, 7 ns pulse duration, 10 Hz pulse repetition frequency), ultrasound transducer (25 MHz center frequency, focal depth = 12.7 mm, f# = 2), ultrasound pulser/receiver, 3D motion axis, and data acquisition unit. The phantoms were irradiated with laser pulses of four different energies: 2, 5, 10.5, and 16.5 mJ/cm^2. The laser light was delivered by optical fiber bundle consisting of 7 fibers of 600 μm in diameter. During the experiment, the tissue mimicking phantom was placed into a water cuvette. The focal point of the ultrasound transducer was positioned at the inclusion's depth and aligned with the laser beam from the optical fiber bundle. A stepper motor mechanically scanned the phantom over the imaging region with 50 μm step in lateral direction. At each step, the phantom was irradiated by the laser light and the ultrasound transducer was used to collect both photoacoustic transients and ultrasound pulse-echo signals. The recorded ultrasound and photoacoustic signals were Hilbert transformed, bandpass filtered, and spatially interpolated to form spatially co-registered 2-D cross-sectional ultrasound (US) and photoacoustic (PA) images of the phantoms.

4.1.2 Results and Discussion

The US, PA and combined US/PA images of the phantom with inclusion containing 550 μg/mL concentration of nanoclusters are presented in Figure 4.4a. Each image covers

4.7 mm by 4.4 mm field of view. The ultrasound image cannot identify the inclusion within the background – this is expected since the nanoclusters do not increase significantly the ultrasound backscattering. However, the photoacoustic image clearly differentiates the inclusion because the nanoclusters have high optical absorption compared to the background. The photoacoustic and ultrasound images can be overlaid to show the position of the inclusion within the background.

The quantitative analysis of the photoacoustic signal amplitude with respect to the different laser fluence rate measured from the regions of interest (ROI) containing the nanoclusters inclusion is shown in Figure 4.4b. A 2.33 mm × 0.67 mm ROI was selected for each photoacoustic image and divided into subareas measuring 0.33 mm × 0.33 mm. The mean and the standard deviation of the photoacoustic signal in the subareas were plotted as a function of fluence rate of laser. As the laser fluence increases, the amplitude of photoacoustic signal from the nanoclusters increases linearly (the R^2 value for the linear curve fitting is 0.9853).

The changes in the photoacoustic signal amplitude with concentration of nanoclusters are quantified in Figure 4.4c. The solid lines represent the linear fit of the photoacoustic signal measured for 5 and 10.5 mJ/cm^2 laser fluence rates with R^2 equal to 0.9895 and 0.9901, respectively. As expected, the amplitude of the photoacoustic signal from the inclusions increases with the concentration of nanoclusters. These results suggest that nanoclusters remain structurally stable under relatively large laser fluences.

The individual nanospheres have a peak absorbance at around 520 nm wavelength and, therefore, isolated spherical nanoparticles cannot be easily detected in photoacoustic imaging *in vivo* because of a spectral overlap with strong absorption of blood and tissue scattering. However, aggregation of targeted spherical nanoparticles mediated by biological molecules such as growth factor receptors or actin can lead to strong NIR

absorption; this approach has been explored for optical [12, 14, 15] and photoacoustic [3-6] molecular imaging.

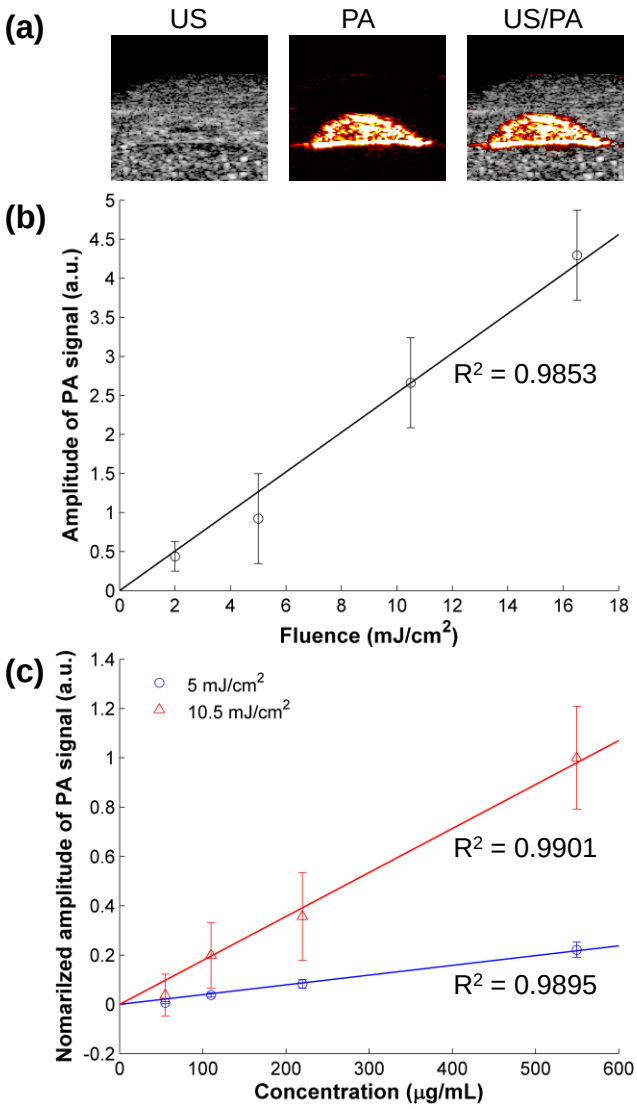

Figure 4.4: (a) Ultrasound (US), photoacoustic (PA) and combined UA/PA images of the phantom with inclusion containing nanoclusters. The concentration of the nanoclusters was 550 µg/mL. (b) Photoacoustic signal amplitude with respect to fluence rate, and (c) dependence of PA signal on nanocluster concentration at 5 and 10.5 mJ/cm^2. The solid lines represent the linear regression fit of the data.

The nanorods are also promising photoacoustic contrast agents due to their high absorption cross-section and tunability in the NIR region. However, the nanorods are not thermodynamically stable structures and change their shape and, therefore, absorption properties, at 8 mJ/cm^2 and higher laser fluence [2]. In comparison, the nanoclusters have strong NIR absorption and are expected to have reasonable thermodynamic stability thus providing an alternative contrast agent for photoacoustic imaging.

4.2 PHOTO-THERMAL STABILITY OF BIODEGRADABLE NANOCLUSTERS

During photoacoustic imaging, nanoparticles are exposed to short laser pulses with a peak laser power that is extremely high when compared to CW laser irradiation. Therefore, the thermal stability of photoacoustic contrast agents is important in producing a consistent and reliable photoacoustic signal. Previous studies have shown that gold nanorods, which are very promising photoacoustic contrast agents due to their high absorption cross-sections in the NIR region, are susceptible to melting and reshaping at the laser fluences used in photoacoustic imaging [2, 16-18].

In this study, the stability of biodegradable nanoclusters of various sizes under nanosecond laser pulses was investigated. In addition, the amplitude of the photoacoustic signal generated from nanoclusters of different sizes was analyzed and compared with the photoacoustic signal produced by the gold nanorods. Based on the thermal stability, optical absorption coefficient, and photoacoustic signal strength, the optimal nanocluster size for photoacoustic imaging and photothermal therapy is identified. This work was published in the journal: S.J. Yoon, A.M. Murthy, K.P. Johnston, K.V. Sokolov, and S.Y. Emelianov, "Thermal stability of biodegradable plasmonic nanoclusters in photoacoustic imaging," Optics Express, 20(28):29479-87 (2012).

4.2.1 Material and Methods

Synthesis of Different Sizes of Biodegradable Nanoclusters

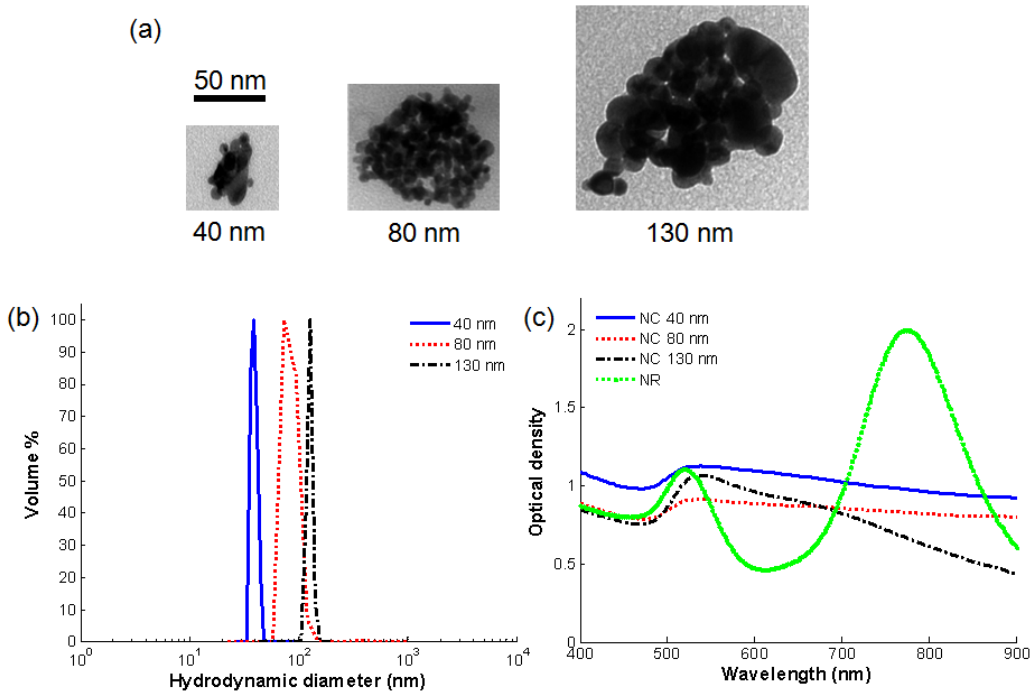

Figure 4.5: (a) Transmission electron microscopy images of 40, 80, 130 nm nanoclusters. (b) Size distribution of 40, 80, 130 nm nanoclusters measured by DLS. (c) UV-Vis-NIR spectra of 40, 80, and 130 nm nanocluster and gold nanorods suspensions at 1.2 mg/mL of gold concentration.

Biodegradable nanoclusters with controlled sizes from 40 to 130 nm were designed and synthesized by varying the ratio of polymer stabilizer to primary gold particles, the concentration of gold nanoparticles, and the surface ligands on the primary gold particles. Forty nm nanoclusters were formed as described in chapter 4.1.1. The formations of 80 nm and 130 nm nanoclusters have been described previously [11]. For 80 nm clusters, citrate/lysine capped primary nanoparticles were used with a polymer/Au ratio of 16/1, and

for 130 nm clusters, primary nanoparticles were capped by only citrate, and a polymer/Au ratio of 16/1 was used. In these cases, a 3 mg/ml Au dispersion was used before evaporation.

The shape and morphology of nanoclusters were observed by transmission electron microscopy (TEM) imaging as shown in Figure 4.5(a). The sizes of nanoclusters were further characterized by Brookhaven Instruments ZetaPlus dynamic light scattering (DLS) apparatus at a scattering angle of 90º and a temperature of 25 ºC in Figure 4.5(b). As shown in Figure 4.5(c), the UV-Vis-NIR spectra were collected from different sizes of nanocluster suspensions at 1.2 mg/mL of gold concentration in a 96-well microliter plate reader (BioTek Synergy HT). The 40 and 80 nm nanoclusters have a broad absorbance while the spectrum of 130 nm cluster shows a monotonic decrease in NIR region. In order to compare these nanoclusters with other photoacoustic contrast agent, cetyltrimethyl-ammonium (CTAB) stabilized gold nanorods were prepared by a seed-mediated growth method [19, 20].

Characterization of the Photothermal Stability of the Biodegradable Nanoclusters

To test the stability of nanoclusters exposed to a nanosecond pulsed laser irradiation, 100 μL nanocluster suspensions of three different sizes (40, 80 and 130 nm) of nanoclusters were prepared and placed in a 96-well plate. The concentration of nanoparticles in each solution was adjusted by diluting the sample with nanopure water to achieve optical density (O.D.) of ~0.6 at 780 nm for each sample. The optical density was measured at room temperature using the microplate reader. Each well was then irradiated from the top with 300 laser pulses (7 ns pulse duration, 10 Hz repetition rate, 780 nm wavelength) generated using a tunable OPO laser system (Vibrant, OPOTEK, Inc.). The fluence of the laser beam was varied from 4 to 20 mJ/cm^2. Following laser irradiation, the

O.D. of each sample was measured again, and the stability of nanoclusters under the nanosecond pulsed laser irradiation was assessed by comparison of absorbance spectra before and after the laser exposure.

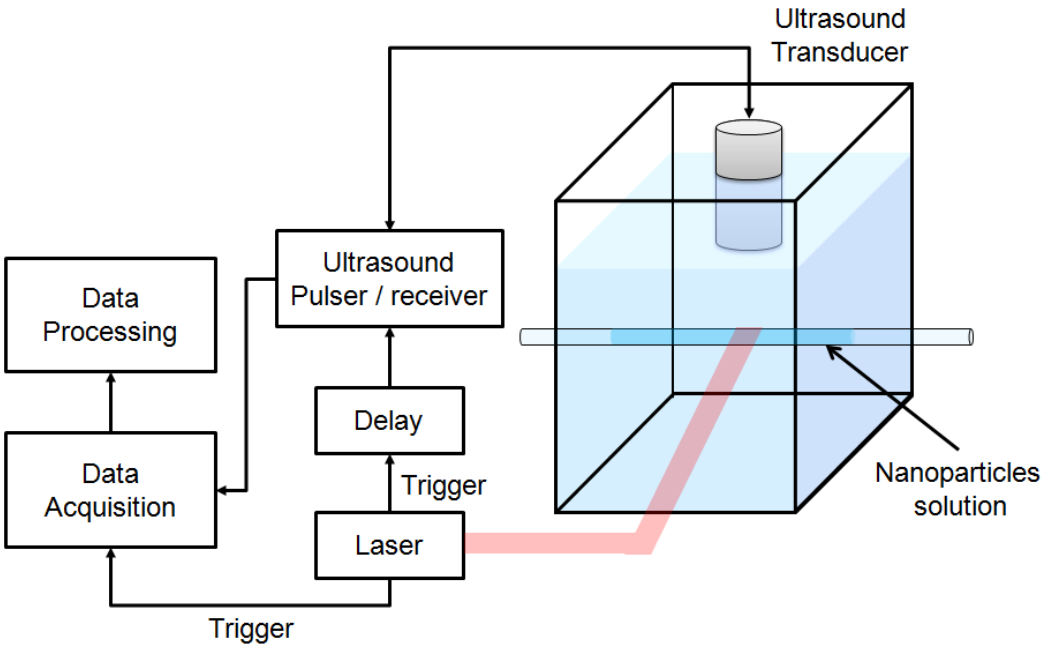

Figure 4.6: Block diagram of an experimental setup for photoacoustic signal measurement.

The stability of the photoacoustic signal was explored by measuring the photoacoustic signal intensity of 40, 80, 130 nm nanoclusters and nanorods suspensions at 1.2 mg/mL of gold concentration exposed to 200 pulses with laser fluences ranging from 4 to 20 mJ/cm^2. A custom-built system to measure the photoacoustic signal from a small sample of nanoclusters in solution is presented in Figure 4.6. The photoacoustic signals from the aqueous nanoparticle solutions were measured as a function of the number of pulses. An acrylic PMMA tube with inner diameter of 378 μm and outer diameter of 500

μm was positioned in a plastic water cuvette with an optical window for laser irradiation. Solutions of nanoclusters of different sizes but with the same overall mass of gold, measured by flame atomic absorption spectroscopy (FAAS, GBC Scientific Equipment Pty Ltd.), were injected into the tube and were kept stationary during the experiment. A 7.5 MHz single element ultrasound transducer (focal depth = 50.8 mm, aperture = 12.7 mm) was mounted on a one-dimensional translation stage and the focal point of the ultrasound transducer was located at the center of the tube containing nanocluster solution. A collimated laser beam from nanosecond pulsed laser was incident on the PMMA tube through the optical window in the water cuvette. The samples were irradiated with five different laser fluences: 4, 8, 12, 16, and 20 mJ/cm^2. For each laser pulse, the photoacoustic signal was collected by the ultrasound transducer and stored for off-line processing to determine the change of photoacoustic signal from each nanocluster solution. At each fluence, three independent measurements for each sample were performed.

Photoacoustic Imaging Setup

To investigate the importance of the thermal stability of the nanoparticles at high laser fluence in photoacoustic imaging, a tissue mimicking phantom was made of 6% polyvinyl alcohol (PVA) and 0.2% 15 μm silica by weight was constructed to simulate the ultrasound and optical properties of tissue. Four cylindrical compartments of 6 mm in diameter were created within the PVA phantom. All compartments were filled with 6 % gelatin solution containing the 40, 80, 130 nm nanoclusters and the nanorods. In each inclusion, the concentration of nanoclusters and nanorods was standardized to 0.5 mg/mL of gold.

An ultrasound and photoacoustic imaging system (Vevo 2100, Visualsonics, Inc.) with an array ultrasound transducer operating at 20 MHz center frequency was used to

obtain photoacoustic images of the tissue-mimicking phantom with embedded inclusions. At each position, the ultrasound array transducer was placed at the center of the inclusions. Nanosecond laser pulses at 780 nm were used to irradiate the samples and 4 photoacoustic signals were collected and averaged. The laser fluence was kept at 16 mJ/cm^2 which is below the safety limit set by American National Standards Institute (ANSI) of 20 mJ/cm^2 in the visible spectral region [21].

4.2.2 Results and Discussion

The thermal stabilities of the 40, 80, 130 nm nanoclusters and the nanorods were measured using a UV-Vis-NIR spectrophotometer. Figure 4.7 shows the absorbance spectra of nanoparticles before and after laser irradiation with 300 pulses at various fluencies. Changes in the absorbance spectra indicate that the laser irradiation reaches the damage threshold fluence. Laser fluence above 8 mJ/cm^2 caused visible spectral changes in the 130 nm nanocluster solution. The NIR absorbance of the 130 nm nanoclusters dramatically decreased when the fluence was increased to 20 mJ/cm^2. Nanoclusters with 40 and 80 nm sizes showed minimal spectral changes after irradiation with fluences up to 20 mJ/cm^2. Similar to 130 nm nanoclusters, gold nanorods also exhibited reduction in the NIR optical absorbance above 8 mJ/cm^2 laser fluence. Further increase in the fluence induced a strong blue shift of the longitudinal peak of optical absorbance of nanorods in the 750-800 nm range. The reduction in the absorbance of the 130 nm nanoclusters is most likely associated with degradation of the clusters to their primary particles or the smaller clusters because of the corresponding increase in the absorbance at *ca.* 520 nm; this correlation between nanocluster sizes and spectral changes was described previously [11]. In the case of nanorods, the changes in the longitudinal plasmon absorption peak between 760 and 810 nm suggest the reshaping of the nanorods [2, 16, 18]. The results indicate that

the 40 and 80 nm nanoclusters have excellent thermal stability under the nanosecond pulsed laser as compared to the larger 130 nm nanoclusters as well as gold nanorods.

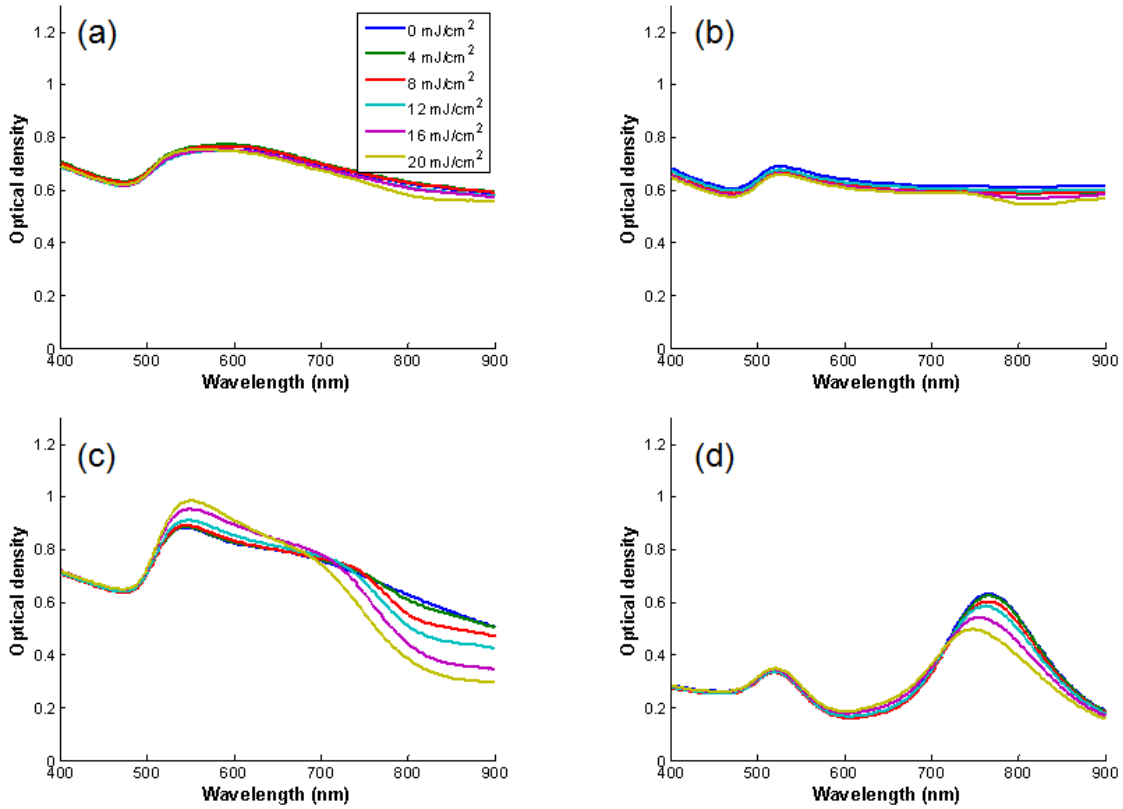

Figure 4.7: UV-Vis-NIR spectra of (a) 40 nm, (b) 80 nm, (c) 130 nm nanoclusters and (d) gold nanorods before and after laser irradiation with nanosecond laser pulses with various fluences.

The observed thermal stability of nanoclusters is closely related to their composition and binding forces between primary particles forming the clusters. The 40 and 80 nm clusters were formed using primary Au nanoparticles capped with a combination of citrate and lysine ligands and a Z-potential of -30.1 ± 2.4 mV, while the primary nanoparticles in 130 nm clusters were capped only with citrate ligand resulting in a Z-potential of -44.0 ± 4.9 mV. Based on the discernible particles in the periphery of TEM

images (see Figure 4.5a), the interparticle distances between the primary gold particles within the 40, 80, 130 nm clusters were estimated to be 1.8 ± 0.7, 1.8 ± 0.6, and 2.4 ± 1.4 nm, respectively. The larger charge repulsion between the citrate capped primary particles in 130 nm clusters leads to a more weakly assembled nanocluster and a greater particle-to-particle spacing in comparison to the 40 and 80 nm clusters. Therefore, the increased thermal stability of the 40 and 80 nm clusters can be largely attributed to the relatively small interparticle distance incurred by lower electrostatic repulsion, which results in an overall more attractive interaction between the primary nanoparticles in the clusters.

The photoacoustic signal intensity was observed as a function of number of laser pulses (Figure 4.8). While the standard deviation was measured in all experiments, for visualization purposes the error bars (plus/minus one standard deviation) are only shown in Figure 4.8d corresponding to the worst-case condition. A consistent photoacoustic signal response from contrast agents in photoacoustic imaging is important because the image analysis is based on the assumption that the photoabsorbers remain the same in terms of the concentration and absorbance during the imaging. The photoacoustic signal was stable for all nanoparticles at 4 mJ/cm^2, which is below damage threshold measured by UV-Vis-NIR spectroscopy (see Figure 4.7). The 40 and 80 nm nanoclusters produced similar photoacoustic signals, while the 130 nm nanoclusters only generated a very small photoacoustic signal which is just above the background signal measured from the sample without nanoparticles. The photoacoustic signals from the 40 and 80 nm nanocluster solutions were stable up to 12 mJ/cm^2; however, a decay in the signal was observed for both nanoclusters exposed to fluences above 12 mJ/cm^2. At 20 mJ/cm^2, the 40 nm nanoclusters produced the highest photoacoustic signal among all the samples, which was 3.8 times higher than the signal from the nanorod solution. The photoacoustic signal from

40 nm nanoclusters increased 4.5 times when the laser fluence was raised from 4 to 20 mJ/cm^2.

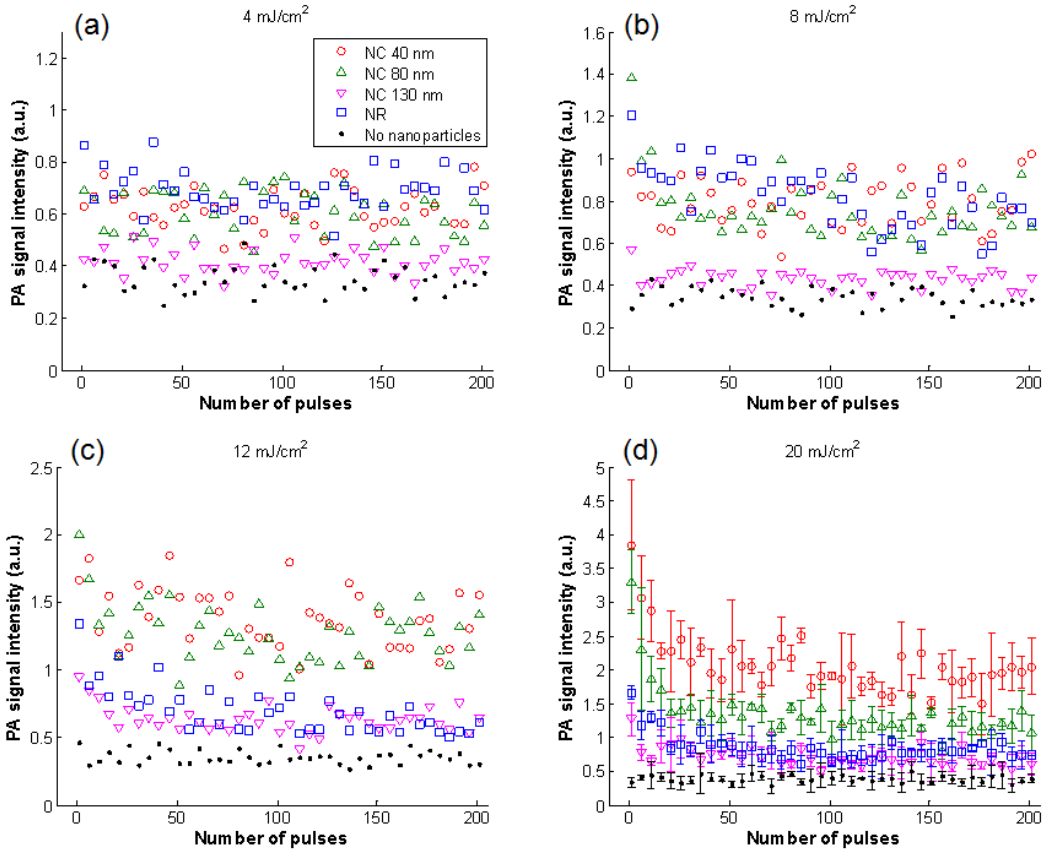

Figure 4.8: Photoacoustic signal intensity of the 40, 80, 130 nm nanoclusters and the nanorods as a function of number of pulses with fluence (a) 4 mJ/cm^2, (b) 8 mJ/cm^2, (c) 12 mJ/cm^2, and (d) 20 mJ/cm^2.

In general, the photoacoustic signal generated by photoabsorbers is linearly increases with the laser fluence. However, the photoacoustic signal from the 40 nm nanoclusters only increased 4.5 times while the fluence was increased 5 times. This can be attributed to photothermal damage of the nanoclusters which is shown as a small reduction in the absorbance at 20 mJ/cm^2 (Figure 4.8a). Using the same conditions, the photoacoustic

signal increase for the nanorods was only 1.1 times. This can be associated with melting and reshaping of the nanorods when exposed to elevated laser fluences. At equivalent gold mass concentrations, the measurements indicate that the 40 nm nanoclusters can produce a photoacoustic signal that is higher than the nanorods when the fluence is higher than 12 mJ/cm^2 because of their superior photothermal stability and photoacoustic signal enhancement due to clustering.

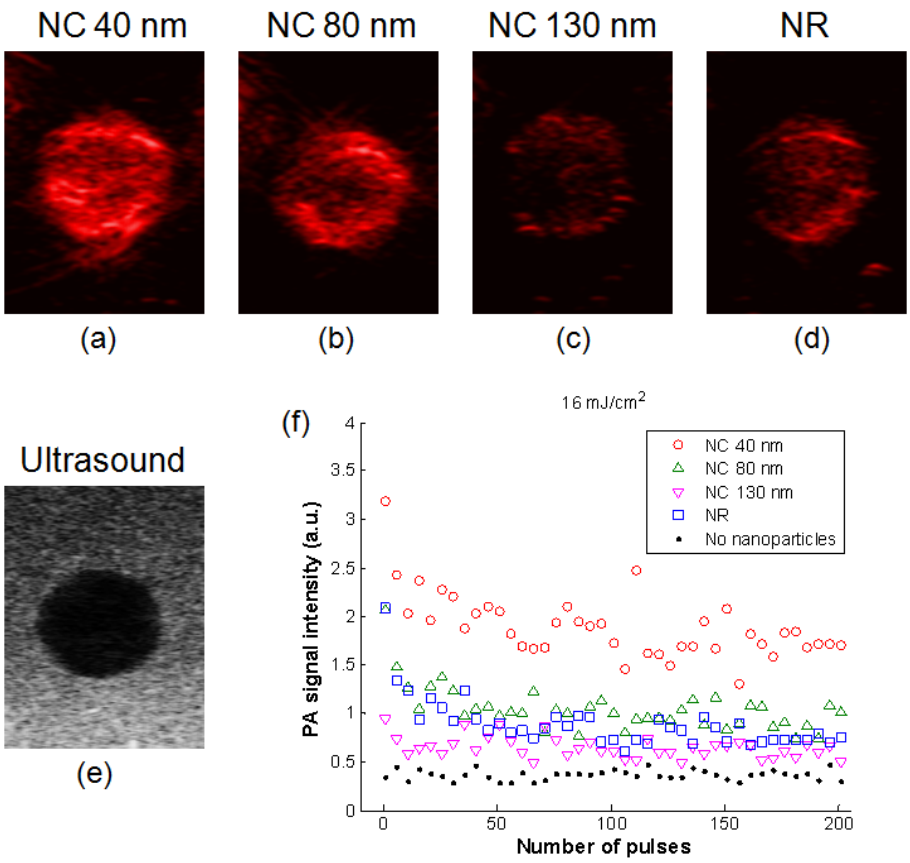

Figure 4.8: Photoacoustic images of the phantom with inclusions containing the (a) 40, (b) 80, (c) 130 nanoclusters, and (d) nanorods. (e) An ultrasound image of the hypoechoic inclusion with hyperechoic background. The photoacoustic images were acquired using 16 mJ/cm^2 laser fluence. (f) Photoacoustic signal intensity of the 40, 80, 130 nm nanoclusters and the nanorods with respect to number of pulses at fluence 16 mJ/cm^2.

Using a tissue-mimicking phantom, the importance of the stability of nanoparticles in photoacoustic imaging was demonstrated. The photoacoustic images of the phantom with inclusions were obtained at 16 mJ/cm^2 laser fluence and 780 nm wavelength corresponding to the peak optical absorption wavelength of the nanorods. More than 50 pulses were used to irradiate each phantom before the photoacoustic images were collected. Inclusion with 130 nm nanoclusters produced the weakest photoacoustic signal among the samples (Figure 4.9). The photoacoustic signal from 40 nm nanoclusters showed the brightest signal at this laser fluence (Figure 4.9a). Interestingly, both the 40 and the 80 nm nanoclusters exhibited stronger photoacoustic signal than that of nanorods. These results are in good agreement with the results presented in Figure 4.8 where stability of nanoparticles was measured at 16 mJ/cm^2 laser fluence using the system described in Figure 4.6.

In general, the photoacoustic signal intensity is proportional to the optical absorption coefficient of the sample. The absorbance of the 40 nm nanocluster solution measured by UV-Vis-NIR spectrometry at 780 nm (λ_{max} of gold nanorods) was only half of that of the nanorod solution at the same amount of gold (Figure 4.5c). However, both nanoparticles produce similar levels of photoacoustic signal at 4 mJ/cm^2, which is below the damage threshold for both types of nanoparticles as demonstrated in Figure 4.8a. The result clearly indicates that nanoclusters provide an enhanced photoacoustic signal. Several mechanisms including optical, thermal [22], and acoustic coupling effects can contribute to the enhancement of the photoacoustic signal from closely spaced primary nanoparticles. Indeed, a photoacoustic signal enhancement effect and a non-linearity with fluence have recently been reported for other forms of clusters [23, 24]. Reasons for this effect could be local change in the temperature distribution and thermal conductivity. It has been reported that the effective thermal conductivity can be significantly enhanced due to the thermal

transport along nanoparticles chains [25]. Others found that the thermal conductivity of gold spheres with a polymer shell is higher than predicted, based on the bulk properties with the addition of an organic co-solvent to the aqueous medium [26], and it was demonstrated that the increased thermal interfacial conductivity enhances the photoacoustic signal [17, 27]. Therefore, the enhancement of photoacoustic signal in biodegradable plasmonic nanoclusters may be attributed to the laser induced thermal coupling, transport effects in clusters, and/or an increased thermal transfer through gold interface induced by the clustering and the biodegradable polymer stabilizer.

4.3 BIODISTRIBUTION STUDY OF BIODEGRADABLE NANOCLUSTERS

The advance in molecular imaging offers the development of sensitive diagnostics and tumor-targeted therapeutics. For many years, there has been tremendous interest in developing contrast agents such as gold nanoparticles and nanoparticles can be used for the selective delivery of drugs to specific targets [28]. Despite the advance in nanoparticle research such as synthesis, characterization, and identification, these advantages can only be achieved when *in vivo* profile of these nanoparticles is fully investigated [29]. Different administration routes may cause varying effects on the biodistribution of the nanoparticles. In addition, the *in vivo* biodistribution of the nanoparticles largely depends on their shape, size, and chemistry such as surface charge and hydrophobicity [30, 31]. In this section, biodegradable nanoclusters are intravenously administrated in mice and the biodistribution of the nanoparticles is monitored by photoacoustic imaging.

4.3.1. Material and Methods

Animal Preparation

For *ex vivo* mouse imaging, 2-4 months old Balb/c female mice were used for this clearance study. All animal studies performed for this chapter were approved under

Institutional Animal Care and Use Committee (IACUC) protocol AUP-2012-00020. Mice were categorized into three groups: solid gold nanosphere-injected, biodegradable nanocluster-injected, and PBS-injected mice. Mice were monitored up to 2 months with the time points of sacrifice at 1 day, 1 week, 1 month, and 2 months. At each time point, photoacoustic imaging was performed after the sacrifice.

Spectroscopic Photoacoustic Imaging Setup

VEVO 2100 ultrasound and photoacoustic imaging system (VisualSonics, Inc.) was used with a 20 MHz array transducer (VisualSonics, Inc.) as described in chapter 3. To differentiate nanoparticles from the background tissue, multi-wavelength photoacoustic imaging was performed with fluence of 5-15 mJ/cm^2. In this experiment, 9 wavelengths from 730 to 890 nm with an increment of 20 nm (i.e., 730, 750, 770, 790, 810, 830, 850, 870, and 890 nm) were used to obtain photoacoustic images. Spectroscopic photoacoustic imaging allows us to differentiate main optical absorbers in tissue, which are oxygenated and deoxygenated blood and nanoparticles in this case. At each cross-section, the pulse-to-pulse laser energy was recorded and compensated for laser energy fluctuation. The photoacoustic signals collected from different wavelengths at each cross-section were compared to the absorption spectra of oxygenated and deoxygenated hemoglobin and nanoparticles. To obtain the correlation coefficients of the absorbers, both linear least squares (LLS) and minimum mean square error (MMSE) methods were used [32].

4.3.2. Results and Discussion

To monitor the biodistribution of nanoparticles, *ex vivo* photoacoustic imaging of nanoparticle injected mice was performed. Mice were injected via tail vein with 200 μL of 6 mg/mL of either 40 nm biodegradable nanoclusters or 10 kD PEGylated 40 nm gold nanospheres in phenol-free DMEM media. For a control group, PBS was injected into

mice. After sacrifice of the mice, the hair was shaved before imaging to remove any photoacoustic signal from the hair. Liver and spleen (hypoechoic area in Figure 4.10b-c) can be differentiated from other tissue using the anatomical information provided by ultrasound images.

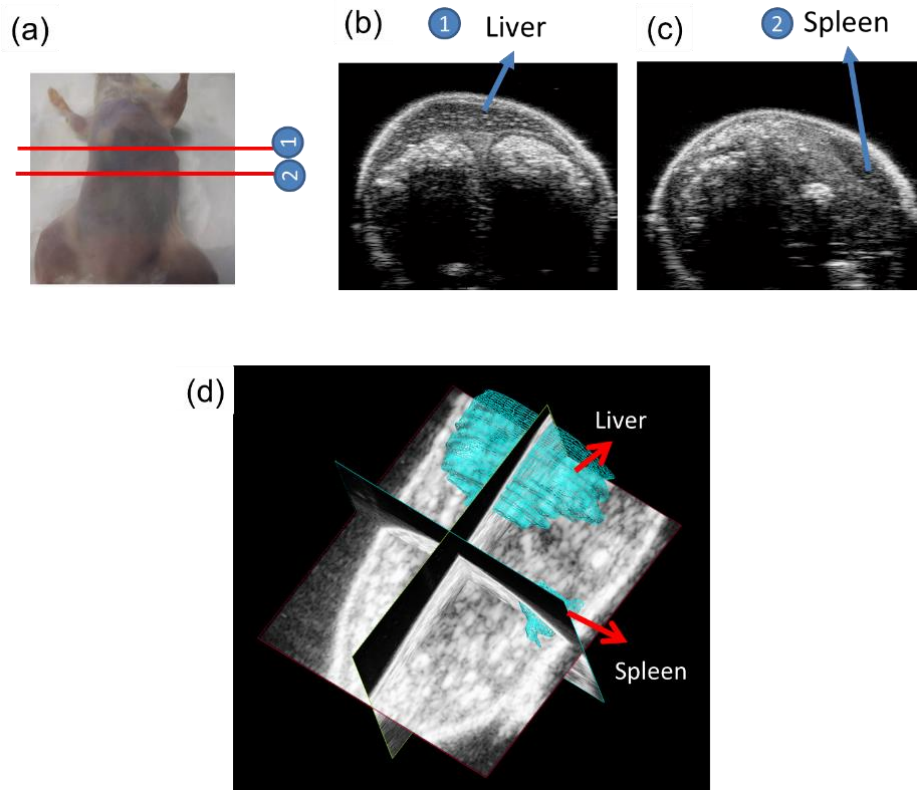

Figure 4.10: (a) Photograph of a Balb/c mouse. (b) Ultrasound image of liver and (c) spleen. (d) 3D ultrasound image of the mouse.

Figure 4. 11 shows spectroscopic images of nanoparticles obtained by spectroscopic photoacoustic imaging of the mice. For the nanocluster injected mouse at 1 day, the accumulation of nanoclusters in a liver and a spleen were clearly observed, while no nanoparticles were detected in PBS injected mice. The influence on the uptake of particles by the mononuclear phagocyte system comprising mainly by the macrophages of the liver and spleen after intravenous injection has been discussed in detail elsewhere [33].

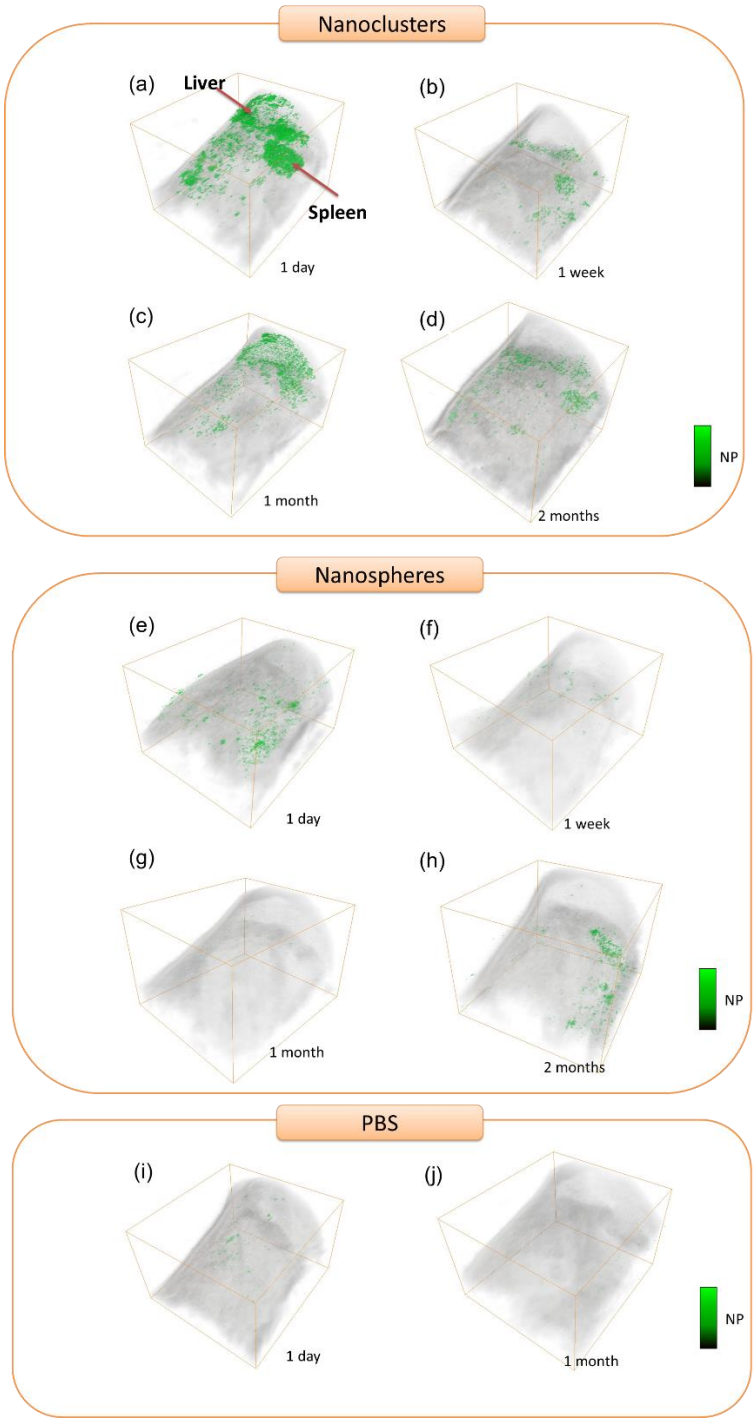

Figure 4.11: Spectroscopic photoacoustic images of nanoparticle. Nanoparticle maps for (a-d) biodegradable nanocluster, (e-h) gold nanospheres, (f-j) PBS injected mice at the time points of 1 day, 1 week, 1 month, and 2 months.

The photoacoustic signal from nanoclusters dropped at the time point of 1 week and kept similar level until the time point of 2 months. There are two possible reasons for the signal decrease from the nanoparticles. First, the biodegradable nanoclusters can be degraded. However, it does not necessarily mean the clearance of the nanoparticles. Once biodegradable nanoclusters degrade, they no longer have broad spectrum in NIR region due to the lack of plasmonic coupling between the individual nanoparticles. Similarly, gold nanospheres were not detected properly (Figure 4.11e-h) by the current spectroscopic photoacoustic imaging setting because gold nanospheres have an absorption peak around 520 nm but the imaging were performed in the optical window, the wavelength of 730 to 870 nm. The other possibility of the signal decrease is that only one mouse was imaged at the each time point, therefore, the more number of samples are required to conclude the reason of dropping the signal.

4.4 *IN VIVO* PHOTOACOUSTIC IMAGING OF MICE WITH TUMORS

Molecular imaging techniques can provide anatomic and functional details of cells and tissue which is critical for cancer diagnostics and research. It has a great potential for the early stage of tumor detection and effective treatment of diseases. In general, molecular imaging relies on external probes that have a high affinity to the specific molecules. There has been considerable interest in epidermal growth receptor (EGFR) because of their signaling pathway in oncology and maintenance of different types of tumors. One of the promising approaches using monoclonal antibodies against EFGR (anti-EGFR) is tested in this section [14]. *In vitro and in vivo* photoacoustic imaging is performed by utilizing anti-EGFR antibody conjugated biodegradable nanoclusters.

4.4.1. Material and Methods

Tissue Mimicking Phantom Preparation

Gelatin based tissue-mimicking phantom with cell inclusion were prepared for photoacoustic imaging. To mimic tissue properties, 6 % gelatin solution with 0.1 wt% of 15 μm silica particles was prepared for base and top layers which encapsulated cell inclusions. The concentrations of cells are 1×10^6 cells/mL for the all inclusions. Molecular specificity of the antibody-conjugated nanoparticles was evaluated in two cell line: EGFR-positive A431 and EGFR-negative MDA-MB-435 cells. Biodegradable nanoclusters were conjugated with anti-EGFR clone 225 antibodies. 5 kD PEGylated biodegradable nanoclusters were used as control. Specifically, the inclusions of A431 cells labeled with anti-EGFR biodegradable nanoclusters, A431 cells with PEGylated biodegradable nanoclusters, MDA-MB-435 cells with anti-EGFR biodegradable nanoclusters and MDA-MB-435 cells with PEGylated biodegradable nanoclusters were prepared.

Animal Preparation

EGFR expressing human A431 cells and EGFR-negative human MDA-MB-435 cells were incubated in phenol-free DMEM (Invitrogen, 11039) and MEM (Invitrogen, 41061) culture media, respectively, supplemented with 10% fetal bovine serum (FBS) at 37˚C in a 5% CO_2 environment. Mice were subcutaneously inoculated with both MDA-MB-435 cells and A431 cells on the same side of the mice and the tumors were allowed to grow to about 6 mm in diameter. The mice were then imaged before the injection of either anti-EGFR biodegradable nanoclusters or PEGylated biodegradable nanoclusters. Photoacoustic imaging was performed at 24 hours post-injection using VEVO LAZR system.

Ultrasound and Spectroscopic Photoacoustic Imaging Setup

VEVO LAZR ultrasound and photoacoustic imaging system (VisualSonics, Inc.) was used with a 20 MHz array transducer (VisualSonics, Inc.) as described previously. To differentiate nanoparticles from the background tissue, spectroscopic photoacoustic imaging was perform at 8 different wavelengths (i.e., 740, 750, 760, 800, 840, 880, 920, and 960 nm) with fluence of 5-15 mJ/cm^2 satisfying an American National Standard Institute (ANSI) limit [21]. During the imaging, electrocardiography (ECG) signal was monitored and respiration gating was applied to minimize a motion artifact.

4.4.2. Results and Discussion

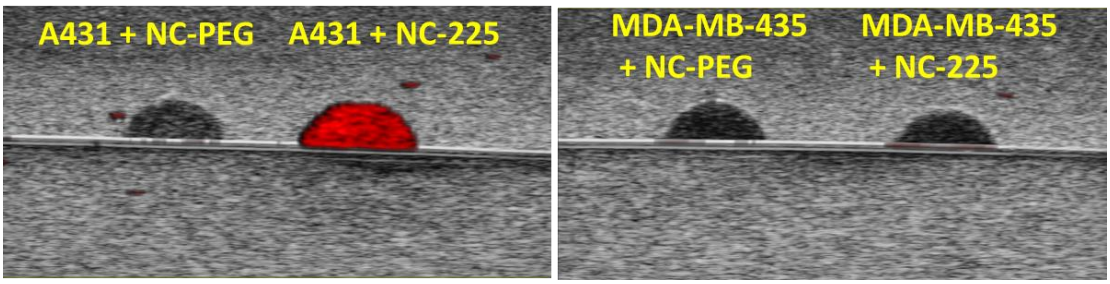

Figure 4.12: Photoacoustic images of tissue mimicking phantom. The inclusions include A431 cells with PEGylated biodegradable nanocluster, A431 cells with nanoclusters conjugated with anti-EGFR clone 225 antibodies, MDA-MB-435 cells with PEGylated biodegradable nanocluster, and MDA-MB-435 cells with anti-EGFR clone 225 antibodies, respectively.

The US, PA and combined US/PA images of the phantom with inclusions, A431 cells with PEGylated biodegradable nanocluster, A431 cells with nanoclusters conjugated with anti-EGFR clone 225 antibodies, MDA-MB-435 cells with PEGylated biodegradable nanocluster, and MDA-MB-435 cells with anti-EGFR clone 225 antibodies, respectively, are presented in Figure 4.12. Each image covers 20 mm × 10 mm field of view. The laser fluence was 13 mJ/cm^2 and the images were collected at the wavelength of 700 nm. The photoacoustic image of inclusion of A431 cells with anti-EGFR nanoclusters shows strong

photoacoustic signal while the rest of the inclusions do not provide any photoacoustic signal. The results confirmed that biodegradable nanoclusters were successfully conjugated with anti-EGFR clone 225 antibodies.

Spectroscopic photoacoustic imaging was performed on tumor-bearing mice. Each mouse has 2 kinds of the tumor (MDA-MB-435 EGFR(-) and A431 EGFR(+)) on the same side of the mouse. Mice were divided into two groups: anti-EGFR biodegradable nanoclusters and PEGylated biodegradable nanoclusters injected mice.

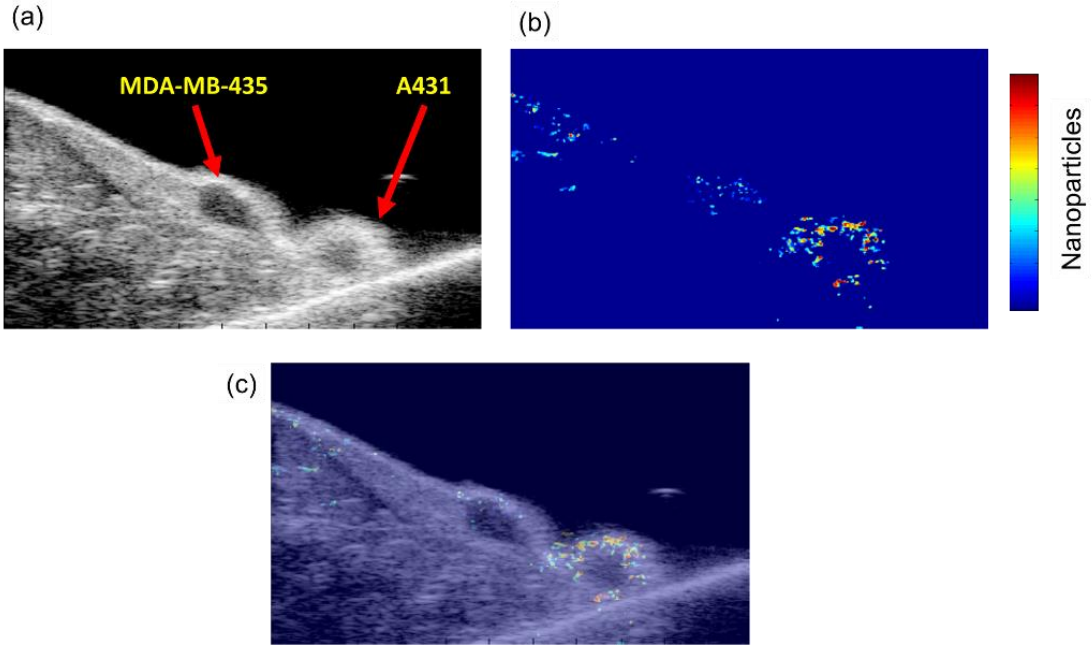

Figure 4.13: (a) Ultrasound image of MDA-MB-435 and A431 tumor-bearing mouse. (b) Spectroscopic photoacoustic image of nanoclusters calculated by spectroscopic photoacoustic imaging. (c) Combined US and spectroscopic photoacoustic image of nanoclusters.

Figure 4.13a shows the ultrasound image of the mouse with MDA-MB-435 (left) and A431 tumors (right). The spectroscopic images have been spectrally unmixed from a set of 8 wavelengths from 740 to 960 nm after the injection of biodegradable nanoclusters

conjugated with anti-EGFR clone 225 antibodies. Both linear least squares (LLS) and minimum mean square error (MMSE) were used to identify nanoclusters (Figure 4.13b). The spectroscopic image shows more accumulation of nanoclusters in the region of the A431 tumor compared to that of MDA-MB-435 tumor, indicating that biodegradable nanoclusters conjugated with anti-EGFR clone 225 antibodies have higher affinity to the A431 tumor.

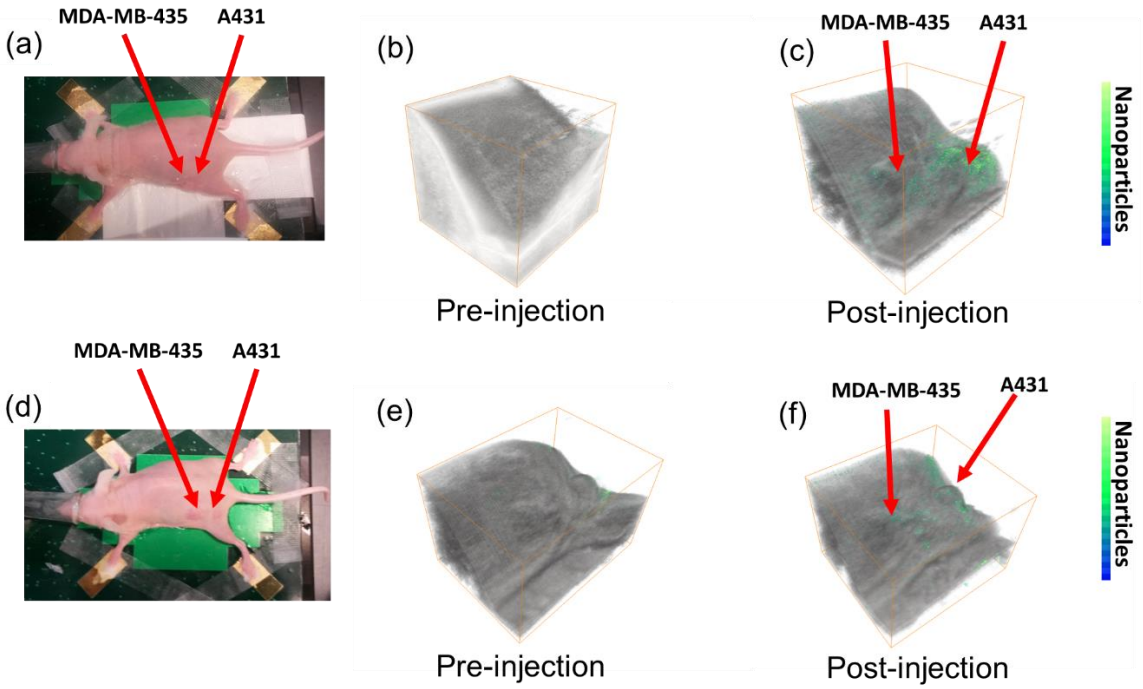

Figure 4.14: (a) A photograph of mouse #1 (b) Spectroscopic photoacoustic image of nanoclusters before injection and (c) after injection of anti-EGFR biodegradable nanoclusters. (d) A photograph of mouse #2 (e) Spectroscopic photoacoustic image of nanoclusters before injection and (f) after injection of anti-EGFR biodegradable nanoclusters.

Figure 4.14 shows the 3D spectroscopic photoacoustic images of biodegradable nanoclusters with anti-EGFR 225 antibodies injected mice. Two mice were imaged for the

each group. The photographs show the location of two kinds of tumors (Figure 4.14). The post-injection spectroscopic photoacoustic image of nanoclusters from mouse #1 shows the accumulation of the biodegradable nanoclusters conjugated with anti-EGFR clone 225 antibodies in A431 tumor. The similar results were obtained from mouse #2.

Figure 4.15 represents the 3D spectroscopic photoacoustic images of biodegradable PEGylated nanoclusters injected mice. Unlike the spectroscopic photoacoustic images from the nanoclusters conjugated with anti-EGFR 225 antibodies, the accumulation of the biodegradable nanoclusters in a specific tumor was not observed from 2 mice in this group.

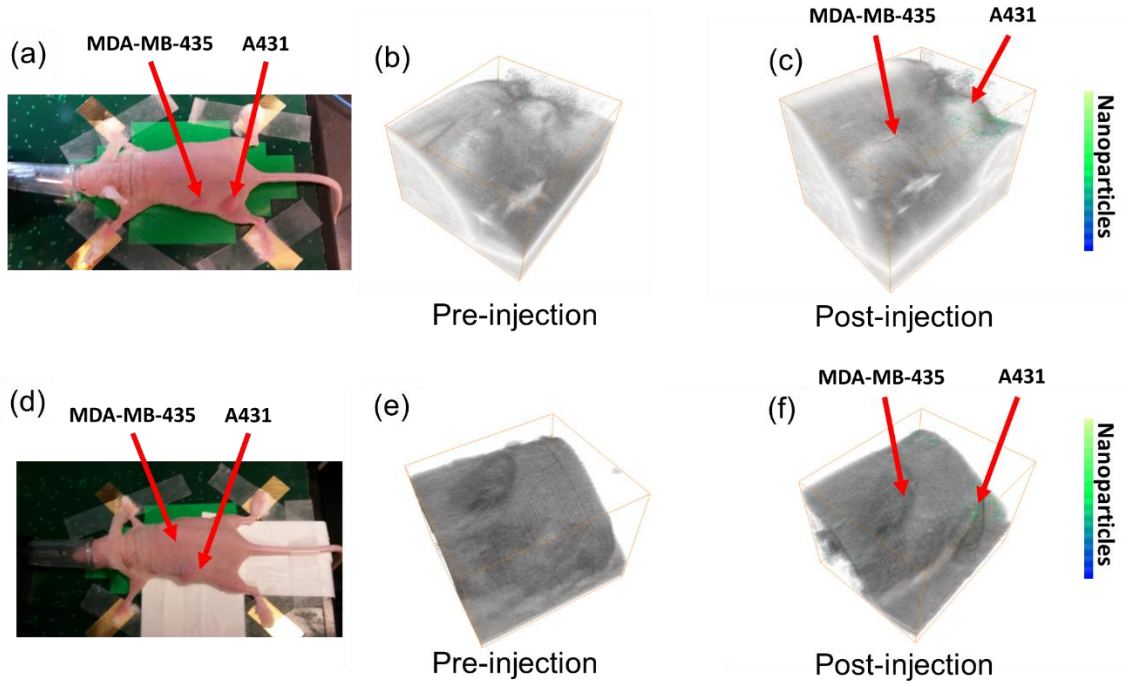

Figure 4.15: (a) A photograph of mouse #3 (b) Spectroscopic photoacoustic image of nanoclusters before injection and (c) after injection of PEGylated biodegradable nanoclusters. (d) A photograph of mouse #4 (e) Spectroscopic photoacoustic image of nanoclusters before injection and (f) after injection of PEGylated biodegradable nanoclusters.

4.5 CONCLUSIONS

In conclusion, the usability of biodegradable nanoclusters (consisting of small primary gold nanospheres and a polymeric stabilizer) as a photoacoustic imaging contrast agent was explored. It was demonstrated that an inclusion with biodegradable nanoclusters, characterized by enhanced absorption within broad NIR spectrum due to plasmon resonance coupling between closely spaced primary nanoparticles [10], can be imaged in an optically scattering tissue mimicking environment using NIR photoacoustic imaging. It is demonstrated that the photoacoustic signal intensity is linearly proportional to the laser fluence and concentration of the nanoclusters suggesting their structural and thermodynamic stability. The stability of biodegradable plasmonic nanoclusters of three different sizes was also investigated in an aqueous solution under nanosecond laser pulses. Photoacoustic signals from the nanoparticles at various fluences were also studied and compared with that of gold nanorods. The photoacoustic signal amplification from clustering of primary gold nanoparticles was observed. The results indicate that 40 nm nanoclusters have superior photo-thermal stability for photoacoustic imaging and produce stronger photoacoustic signal as compared to nanorods at a given concentration of gold. The biodistribution of biodegradable nanoclusters was explored using spectroscopic photoacoustic imaging technique. The accumulation of nanoclusters in the liver and spleen was observed. Finally, antibody conjugated biodegradable nanoclusters were injected into tumor-bearing mice and imaged. The location of antibody conjugated biodegradable nanoclusters was presented by the spectroscopic photoacoustic images. In addition, higher affinity to the A431 tumor was demonstrated from the biodegradable nanoclusters conjugated with anti-EGFR clone 225 antibodies. Overall, the results of the study suggest that the biodegradable plasmonic nanoclusters are promising contrast agents for molecular photoacoustic imaging and other biomedical applications such as photothermal therapy.

4.6 REFERENCES

1. P. Alivisatos, "The use of nanocrystals in biological detection," Nature Biotechnology **22**, 47-52 (2004).

2. Y.-S. Chen, W. Frey, S. Kim, K. Homan, P. Kruizinga, K. Sokolov, and S. Emelianov, "Enhanced thermal stability of silica-coated gold nanorods for photoacoustic imaging and image-guided therapy," Opt. Express **18**, 8867-8878 (2010).

3. K. Homan, S. Kim, Y.-S. Chen, B. Wang, S. Mallidi, and S. Emelianov, "Prospects of molecular photoacoustic imaging at 1064 nm wavelength," Opt. Lett. **35**, 2663-2665 (2010).

4. S. Mallidi, T. Larson, J. Aaron, K. Sokolov, and S. Emelianov, "Molecular specific optoacoustic imaging with plasmonic nanoparticles," Optics Express **15**, 6583-6588 (2007).

5. B. Wang, E. Yantsen, T. Larson, A. B. Karpiouk, S. Sethuraman, J. L. Su, K. Sokolov, and S. Y. Emelianov, "Plasmonic Intravascular Photoacoustic Imaging for Detection of Macrophages in Atherosclerotic Plaques," Nano Lett. **9**, 2212-2217 (2008).

6. S. Mallidi, T. Larson, J. Tam, P. P. Joshi, A. Karpiouk, K. Sokolov, and S. Emelianov, "Multiwavelength Photoacoustic Imaging and Plasmon Resonance Coupling of Gold Nanoparticles for Selective Detection of Cancer," Nano Letters **9**, 2825-2831 (2009).

7. N. Lewinski, V. Colvin, and R. Drezek, "Cytotoxicity of nanoparticles," Small **4**, 26-49 (2008).

8. H. S. Choi, W. Liu, P. Misra, E. Tanaka, J. P. Zimmer, B. I. Ipe, M. G. Bawendi, and J. V. Frangioni, "Renal clearance of quantum dots," Nature Biotechnology **25**, 1165-1170 (2007).

9. P. K. Jain, K. S. Lee, I. H. El-Sayed, and M. A. El-Sayed, "Calculated absorption and scattering properties of gold nanoparticles of different size, shape, and composition: Applications in biological imaging and biomedicine," Journal of Physical Chemistry B **110**, 7238-7248 (2006).

10. J. M. Tam, J. O. Tam, A. Murthy, D. R. Ingram, L. L. Ma, K. Travis, K. P. Johnston, and K. V. Sokolov, "Controlled assembly of biodegradable plasmonic nanoclusters for near-infrared Imaging and therapeutic applications," ACS nano **4**, 2178-2184 (2010).

11. J. M. Tam, A. K. Murthy, D. R. Ingram, R. Nguyen, K. V. Sokolov, and K. P. Johnston, "Kinetic assembly of Near-IR-Active gold nanoclusters using weakly adsorbing polymers to control the size," Langmuir **26**, 8988-8999 (2010).

12. J. Aaron, K. Travis, N. Harrison, and K. Sokolov, "Dynamic imaging of molecular assemblies in live cells based on nanoparticle plasmon resonance coupling," Nano Letters **9**, 3612-3618 (2009).

13. J. K. Vasir and V. Labhasetwar, "Biodegradable nanoparticles for cytosolic delivery of therapeutics," Advanced Drug Delivery Reviews **59**, 718-728 (2007).

14. K. Sokolov, M. Follen, J. Aaron, I. Pavlova, A. Malpica, R. Lotan, and R. Richards-Kortum, "Real-time vital optical imaging of precancer using anti-epidermal growth factor receptor antibodies conjugated to gold nanoparticles," Cancer Research **63**, 1999-2004 (2003).

15. J. Aaron, N. Nitin, K. Travis, S. Kumar, T. Collier, S. Y. Park, M. Jose-Yacaman, L. Coghlan, M. Follen, R. Richards-Kortum, and K. Sokolov, "Plasmon resonance coupling of metal nanoparticles for molecular imaging of carcinogenesis *in vivo*," Journal of Biomedical Optics **12**(2007).

16. Y. T. Wang, S. Teitel, and C. Dellago, "Surface-driven bulk reorganization of gold nanorods," Nano Letters **5**, 2174-2178 (2005).

17. Y. S. Chen, W. Frey, S. Kim, P. Kruizinga, K. Homan, and S. Emelianov, "Silica-coated gold nanorods as photoacoustic signal nanoamplifiers," Nano Lett **11**, 348-354 (2011).

18. L.-C. Chen, C.-W. Wei, J. S. Souris, S.-H. Cheng, C.-T. Chen, C.-S. Yang, P.-C. Li, and L.-W. Lo, "Enhanced photoacoustic stability of gold nanorods by silica matrix confinement," Journal of Biomedical Optics **15**, 016010 (2010).

19. N. R. Jana, L. Gearheart, and C. J. Murphy, "Seed-mediated growth approach for shape-controlled synthesis of spheroidal and rod-like gold nanoparticles using a surfactant template," Advanced Materials **13**, 1389-1393 (2001).

20. B. Nikoobakht and M. A. El-Sayed, "Preparation and growth mechanism of gold nanorods (NRs) using seed-mediated growth method," Chemistry of Materials **15**, 1957-1962 (2003).

21. L. I. o. America, *American National Standard for the Safe Use of Lasers ANSI Z136.1-2000* (American National Standards Institute, Inc., New York, 2000).

22. A. Sanchot, G. Baffou, R. Marty, A. Arbouet, R. Quidant, C. Girard, and E. Dujardin, "Plasmonic nanoparticle networks for light and heat concentration," ACS Nano **6**, 3434-3440 (2012).

23. S. Y. Nam, L. M. Ricles, L. J. Suggs, and S. Y. Emelianov, "Nonlinear photoacoustic signal increase from endocytosis of gold nanoparticles," Optics Letters **37**, 4708-4710 (2012).

24. C. L. Bayer, S. Y. Nam, Y.-S. Chen, and S. Y. Emelianov, "Photoacoustic signal amplification through plasmonic nanoparticle aggregation," J Biomed Opt, submitted (2012).

25. W. Evans, R. Prasher, J. Fish, P. Meakin, P. Phelan, and P. Keblinski, "Effect of aggregation and interfacial thermal resistance on thermal conductivity of nanocomposites and colloidal nanofluids," International Journal of Heat and Mass Transfer **51**, 1431-1438 (2008).

26. Z. Ge, Y. Kang, T. A. Taton, P. V. Braun, and D. G. Cahill, "Thermal transport in Au-core polymer-shell nanoparticles," Nano Letters **5**, 531-535 (2005).

27. Y.-S. Chen, W. Frey, S. Aglyamov, and S. Emelianov, "Environment-dependent generation of photoacoustic waves from plasmonic nanoparticles," Small **8**, 47-52 (2012).

28. S. K. Sahoo and V. Labhasetwar, "Nanotech approaches to drug delivery and imaging," Drug discovery today **8**, 1112-1120 (2003).

29. S. E. A. Gratton, P. D. Pohlhaus, J. Lee, J. Guo, M. J. Cho, and J. M. DeSimone, "Nanofabricated particles for engineered drug therapies: A preliminary biodistribution study of PRINT™ nanoparticles," Journal of Controlled Release **121**, 10-18 (2007).

30. A. E. Hawley, S. S. Davis, and L. Illum, "Targeting of colloids to lymph nodes: influence of lymphatic physiology and colloidal characteristics," Advanced Drug Delivery Reviews **17**, 129-148 (1995).

31. P. Maincent, P. Thouvenot, C. Amicabile, M. Hoffman, J. Kreuter, P. Couvreur, and J. Devissaguet, "Lymphatic Targeting of Polymeric Nanoparticles After Intraperitoneal Administration in Rats," Pharm Res **9**, 1534-1539 (1992).

32. S. Kim, Y.-S. Chen, G. P. Luke, and S. Y. Emelianov, "*In vivo* three-dimensional spectroscopic photoacoustic imaging for monitoring nanoparticle delivery," Biomed. Opt. Express **2**, 2540-2550 (2011).

33. W. H. De Jong and P. J. Borm, "Drug delivery and nanoparticles:applications and hazards," International journal of nanomedicine **3**, 133-149 (2008).

Chapter 5: Conclusions and Future Work

5.1 Summary of the Research

The objective of this study was to create molecular probes for enhanced photoacoustic signal to diagnose the early stage of tumor and improve the therapeutic procedure using nanoclusters. In Chapter 2, photothermal stimuli-responsive PNIPAM nanoclusters were designed and characterized. PNIPAM-AuNS and PNIPAM-CuS were synthesized and photoacoustic signals from these nanoclusters were obtained as a function of temperature. By controlling the interparticle distance between primary nanoparticles, the photoacoustic signal enhancement from clustering of nanoparticles was demonstrated. In Chapter 3, PNIPAM-CuS nanoclusters were used to provide the dynamic contrast in real time *ex vivo*. The stimuli-responsive volumetric changes of the nanoclusters triggered by external light source produce an abrupt photoacoustic signal increase which can be monitored in real time. Chapter 2 and 3 demonstrated that the nanoclusters can be a promising photoacoustic contrast agents. However, using these nanoparticles *in vivo* may cause accumulation of particles and long term toxicity in a body. In Chapter 4, therefore, plasmonic biodegradable nanoclusters consisting of sub-5 nm primary gold particles stabilized by a weakly adsorbed biodegradable polymer were introduced. The photoacoustic signal from biodegradable nanoclusters was quantitatively demonstrated using a tissue mimicking phantom. Since photoacoustic contrast agents are exposed to high laser fluence, their photothermal stability should be stable. Otherwise, the contrast agents do not provide reliable photoacoustic signal. Therefore, the photothermal sensitivity of different sizes of nanoclusters was explored to investigate optimal the size of nanoclusters. These biodegradable nanoclusters were also utilized to determine biodistribution of

nanoparticles. Finally, *in vivo* photoacoustic imaging was performed on tumor-bearing mice using antibody conjugated biodegradable nanoclusters.

5.2 FUTURE DIRECTIONS

Although the suggested photothermal stimuli-responsive nanoclusters provide excellent dynamic contrast for photoacoustic imaging, there is much room to improve in terms of optimizing size of nanocluster and LCST of nanogels. The size of nanocluster introduced in this study is 700 nm in diameter when temperature is below the LCST. Nanoparticles larger than 200 nm in diameter accumulate in the liver and spleen, where the particles are processed by mononuclear phagocyte system (MPS) cells. In addition, larger nanoparticles do not extravasate far from blood vessel because they are trapped in extracellular matrix between cells. In contrast, nanoparticles smaller than 50 nm penetrate deep into tumor tissue [1, 2]. The nanoclusters with 700 nm in diameter still can be used for some applications such as lymph node application and drug delivery system, however, its applications can be extended further if the size of nanocluster can be reduced. Another limitation to the current PNIPAM nanocluster is that LCST temperature is currently 32°C. In order to observe dynamic contrast with these nanoclusters *in vivo*, the LCST have to increase to match biological temperature. The studies on reducing nanogel size and changing LCST have been discussed by co-polymerizing hydrophilic monomers into the polymer matrix [3, 4]. Preliminary results in Figure 5.1 show different sizes of PNIPAM-AuNS nanoclusters. In addition, PNIPAM nanogels might be toxic when they are administered [5] , however, other studies show different results depending on the time scale and cell lines [6, 7]. Therefore, a toxicity study of these PNIPAM nanoclusters needs to be performed.

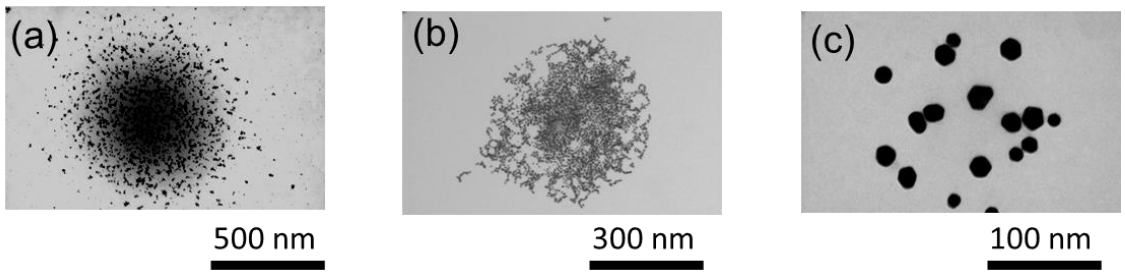

Figure 5.1: Different sizes of PNIPAM-AuNS nanoclusters. The sizes of nanocluster are 700, 350, and 150 nm, respectively.

Spectroscopic photoacoustic imaging is a powerful technique to visualize the location of nanoparticles, however, this method takes time to collect images at several wavelengths and process the data. The biodegradable nanocluster has broad NIR absorbance which is extended to 1064 nm. Therefore, it can be also used for 1064 nm contrast agent in photoacoustic imaging. As described previous chapter, there are several advantages of using the wavelength of 1064 nm in photoacoustic imaging, if nanoclusters can be imaged at 1064 nm. In Figure 5.2b-c, the preliminary results show the combined ultrasound/photoacoustic images of 20, 30, and 40 nm nanoclusters injected porcine tissue. In Figure 5b, imaged at 700 nm, the location of the injected nanoparticles cannot be differentiated from the background noise. In contrast, the presence of nanoparticles is clearly visualized in Figure5.2c which is collected at 1064 nm. In addition, the amplitude of the photoacoustic signal at 1064 nm will decrease when the nanoclusters are injected into a body over time because of the reduction in absorption spectrum of degraded nanoclusters. Thus, the degradation stages of the biodegradable nanoclusters can be monitored by collecting photoacoustic images at 1064 nm.

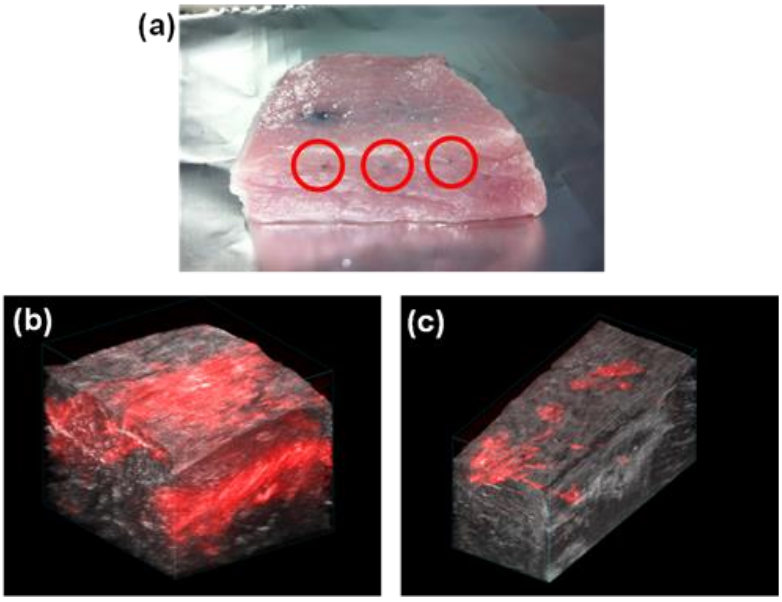

Figure 5.2: (a) Photograph of the 20, 30, and 40 nm nanoclusters injected porcine tissue (b) combined UA/PA images of the porcine tissue with inclusion containing 20, 30, and 40 nm nanoclusters at 700 nm and (c) 1060 nm

5.3 REFERENCES

1. C. H. J. Choi, C. A. Alabi, P. Webster, and M. E. Davis, "Mechanism of active targeting in solid tumors with transferrin-containing gold nanoparticles," Proceedings of the National Academy of Sciences **107**, 1235-1240 (2010).

2. H. Lee, H. Fonge, B. Hoang, R. M. Reilly, and C. Allen, "The Effects of Particle Size and Molecular Targeting on the Intratumoral and Subcellular Distribution of Polymeric Nanoparticles," Molecular Pharmaceutics **7**, 1195-1208 (2010).

3. M. Das, N. Sanson, D. Fava, and E. Kumacheva, "Microgels Loaded with Gold Nanorods: Photothermally Triggered Volume Transitions under Physiological Conditions†," Langmuir **23**, 196-201 (2006).

4. J. Gao and B. J. Frisken, "Influence of Reaction Conditions on the Synthesis of Self-Cross-Linked N-Isopropylacrylamide Microgels," Langmuir **19**, 5217-5222 (2003).

5. P. C. Naha, M. Davoren, F. M. Lyng, and H. J. Byrne, "Reactive oxygen species (ROS) induced cytokine production and cytotoxicity of PAMAM dendrimers in J774A.1 cells," Toxicology and Applied Pharmacology **246**, 91-99 (2010).

6. P. C. Naha, K. Bhattacharya, T. Tenuta, K. A. Dawson, I. Lynch, A. Gracia, F. M. Lyng, and H. J. Byrne, "Intracellular localisation, geno- and cytotoxic response of polyN-isopropylacrylamide (PNIPAM) nanoparticles to human keratinocyte (HaCaT) and colon cells (SW 480)," Toxicology Letters **198**, 134-143 (2010).

7. Y.-H. Lien, T.-M. Wu, J.-H. Wu, and J.-W. Liao, "Cytotoxicity and drug release behavior of PNIPAM grafted on silica-coated iron oxide nanoparticles," J Nanopart Res **13**, 5065-5075 (2011).

Bibliography

J. Aaron, N. Nitin, K. Travis, S. Kumar, T. Collier, S. Y. Park, M. Jose-Yacaman, L. Coghlan, M. Follen, R. Richards-Kortum, and K. Sokolov, "Plasmon resonance coupling of metal nanoparticles for molecular imaging of carcinogenesis *in vivo*," Journal of Biomedical Optics **12**(2007).

J. Aaron, K. Travis, N. Harrison, and K. Sokolov, "Dynamic imaging of molecular assemblies in live cells based on nanoparticle plasmon resonance coupling," Nano Letters **9**, 3612-3618 (2009).

A. Agarwal, S. Huang, M. ODonnell, K. Day, M. Day, N. Kotov, and S. Ashkenazi, "Targeted gold nanorod contrast agent for prostate cancer detection by photoacoustic imaging," Journal of applied physics **102**, 064701-064701-064704 (2007).

A. Agarwal, S. W. Huang, M. O'Donnell, K. C. Day, M. Day, N. Kotov, and S. Ashkenazi, "Targeted gold nanorod contrast agent for prostate cancer detection by photoacoustic imaging," Journal of Applied Physics **102**, 064701-064701-064704 (2007).

W. J. Akers, C. Kim, M. Berezin, K. Guo, R. Fuhrhop, G. M. Lanza, G. M. Fischer, E. Daltrozzo, A. Zumbusch, and X. Cai, "Noninvasive photoacoustic and fluorescence sentinel lymph node identification using dye-loaded perfluorocarbon nanoparticles," ACS nano **5**, 173 (2011).

P. Alivisatos, "The use of nanocrystals in biological detection," Nature Biotechnology **22**, 47-52 (2004).

L. I. o. America, *American National Standard for the Safe Use of Lasers ANSI Z136.1-2000* (American National Standards Institute, Inc., New York, 2000).

G. Baffou and R. Quidant, "Thermo-plasmonics: using metallic nanostructures as nano-sources of heat," Laser & Photonics Reviews **7**, 171-187 (2013).

C. L. Bayer, Y. S. Chen, S. Kim, S. Mallidi, K. Sokolov, and S. Emelianov, "Multiplex photoacoustic molecular imaging using targeted silica-coated gold nanorods," Biomedical optics express **2**, 1828-1835 (2011).

C. L. Bayer, S. Y. Nam, Y.-S. Chen, and S. Y. Emelianov, "Photoacoustic signal amplification through plasmonic nanoparticle aggregation," J Biomed Opt, submitted (2012).

C. L. Bayer, S. Y. Nam, Y.-S. Chen, and S. Y. Emelianov, "Photoacoustic signal amplification through plasmonic nanoparticle aggregation," BIOMEDO **18**, 016001-016001 (2013).

P. Beard, "Biomedical photoacoustic imaging," Interface Focus **1**, 602-631 (2011).

A. G. Bell, "Production of sound by radiant energy," Journal of the Franklin Institute **111**, 401-428 (1881).

S. Bhattacharyya, S. Wang, D. Reinecke, W. Kiser Jr, R. A. Kruger, and T. R. DeGrado, "Synthesis and Evaluation of Near-Infrared (NIR) Dye− Herceptin Conjugates as Photoacoustic Computed Tomography (PCT) Probes for HER2 Expression in Breast Cancer," Bioconjugate chemistry **19**, 1186-1193 (2008).

M. Bikram, A. M. Gobin, R. E. Whitmire, and J. L. West, "Temperature-sensitive hydrogels with SiO2-Au nanoshells for controlled drug delivery," Journal of Controlled Release **123**, 219-227 (2007).

L. S. Bouchard, M. S. Anwar, G. L. Liu, B. Hann, Z. H. Xie, J. W. Gray, X. Wang, A. Pines, and F. F. Chen, "Picomolar sensitivity MRI and photoacoustic imaging of cobalt nanoparticles," Proceedings of the National Academy of Sciences **106**, 4085 (2009).

T. Bowen, "Radiation-Induced Thermoacoustic Soft Tissue Imaging," in *1981 Ultrasonics Symposium*, 1981), 817-822.

C. Bremer, V. Ntziachristos, and R. Weissleder, "Optical-based molecular imaging: contrast agents and potential medical applications," European radiology **13**, 231-243 (2003).

E. Cabane, X. Zhang, K. Langowska, C. Palivan, and W. Meier, "Stimuli-responsive polymers and their applications in nanomedicine," Biointerphases **7**, 1-27 (2012).

L.-C. Chen, C.-W. Wei, J. S. Souris, S.-H. Cheng, C.-T. Chen, C.-S. Yang, P.-C. Li, and L.-W. Lo, "Enhanced photoacoustic stability of gold nanorods by silica matrix confinement," Journal of Biomedical Optics **15**, 016010 (2010).

Y.-S. Chen, W. Frey, S. Aglyamov, and S. Emelianov, "Environment-dependent generation of photoacoustic waves from plasmonic nanoparticles," Small **8**, 47-52 (2012).

Y.-S. Chen, W. Frey, S. Kim, K. Homan, P. Kruizinga, K. Sokolov, and S. Emelianov, "Enhanced thermal stability of silica-coated gold nanorods for photoacoustic imaging and image-guided therapy," Opt. Express **18**, 8867-8878 (2010).

Y. S. Chen, W. Frey, S. Kim, P. Kruizinga, K. Homan, and S. Emelianov, "Silica-coated gold nanorods as photoacoustic signal nanoamplifiers," Nano letters (2011).

Y. S. Chen, W. Frey, S. Kim, P. Kruizinga, K. Homan, and S. Emelianov, "Silica-coated gold nanorods as photoacoustic signal nanoamplifiers," Nano Lett **11**, 348-354 (2011).

C. H. J. Choi, C. A. Alabi, P. Webster, and M. E. Davis, "Mechanism of active targeting in solid tumors with transferrin-containing gold nanoparticles," Proceedings of the National Academy of Sciences **107**, 1235-1240 (2010).

H. S. Choi, W. Liu, P. Misra, E. Tanaka, J. P. Zimmer, B. I. Ipe, M. G. Bawendi, and J. V. Frangioni, "Renal clearance of quantum dots," Nature Biotechnology **25**, 1165-1170 (2007).

J. A. Copland, M. Eghtedari, V. L. Popov, N. Kotov, N. Mamedova, M. Motamedi, and A. A. Oraevsky, "Bioconjugated gold nanoparticles as a molecular based contrast

agent: implications for imaging of deep tumors using optoacoustic tomography," Molecular Imaging & Biology **6**, 341-349 (2004).

M. Das, N. Sanson, D. Fava, and E. Kumacheva, "Microgels Loaded with Gold Nanorods: Photothermally Triggered Volume Transitions under Physiological Conditions†," Langmuir **23**, 196-201 (2006).

W. H. De Jong and P. J. Borm, "Drug delivery and nanoparticles:applications and hazards," International journal of nanomedicine **3**, 133-149 (2008).

A. De La Zerda, C. Zavaleta, S. Keren, S. Vaithilingam, S. Bodapati, Z. Liu, J. Levi, B. R. Smith, T. J. Ma, and O. Oralkan, "Carbon nanotubes as photoacoustic molecular imaging agents in living mice," Nature nanotechnology **3**, 557-562 (2008).

G. J. Diebold, M. I. Khan, and S. M. Park, "Photoacoustic "signatures" of particulate matter: optical poduction of acoustic monopole radiation," Science **250**, 101-104 (1990).

T. L. Doane and C. Burda, "The unique role of nanoparticles in nanomedicine: imaging, drug delivery and therapy," Chemical Society Reviews **41**, 2885-2911 (2012).

K. Doi, "Current status and future potential of computer-aided diagnosis in medical imaging," British Journal of Radiology **78**, s3-s19 (2005).

D. Duracher, A. Elaissari, and C. Pichot, "Characterization of cross-linked poly(N-isopropylmethacrylamide) microgel latexes," Colloid Polym. Sci. **277**, 905-913 (1999).

I. H. El-Sayed, X. Huang, and M. A. El-Sayed, "Surface plasmon resonance scattering and absorption of anti-EGFR antibody conjugated gold nanoparticles in cancer diagnostics: applications in oral cancer," Nano letters **5**, 829-834 (2005).

D. R. Elias, D. L. J. Thorek, A. K. Chen, J. Czupryna, and A. Tsourkas, "*In vivo* imaging of cancer biomarkers using activatable molecular probes," Cancer Biomarkers **4**, 287-305 (2008).

S. Emelianov, S. Aglyamov, A. Karpiouk, S. Mallidi, S. Park, S. Sethuraman, J. Shah, R. Smalling, J. Rubin, and W. Scott, "Synergy and Applications of Combined Ultrasound, Elasticity, and Photoacoustic Imaging," in *IEEE International Ultrasonics Symposium*, (IEEE, 2006), 405-415.

S. Y. Emelianov, S. R. Aglyamov, A. B. Karpiouk, S. Mallidi, S. Park, S. Sethuraman, J. Shah, R. W. Smalling, J. M. Rubin, and W. G. Scott, "1E-5 Synergy and Applications of Combined Ultrasound, Elasticity, and Photoacoustic Imaging (Invited)," in *Ultrasonics Symposium, 2006. IEEE*, 2006), 405-415.

S. Y. Emelianov, P. C. Li, and M. O'Donnell, "Photoacoustics for molecular imaging and therapy," Physics today **62**, 34 (2009).

R. O. Esenaliev, A. A. Karabutov, and A. A. Oraevsky, "Sensitivity of laser opto-acoustic imaging in detection of small deeply embedded tumors," Selected Topics in Quantum Electronics, IEEE Journal of **5**, 981-988 (1999).

W. Evans, R. Prasher, J. Fish, P. Meakin, P. Phelan, and P. Keblinski, "Effect of aggregation and interfacial thermal resistance on thermal conductivity of nanocomposites and colloidal nanofluids," International Journal of Heat and Mass Transfer **51**, 1431-1438 (2008).

E. I. Galanzha, J. W. Kim, and V. P. Zharov, "Nanotechnology-based molecular photoacoustic and photothermal flow cytometry platform for *in-vivo* detection and killing of circulating cancer stem cells," Journal of biophotonics **2**, 725-735 (2009).

E. I. Galanzha, E. V. Shashkov, T. Kelly, J. W. Kim, L. Yang, and V. P. Zharov, "*In vivo* magnetic enrichment and multiplex photoacoustic detection of circulating tumour cells," Nature nanotechnology **4**, 855-860 (2009).

E. I. Galanzha and V. P. Zharov, "Photoacoustic flow cytometry," Methods **57**, 280-296 (2012).

S. S. Gambhir, "Molecular imaging of cancer with positron emission tomography," Nature Reviews Cancer **2**, 683-693 (2002).

J. Gao and B. J. Frisken, "Influence of Reaction Conditions on the Synthesis of Self-Cross-Linked N-Isopropylacrylamide Microgels," Langmuir **19**, 5217-5222 (2003).

Z. Ge, Y. Kang, T. A. Taton, P. V. Braun, and D. G. Cahill, "Thermal transport in Au-core polymer-shell nanoparticles," Nano Letters **5**, 531-535 (2005).

S. E. A. Gratton, P. D. Pohlhaus, J. Lee, J. Guo, M. J. Cho, and J. M. DeSimone, "Nanofabricated particles for engineered drug therapies: A preliminary biodistribution study of PRINT™ nanoparticles," Journal of Controlled Release **121**, 10-18 (2007).

R. C. Gray and A. J. Bard, "Photoacoustic spectroscopy applied to systems involving photoinduced gas evolution or consumption," Analytical Chemistry **50**, 1262-1265 (1978).

T. Harrison, J. C. Ranasinghesagara, H. Lu, K. Mathewson, A. Walsh, and R. J. Zemp, "Combined photoacoustic and ultrasound biomicroscopy," Optics Express **17**, 22041-22046 (2009).

A. E. Hawley, S. S. Davis, and L. Illum, "Targeting of colloids to lymph nodes: influence of lymphatic physiology and colloidal characteristics," Advanced Drug Delivery Reviews **17**, 129-148 (1995).

S. Hirotsu, Y. Hirokawa, and T. Tanaka, "Volume-phase transitions of ionized N-isopropylacrylamide gels," The Journal of Chemical Physics **87**, 1392-1395 (1987).

K. Homan, S. Kim, Y.-S. Chen, B. Wang, S. Mallidi, and S. Emelianov, "Prospects of molecular photoacoustic imaging at 1064 nm wavelength," Opt. Lett. **35**, 2663-2665 (2010).

K. Homan, S. Kim, Y. S. Chen, B. Wang, S. Mallidi, and S. Emelianov, "Prospects of molecular photoacoustic imaging at 1064 nm wavelength," Optics letters **35**, 2663-2665 (2010).

K. Homan, S. Mallidi, E. Cooley, and S. Emelianov, "Combined photoacoustic and ultrasound imaging of metal nanoparticles *in vivo*," in *Nanoimaging* (Pan Stanford Publishing, Singapore, 2010).

K. A. Homan, M. Souza, R. Truby, G. P. Luke, C. Green, E. Vreeland, and S. Emelianov, "Silver Nanoplate Contrast Agents for *In Vivo* Molecular Photoacoustic Imaging," ACS nano, 641-650 (2012).

G. Huang, J. Gao, Z. Hu, J. V. St. John, B. C. Ponder, and D. Moro, "Controlled drug release from hydrogel nanoparticle networks," Journal of Controlled Release **94**, 303-311 (2004).

X. Huang, P. K. Jain, I. H. El-Sayed, and M. A. El-Sayed, "Plasmonic photothermal therapy (PPTT) using gold nanoparticles," Lasers in Medical Science **23**, 217-228 (2008).

P. K. Jain, I. H. El-Sayed, and M. A. El-Sayed, "Au nanoparticles target cancer," Nano Today **2**, 18-29 (2007).

P. K. Jain, K. S. Lee, I. H. El-Sayed, and M. A. El-Sayed, "Calculated absorption and scattering properties of gold nanoparticles of different size, shape, and composition: Applications in biological imaging and biomedicine," Journal of Physical Chemistry B **110**, 7238-7248 (2006).

N. R. Jana, L. Gearheart, and C. J. Murphy, "Seed-mediated growth approach for shape-controlled synthesis of spheroidal and rod-like gold nanoparticles using a surfactant template," Advanced Materials **13**, 1389-1393 (2001).

Y. Jin, C. Jia, S. W. Huang, M. O'Donnell, and X. Gao, "Multifunctional nanoparticles as coupled contrast agents," Nature Communications **1**, 41 (2010).

J. V. Jokerst, A. J. Cole, D. Van de Sompel, and S. S. Gambhir, "Gold nanorods for ovarian cancer detection with photoacoustic imaging and resection guidance via raman imaging in living mice," ACS Nano **6**, 10366-10377 (2012).

B. Kang, D. Yu, Y. Dai, S. Chang, D. Chen, and Y. Ding, "Cancer-Cell Targeting and Photoacoustic Therapy Using Carbon Nanotubes as “Bomb” Agents," Small **5**, 1292-1301 (2009).

B. T. Khuri-Yakub, X. Chen, H. Dai, and S. S. Gambhir, "Family of Enhanced Photoacoustic Imaging Agents for High-Sensitivity and Multiplexing Studies in Living Mice," ACS Nano **6**, 4694-4701 (2012).

C. Kim, E. C. Cho, J. Chen, K. H. Song, L. Au, C. Favazza, Q. Zhang, C. M. Cobley, F. Gao, and Y. Xia, "*In vivo* molecular photoacoustic tomography of melanomas targeted by bioconjugated gold nanocages," ACS nano (2010).

C. Kim, H. M. Song, X. Cai, J. Yao, A. Wei, and L. V. Wang, "*In vivo* photoacoustic mapping of lymphatic systems with plasmon-resonant nanostars," Journal of materials chemistry **21**, 2841-2844 (2011).

G. Kim, S. W. Huang, K. C. Day, M. O’Donnell, R. R. Agayan, M. A. Day, R. Kopelman, and S. Ashkenazi, "Indocyanine-green-embedded PEBBLEs as a contrast agent for photoacoustic imaging," Journal of biomedical optics **12**, 044020 (2007).

J. W. Kim, E. I. Galanzha, E. V. Shashkov, H. M. Moon, and V. P. Zharov, "Golden carbon nanotubes as multimodal photoacoustic and photothermal high-contrast molecular agents," Nature nanotechnology **4**, 688-694 (2009).

K. Kim, S. W. Huang, S. Ashkenazi, M. O’Donnell, A. Agarwal, N. A. Kotov, M. F. Denny, and M. J. Kaplan, "Photoacoustic imaging of early inflammatory response using gold nanorods," Applied physics letters **90**, 223901 (2007).

S. Kim, Y.-S. Chen, G. P. Luke, and S. Y. Emelianov, "*In vivo* three-dimensional spectroscopic photoacoustic imaging for monitoring nanoparticle delivery," Biomed. Opt. Express **2**, 2540-2550 (2011).

S. Kim, Y. S. Chen, G. P. Luke, and S. Y. Emelianov, "*In vivo* three-dimensional spectroscopic photoacoustic imaging for monitoring nanoparticle delivery," Biomedical optics express **2**, 2540-2550 (2011).

H. Kobayashi and P. L. Choyke, "Target-cancer-cell-specific activatable fluorescence imaging probes: rational design and *in vivo* applications," Accounts of Chemical Research **44**, 83-90 (2011).

K. Kostarelos, A. Bianco, and M. Prato, "Promises, facts and challenges for carbon nanotubes in imaging and therapeutics," Nature nanotechnology **4**, 627-633 (2009).

R. A. Kruger and P. Y. Liu, "Photoacoustic ultrasound: Pulse production and detection in 0.5% Liposyn," Medical physics **21**, 1179-1184 (1994).

G. Ku and L. V. Wang, "Deeply penetrating photoacoustic tomography in biological tissues enhancedwith an optical contrast agent," Opt. Lett. **30**, 507-509 (2005).

G. Ku, X. Wang, X. Xie, G. Stoica, and L. V. Wang, "Imaging of tumor angiogenesis in rat brains *in vivo* by photoacoustic tomography," Applied optics **44**, 770-775 (2005).

G. Ku, M. Zhou, S. Song, Q. Huang, J. Hazle, and C. Li, "Copper Sulfide Nanoparticles As a New Class of Photoacoustic Contrast Agent for Deep Tissue Imaging at 1064 nm," ACS Nano **6**, 7489-7496 (2012).

Y. Lao, D. Xing, S. Yang, and L. Xiang, "Noninvasive photoacoustic imaging of the developing vasculature during early tumor growth," Phys Med Biol **53**, 4203-4212 (2008).

J. Laufer, P. Johnson, E. Zhang, B. Treeby, B. Cox, B. Pedley, and P. Beard, "*In vivo* preclinical photoacoustic imaging of tumor vasculature development and therapy," Journal of Biomedical Optics **17**, 056016-056011 (2012).

H. Lee, H. Fonge, B. Hoang, R. M. Reilly, and C. Allen, "The Effects of Particle Size and Molecular Targeting on the Intratumoral and Subcellular Distribution of Polymeric Nanoparticles," Molecular Pharmaceutics **7**, 1195-1208 (2010).

J. Levi, S. R. Kothapalli, T.-J. Ma, K. Hartman, B. T. Khuri-Yakub, and S. S. Gambhir, "Design, synthesis, and imaging of an activatable photoacoustic probe," Journal of the American Chemical Society **132**, 11264-11269 (2010).

N. Lewinski, V. Colvin, and R. Drezek, "Cytotoxicity of nanoparticles," Small **4**, 26-49 (2008).

M.-L. Li, J.-T. Oh, X. Xie, G. Ku, W. Wang, C. Li, G. Lungu, G. Stoica, and L. V. Wang, "Simultaneous molecular and hypoxia imaging of brain tumors *in vivo* using spectroscopic photoacoustic tomography," Proceedings of the Ieee **96**, 481-489 (2008).

M. L. Li, J. T. Oh, X. Xie, G. Ku, W. Wang, C. Li, G. Lungu, G. Stoica, and L. V. Wang, "Simultaneous molecular and hypoxia imaging of brain tumors *in vivo* using spectroscopic photoacoustic tomography," Proceedings of the IEEE **96**, 481-489 (2008).

M. L. Li, J. C. Wang, J. A. Schwartz, K. L. Gill-Sharp, G. Stoica, and L. V. Wang, "*In-vivo* photoacoustic microscopy of nanoshell extravasation from solid tumor vasculature," Journal of biomedical optics **14**, 010507 (2009).

P.-C. Li, C.-R. C. Wang, D.-B. Shieh, C.-W. Wei, C.-K. Liao, C. Poe, S. Jhan, A.-A. Ding, and Y.-N. Wu, "*In vivo* photoacoustic molecular imaging withsimultaneous multiple selective targeting usingantibody-conjugated gold nanorods," Opt. Express **16**, 18605-18615 (2008).

P. C. Li, C. W. Wei, C. K. Liao, C. D. Chen, K. C. Pao, C. R. C. Wang, Y. N. Wu, and D. B. Shieh, "Photoacoustic imaging of multiple targets using gold nanorods," Ultrasonics, Ferroelectrics and Frequency Control, IEEE Transactions on **54**, 1642-1647 (2007).

Y.-H. Lien, T.-M. Wu, J.-H. Wu, and J.-W. Liao, "Cytotoxicity and drug release behavior of PNIPAM grafted on silica-coated iron oxide nanoparticles," J Nanopart Res **13**, 5065-5075 (2011).

W. Lu, Q. Huang, G. Ku, X. Wen, M. Zhou, D. Guzatov, P. Brecht, R. Su, A. Oraevsky, and L. V. Wang, "Photoacoustic imaging of living mouse brain vasculature using hollow gold nanospheres," Biomaterials **31**, 2617-2626 (2010).

G. P. Luke, D. Yeager, and S. Y. Emelianov, "Biomedical Applications of Photoacoustic Imaging with Exogenous Contrast Agents," Annals of biomedical engineering, 1-16 (2012).

L. L. Ma, M. D. Feldman, J. M. Tam, A. S. Paranjape, K. K. Cheruku, T. A. Larson, J. O. Tam, D. R. Ingram, V. Paramita, and J. W. Villard, "Small multifunctional nanoclusters (nanoroses) for targeted cellular imaging and therapy," ACS nano **3**, 2686-2696 (2009).

R. Ma, A. Taruttis, V. Ntziachristos, and D. Razansky, "Multispectral optoacoustic tomography (MSOT) scanner for whole-body small animal imaging," Optics Express **17**, 21414-21426 (2009).

P. Maincent, P. Thouvenot, C. Amicabile, M. Hoffman, J. Kreuter, P. Couvreur, and J. Devissaguet, "Lymphatic Targeting of Polymeric Nanoparticles After Intraperitoneal Administration in Rats," Pharm Res **9**, 1534-1539 (1992).

S. Mallidi, T. Larson, J. Aaron, K. Sokolov, and S. Emelianov, "Molecular specific optoacoustic imaging with plasmonic nanoparticles," Optics Express **15**, 6583-6588 (2007).

S. Mallidi, T. Larson, J. Aaron, K. Sokolov, and S. Emelianov, "Molecular specific optoacoustic imaging with plasmonic nanoparticles," Opt. Express **15**, 6583-6588 (2007).

S. Mallidi, T. Larson, J. Tam, P. P. Joshi, A. Karpiouk, K. Sokolov, and S. Emelianov, "Multiwavelength Photoacoustic Imaging and Plasmon Resonance Coupling of Gold Nanoparticles for Selective Detection of Cancer," Nano Letters **9**, 2825-2831 (2009).

S. Mallidi, G. P. Luke, and S. Emelianov, "Photoacoustic imaging in cancer detection, diagnosis, and treatment guidance," Trends in biotechnology (2011).

S. Manohar, C. Ungureanu, and T. G. Van Leeuwen, "Gold nanorods as molecular contrast agents in photoacoustic imaging: the promises and the caveats," Contrast Media & Molecular Imaging **6**, 389-400 (2011).

K. Maslov, H. F. Zhang, S. Hu, and L. V. Wang, "Optical-resolution photoacoustic microscopy for *in vivo* imaging of single capillaries," Opt Lett **33**, 929-931 (2008).

K. Maslov, H. F. Zhang, S. Hu, and L. V. Wang, "Optical-resolution photoacoustic microscopy for *in vivo* imaging of single capillaries," Opt. Lett. **33**, 929-931 (2008).

M. Mehrmohammadi, S. J. Yoon, D. Yeager, and S. Y. Emelianov, "Photoacoustic Imaging for Cancer Detection and Staging," Current molecular imaging **2**, 89-105 (2013).

S. R. Meikle, P. Kench, M. Kassiou, and R. B. Banati, "Small animal SPECT and its place in the matrix of molecular imaging technologies," Physics in medicine and biology **50**, R45 (2005).

S. Mura, J. Nicolas, and P. Couvreur, "Stimuli-responsive nanocarriers for drug delivery," Nature Materials **12**, 991- 1003 (2013).

P. C. Naha, K. Bhattacharya, T. Tenuta, K. A. Dawson, I. Lynch, A. Gracia, F. M. Lyng, and H. J. Byrne, "Intracellular localisation, geno- and cytotoxic response of polyN-isopropylacrylamide (PNIPAM) nanoparticles to human keratinocyte (HaCaT) and colon cells (SW 480)," Toxicology Letters **198**, 134-143 (2010).

P. C. Naha, M. Davoren, F. M. Lyng, and H. J. Byrne, "Reactive oxygen species (ROS) induced cytokine production and cytotoxicity of PAMAM dendrimers in J774A.1 cells," Toxicology and Applied Pharmacology **246**, 91-99 (2010).

S. Y. Nam, L. M. Ricles, L. J. Suggs, and S. Y. Emelianov, "Nonlinear photoacoustic signal increase from endocytosis of gold nanoparticles," Optics Letters **37**, 4708-4710 (2012).

J. J. Niederhauser, M. Jaeger, R. Lemor, P. Weber, and M. Frenz, "Combined ultrasound and optoacoustic system for real-time high-contrast vascular imaging *in vivo*," Medical Imaging, IEEE Transactions on **24**, 436-440 (2005).

B. Nikoobakht and M. A. El-Sayed, "Preparation and growth mechanism of gold nanorods (NRs) using seed-mediated growth method," Chemistry of Materials **15**, 1957-1962 (2003).

V. Ntziachristos, C.-H. Tung, C. Bremer, and R. Weissleder, "Fluorescence molecular tomography resolves protease activity *in vivo*," Nature Medicine **8**, 757-760 (2002).

J.-T. Oh, M.-L. Li, H. F. Zhang, K. Maslov, G. Stoica, and L. V. Wang, "Three-dimensional imaging of skin melanoma *in vivo* by dual-wavelength photoacoustic microscopy," Journal of biomedical optics **11**, 034032-034032 (2006).

A. A. Oraevsky, S. L. Jacques, R. O. Esenaliev, and F. K. Tittel, *Laser-based optoacoustic imaging in biological tissues*, Laser-Tissue Interaction V, Proceedings Of (1994), Vol. 2134, pp. 122-128.

A. A. Oraevsky, S. L. Jacques, R. O. Esenaliev, and F. K. Tittel, *Time-Resolved Optoacoustic Imaging in Layered Biological Tissues*, Advances in Optical Imaging and Photon Migration (Academic Press, New York, 1994), Vol. 21, pp. 161-165.

A. A. Oraevsky and A. A. Karabutov, *Optoacoustic tomography. In Biomedical Photonics Handbook* (CRC Press, Boca Raton, Florida, 2003), pp. 34/31–34/34.

D. Pan, M. Pramanik, A. Senpan, X. Yang, K. H. Song, M. J. Scott, H. Zhang, P. J. Gaffney, S. A. Wickline, and L. V. Wang, "Molecular photoacoustic tomography with colloidal nanobeacons," Angewandte Chemie **121**, 4234-4237 (2009).

S. Park, S. Mallidi, A. B. Karpiouk, S. Aglyamov, and S. Y. Emelianov, "Photoacoustic imaging using array transducer," in *SPIE Photonics West*, 2007), 643714.

J. M. Perez, L. Josephson, and R. Weissleder, "Use of magnetic nanoparticles as nanosensors to probe for molecular interactions," ChemBioChem **5**, 261-264 (2004).

M. Pramanik, M. Swierczewska, D. Green, B. Sitharaman, and L. V. Wang, "Single-walled carbon nanotubes as a multimodal-thermoacoustic and photoacoustic-contrast agent," Journal of biomedical optics **14**, 034018 (2009).

D. Razansky, C. Vinegoni, and V. Ntziachristos, "Multispectral photoacoustic imaging of fluorochromes in small animals," Optics letters **32**, 2891-2893 (2007).

A. Rosencwaig and A. Gersho, "Theory of the photoacoustic effect with solids," Journal of applied physics **47**, 64-69 (1976).

S. K. Sahoo and V. Labhasetwar, "Nanotech approaches to drug delivery and imaging," Drug discovery today **8**, 1112-1120 (2003).

A. Sanchot, G. Baffou, R. Marty, A. Arbouet, R. Quidant, C. Girard, and E. Dujardin, "Plasmonic nanoparticle networks for light and heat concentration," ACS Nano **6**, 3434-3440 (2012).

H. G. Schild, "Poly (n-isopropylacrylamide) - experiment, theory and application," Progress in Polymer Science **17**, 163-249 (1992).

H. G. Schild, "Poly(N-isopropylacrylamide): experiment, theory and application," Progress in Polymer Science **17**, 163-249 (1992).

S. Sethuraman, J. H. Amirian, S. H. Litovsky, R. W. Smalling, and S. Y. Emelianov, "Spectroscopic intravascular photoacoustic imaging to differentiate atherosclerotic plaques," Optics Express **16**, 3362-3367 (2008).

E. V. Shashkov, M. Everts, E. I. Galanzha, and V. P. Zharov, "Quantum dots as multimodal photoacoustic and photothermal contrast agents," Nano letters **8**, 3953-3958 (2008).

R. Siegel, E. Ward, O. Brawley, and A. Jemal, "Cancer statistics, 2011," CA: A Cancer Journal for Clinicians (2011).

R. Siphanto, K. Thumma, R. Kolkman, T. G. Leeuwen, F. F. M. Mul, J. W. Neck, L. N. A. Adrichem, and W. Steenbergen, "Serial nonivasive photoacoustic imaging of neovascularization in tumor angiogenesis," Optics express **13**, 89-95 (2005).

A. M. Smith, M. C. Mancini, and S. Nie, "Second window for *in vivo* imaging," Nature Nanotechnology **4**, 710-711 (2009).

K. Sokolov, M. Follen, J. Aaron, I. Pavlova, A. Malpica, R. Lotan, and R. Richards-Kortum, "Real-time vital optical imaging of precancer using anti-epidermal growth factor receptor antibodies conjugated to gold nanoparticles," Cancer Research **63**, 1999-2004 (2003).

K. H. Song, C. Kim, C. M. Cobley, Y. Xia, and L. V. Wang, "Near-infrared gold nanocages as a new class of tracers for photoacoustic sentinel lymph node mapping on a rat model," Nano letters **9**, 183-188 (2008).

K. H. Song, C. Kim, K. Maslov, and L. V. Wang, "Noninvasive *in vivo* spectroscopic nanorod-contrast photoacoustic mapping of sentinel lymph nodes," European journal of radiology **70**, 227-231 (2009).

K. H. Song, E. W. Stein, J. A. Margenthaler, and L. V. Wang, "Noninvasive photoacoustic identification of sentinel lymph nodes containing methylene blue *in vivo* in a rat model," Journal of biomedical optics **13**, 054033 (2008).

K. M. Stantz, M. Cao, B. Liu, K. D. Miller, and L. Guo, "Molecular imaging of neutropilin-1 receptor using photoacoustic spectroscopy in breast tumors," in *SPIE Photonics West*, 2010), 75641O.

E. Strohm, M. Rui, I. Gorelikov, N. Matsuura, and M. Kolios, "Vaporization of perfluorocarbon droplets using optical irradiation," Biomedical optics express **2**, 1432-1442 (2011).

M. A. C. Stuart, W. T. S. Huck, J. Genzer, M. Mueller, C. Ober, M. Stamm, G. B. Sukhorukov, I. Szleifer, V. V. Tsukruk, M. Urban, F. Winnik, S. Zauscher, I. Luzinov, and S. Minko, "Emerging applications of stimuli-responsive polymer materials," Nature Materials **9**, 101-113 (2010).

M. A. C. Stuart, W. T. S. Huck, J. Genzer, M. Muller, C. Ober, M. Stamm, G. B. Sukhorukov, I. Szleifer, V. V. Tsukruk, M. Urban, F. Winnik, S. Zauscher, I. Luzinov, and S. Minko, "Emerging applications of stimuli-responsive polymer materials," **9**(2010).

A. C. Tam, "Applications of photoacoustic sensing techniques," Reviews of Modern Physics **58**, 381-431 (1986).

J. M. Tam, A. K. Murthy, D. R. Ingram, R. Nguyen, K. V. Sokolov, and K. P. Johnston, "Kinetic assembly of Near-IR-Active gold nanoclusters using weakly adsorbing polymers to control the size," Langmuir **26**, 8988-8999 (2010).

J. M. Tam, J. O. Tam, A. Murthy, D. R. Ingram, L. L. Ma, K. Travis, K. P. Johnston, and K. V. Sokolov, "Controlled assembly of biodegradable plasmonic nanoclusters for near-infrared Imaging and therapeutic applications," ACS nano **4**, 2178-2184 (2010).

C. M. C. Tempany and B. J. McNeil, "Advances in biomedical imaging," JAMA: The Journal of the American Medical Association **285**, 562-567 (2001).

T. Thomas, P. Dale, R. Weight, U. Atasoy, J. Magee, and J. Viator, "Photoacoustic detection of breast cancer cells in human blood," significance **1**, 2 (2008).

B. P. Timko, T. Dvir, and D. S. Kohane, "Remotely triggerable drug delivery systems," Advanced Materials **22**, 4925-4943 (2010).

V. V. Tuchin, A. Tárnok, and V. P. Zharov, "*In vivo* flow cytometry: a horizon of opportunities," Cytometry Part A **79**, 737-745 (2011).

J. K. Vasir and V. Labhasetwar, "Biodegradable nanoparticles for cytosolic delivery of therapeutics," Advanced Drug Delivery Reviews **59**, 718-728 (2007).

T. Vermonden, R. Censi, and W. E. Hennink, "Hydrogels for protein delivery," Chemical Reviews **112**, 2853-2888 (2012).

J. A. Viator, S. Gupta, B. S. Goldschmidt, K. Bhattacharyya, R. Kannan, R. Shukla, P. S. Dale, E. Boote, and K. Katti, "Gold nanoparticle mediated detection of prostate cancer cells using photoacoustic flowmetry with optical reflectance," Journal of Biomedical Nanotechnology **6**, 187-191 (2010).

H. N. Wagner Jr and P. S. Conti, "Advances in medical imaging for cancer diagnosis and treatment," Cancer **67**, 1121-1128 (1991).

B. Wang, E. Yantsen, T. Larson, A. B. Karpiouk, S. Sethuraman, J. L. Su, K. Sokolov, and S. Y. Emelianov, "Plasmonic Intravascular Photoacoustic Imaging for Detection of Macrophages in Atherosclerotic Plaques," Nano Lett. **9**, 2212-2217 (2008).

B. Wang, E. Yantsen, T. Larson, A. B. Karpiouk, S. Sethuraman, J. L. Su, K. Sokolov, and S. Y. Emelianov, "Plasmonic intravascular photoacoustic imaging for detection of macrophages in atherosclerotic plaques," Nano Letters **9**, 2212-2217 (2009).

C. Wang, J. Chen, T. Talavage, and J. Irudayaraj, "Gold Nanorod/Fe3O4 Nanoparticle "Nano-Pearl-Necklaces" for Simultaneous Targeting, Dual-Mode Imaging, and Photothermal Ablation of Cancer Cells," Angewandte Chemie **121**, 2797-2801 (2009).

L. Wang, *Photoacoustic Imaging and Spectroscopy*, Optical Science and Engineering (CRC Press, 2009).

L. V. Wang, "Prospects of photoacoustic tomography," Medical Physics **35**, 5758 (2008).

L. V. Wang, "Multiscale photoacoustic microscopy and computed tomography," Nature photonics **3**, 503-509 (2009).

L. V. Wang and S. Hu, "Photoacoustic tomography: *in vivo* imaging from organelles to organs," Science **335**, 1458-1462 (2012).

X. Wang, Y. Pang, G. Ku, X. Xie, G. Stoica, and L. V. Wang, "Noninvasive laser-induced photoacoustic tomography for structural and functional *in vivo* imaging of the brain," Nat Biotech **21**, 803-806 (2003).

Y. Wang, X. Xie, X. Wang, G. Ku, K. L. Gill, D. P. O'Neal, G. Stoica, and L. V. Wang, "Photoacoustic tomography of a nanoshell contrast agent in the *in vivo* rat brain," Nano letters **4**, 1689-1692 (2004).

Y. T. Wang, S. Teitel, and C. Dellago, "Surface-driven bulk reorganization of gold nanorods," Nano Letters **5**, 2174-2178 (2005).

Y. W. Wang, X. Y. Xie, X. D. Wang, G. Ku, K. L. Gill, D. P. O'Neal, G. Stoica, and L. V. Wang, "Photoacoustic tomography of a nanoshell contrast agent in the *in vivo* rat brain," Nano Letters **4**, 1689-1692 (2004).

R. Weissleder, "Molecular Imaging: Exploring the Next Frontier1," Radiology **212**, 609-614 (1999).

R. Weissleder, "Scaling down imaging: molecular mapping of cancer in mice," Nature Reviews Cancer **2**, 11-18 (2002).

R. Weissleder, "Molecular imaging in cancer," Science's STKE **312**, 1168 (2006).

R. Weissleder and M. J. Pittet, "Imaging in the era of molecular oncology," Nature **452**, 580-589 (2008).

K. Wilson, K. Homan, and S. Emelianov, "Synthesis of a dual contrast agent for ultrasound and photoacoustic imaging," in *SPIE Photonics West*, 2010), 75760M.

K. Wilson, K. Homan, and S. Emelianov, "Biomedical photoacoustics beyond thermal expansion using triggered nanodroplet vaporization for contrast-enhanced imaging," Nature Communications **3**, 618 (2012).

L. Xiang, Y. Yuan, D. Xing, Z. Ou, S. Yang, and F. Zhou, "Photoacoustic molecular imaging with antibody-functionalized single-walled carbon nanotubes for early diagnosis of tumor," Journal of biomedical optics **14**, 021008 (2009).

M. Xu and L. V. Wang, "Analytic explanation of spatial resolution related to bandwidth and detector aperture size in thermoacoustic or photoacoustic reconstruction," Physical Review E **67**, 056605 (2003).

M. Xu and L. V. Wang, "Photoacoustic imaging in biomedicine," Review of scientific instruments **77**, 041101 (2006).

X. Yang, S. E. Skrabalak, Z. Y. Li, Y. Xia, and L. V. Wang, "Photoacoustic tomography of a rat cerebral cortex *in vivo* with Au nanocages as an optical contrast agent," Nano letters **7**, 3798-3802 (2007).

X. Yang, E. W. Stein, S. Ashkenazi, and L. V. Wang, "Nanoparticles for photoacoustic imaging," Wiley Interdisciplinary Reviews: Nanomedicine and Nanobiotechnology **1**, 360-368 (2009).

A. Zerda, J. W. Kim, E. I. Galanzha, S. S. Gambhir, and V. P. Zharov, "Advanced contrast nanoagents for photoacoustic molecular imaging, cytometry, blood test and photothermal theranostics," Contrast Media & Molecular Imaging **6**, 346-369 (2011).

L. Zha, B. Banik, and F. Alexis, "Stimulus responsive nanogels for drug delivery," Soft Matter **7**, 5908-5916 (2011).

H. F. Zhang, K. Maslov, G. Stoica, and L. V. Wang, "Functional photoacoustic microscopy for high-resolution and noninvasive *in vivo* imaging," Nature biotechnology **24**, 848-851 (2006).

V. P. Zharov, "Ultrasharp nonlinear photothermal and photoacoustic resonances and holes beyond the spectral limit," Nature Photonics **5**, 110-226 (2011).

V. P. Zharov, E. I. Galanzha, E. V. Shashkov, N. G. Khlebtsov, and V. V. Tuchin, "*In vivo* photoacoustic flow cytometry for monitoring of circulating single cancer cells and contrast agents," Optics letters **31**, 3623-3625 (2006).

Vita

Soon Joon Yoon received his B.S. and M.S. in Electrical and Computer Engineering from Yonsei University, South Korea, in 2006 and 2008, respectively. He entered The University of Texas at Austin for his Ph.D. study and joined the Ultrasound Imaging and Therapeutics Research Laboratory in 2008. His graduate research has been focused on photoacoustic contrast agents.

Permanent email address: o2no2n@gmail.com

This dissertation was typed by Soon Joon Yoon